CAVITY FORMATION IN THE RABBIT MODEL OF TUBERCULOSIS

by
Brian M Luna

A dissertation submitted to Johns Hopkins University in conformity with the requirements for the degree of Doctor of Philosophy

Baltimore, Maryland
May 2014

© 2014 Brian M Luna
All Rights Reserved

Abstract

Tuberculosis is one of the leading causes of morbidity and mortality among infectious diseases. The development of cavitary lesions is a major concern; it is believed that cavitary lesions contribute to tuberculosis disease transmission and antibiotic resistance. The progression of cavitary lesions can also be a sign of treatment failure. Despite the health significance of cavitary tuberculosis, there is currently no test or assay to assess which patients would be most likely to develop cavitary disease. Tests capable of detecting early treatment failure could be useful in clinical trial settings and save a considerable amount of money for failed drugs, as clinical trials are expensive due to long-term treatment and follow up monitoring required for tuberculosis. In this work, a non-invasive imaging tool is presented that is capable of predicting which rabbits will continue to progress to develop cavitary disease. Next a RNA sequencing study was performed to measure the global transcriptome response of the host at the cavitary lesion. One of the genes identified as being upregulated in the cavitary tissue was *mmp-1*. We hypothesized that MMP-1 was involved in cavitary lesion development and tested our hypothesis by treating *M. tb* infected rabbits with a small molecule, RO32-3555 (Trocade), which inhibits MMP-1 activity.

Thesis Advisor- William R Bishai, MD, PhD

2nd reader- Sanjay K Jain, MD

Thesis Advisors:

William R. Bishai, MD, PhD, Professor of Medicine and Pathology, Johns Hopkins University School of Medicine

Thesis Committee:

Sanjay K. Jain, MD, Associate Professor of Pediatrics and International Health, Johns Hopkins University School of Medicine

Jacques Grosset, MD, Professor, Center for Tuberculosis Research, Johns Hopkins University School of Medicine

Assaf A. Gilad, PhD, Professor of Radiology, Johns Hopkins University School of Medicine

Acknowledgements

There are a number of people that need to be thanked and without their help none of this work would have been possible. Dr. William Bishai has been a great mentor and I couldn't have asked for anything more. He provided me with an environment that allowed me to fail and even though it might sound counterintuitive it was through the failures that I continued to mature. His constant encouragement, especially during tough times, was always appreciated.

During my time as a graduate student Dr. Bishai had accepted a position and relocated to Durban, South Africa. Despite the move there was never a feeling of isolation or abandonment and Dr. Sanjay Jain deserves much credit for that. He would always ask about how the work was progressing and if any help was needed. In similar regards to Dr. Bishai, the most important support from Dr. Jain was his constant encouragement.

I would also like to thank the thesis committee as a whole: Dr. Sanjay Jain, Dr. Jacques Grosset, and Dr. Assaf Gilad. They have been supportive and helpful throughout this process.

Dr. JongHee Lee was an important friend and mentor. He always knew when I needed his help as a mentor (trouble shooting an experiment) or as a friend (leaving the troubled experiment alone and going out for Korean BBQ instead). Dr. Christer Larsson, Dr. Nicole Ammerman, Dr. André Kübler, Dr. Ulas Bagci,

Kathryn Winglee, and Hui Yang were involved with the experimental design, lab work, and analysis. My success would not have been possible without them.

I would also like to thank Stephanie Chiang for her help in editing the thesis and also for her patience and support. Thanks to my parents, Carlos and Rosa Luna, and my brothers, Shawn and Chris for their constant support and encouragement as well.

Lastly, thank you to everyone who was not named but nonetheless have made a significant impact. I promise that it has not gone unnoticed or unappreciated.

Table of Contents

ABSTRACT II

ACKNOWLEDGEMENTS IV

TABLE OF FIGURES VIII

TABLE OF TABLES X

CHAPTER 1: INTRODUCTION 1

1.1 THE RABBIT MODEL OF CAVITARY TUBERCULOSIS 2

1.2 PET/CT IMAGING 4

1.3 INFECTIOUS DISEASE IMAGING 6

REFERENCES 9

FIGURES 12

CHAPTER 2: *IN VIVO* PREDICTION OF TUBERCULOSIS CAVITY FORMATION 24

ABSTRACT 24

INTRODUCTION 25

MATERIALS AND METHODS 26

RESULTS 28

DISCUSSION 33

REFERENCES 36

FIGURES 40

CHAPTER 3: RNA-SEQ OF HOST EXPRESSION PROFILE IN A RABBIT MODEL OF CAVITARY TUBERCULOSIS 57

ABSTRACT 57

INTRODUCTION 59

MATERIALS AND METHODS 61

RESULTS 65
DISCUSSION 70
REFERENCES 73
FIGURES 76
CHAPTER 4: SMALL MOLECULE INHIBITION OF MMP-1 ALTERS PATHOLOGY IN A RABBIT MODEL OF TUBERCULOSIS. 85
ABSTRACT 85
INTRODUCTION 87
METHODS 89
RESULTS 93
DISCUSSION 96
REFERENCES 98
FIGURES 101
APPENDIX- IMAGE PROCESSING OF CT AND PET IMAGES 113
ABSTRACT 113
INTRODUCTION 113
METHOD 1- ANNOTATION TOOL (NIH) 114
METHOD 2: AMIRA VISUALIZATION SCIENCES GROUP 117
REFERENCES 119
FIGURES 120
CURRICULUM VITAE 136

Table of Figures

FIGURE 1-1: ESTIMATED TB INCIDENCE RATE FOR 2012 12

FIGURE 1-2: TB PATHOGENESIS 13

FIGURE 1-3: CAVITY LESION IN RABBITS AND HUMANS 15

FIGURE 1-4: RABBIT CAVITY LESION 16

FIGURE 1-5: MMP DEGRADATION OF EXTRACELLULAR MATRIX 17

FIGURE 1-6: CT SCANNER SCHEMATIC 19

FIGURE 1-7: PET SCANNER SCHEMATIC 21

FIGURE 2-1: ALGORITHMS FOR PREDICTING CAVITARY DISEASE. 40

FIGURE 2-2: IMAGE SEGMENTATION AND REGISTRATION. 42

FIGURE 2-3: DENSITY CHANGE IN CAVITARY PROGRESSING AND NON-CAVITARY PROGRESSING GROUPS 44

FIGURE 2-4: CHANGE IN [^{18}F]-FDG SUVMAX BETWEEN CAVITARY PROGRESSING AND NON-CAVITARY PROGRESSING GROUPS OVER TIME. 46

FIG. 2-5: CHANGE IN TOTAL LUNG DENSITY OVER TIME. 47

FIG. 2-6: THE SUM OF DIFFERENCES AND SUM OF SUMS. 48

FIGURE 2-7: CHANGE IN LUNG DENSITY IN PET ROI. 49

FIGURE 2-8: CHANGE IN THE PROPORTION OF DENSELY CONSOLIDATED LUNG TISSUE. 50

FIGURE 2-9: AUC TEST FOR PREDICTING CAVITARY PROGRESSION 51

FIGURE 2-10: RABBIT CAVITY LESION. 53

EQUATION 1 55

EQUATION 2 55

FIGURE 3-1: RNA TISSUE SAMPLING 76

FIGURE 3-2: TUXEDO GLOBAL CLUSTERING 77

FIGURE 3-3: REACTOME IMMUNE RESPONSE GENE SET 78

FIGURE 3-4: IPA IFN-GAMMA NETWORK 79

FIGURE 3-5: IPA CAVITY SIGNALING......80

FIGURE 4-1: GROUP 1 STUDY OUTLINE......101

FIGURE 4-2: GROUP 1 CT DENSITY PLOTS......102

FIGURE 4-3: VASCULITIS......104

FIGURE 4-4: GROUP 2 STUDY OUTLINE......105

FIGURE 4-5: GROUP 2, 3D LUNG IMAGES......106

FIGURE 4-6: GROUP 2 CT DENSITY PLOTS......109

FIGURE 4-7: GROUP 2 LUNG AND LESION VOLUME......111

FIGURE 5-1: IMAGE COREGISTRATION......120

FIGURE 5-2: VOXEL SIZE......121

FIGURE 5-3: POINT SOURCE COREGISTRATION......122

FIGURE 5-4: VOXEL NORMALIZATION......123

FIGURE 5-5: ANNOTATION TOOL THRESHOLD......124

FIGURE 5-6: ANNOTATION TOOL REGION WALKING......125

FIGURE 5-7: ANNOTATION TOOL FINAL......126

FIGURE 5-8: AMIRA CT POINT SOURCE......127

FIGURE 5-9: AMIRA PET POINT SOURCE......128

FIGURE 5-10: AMIRA COREGISTRATION......129

FIGURE 5-11: AMIRA COREGISTRATION OVERLAY......130

FIGURE 5-12: AMIRA CT SEGMENTATION......131

FIGURE 5-13: AMIRA PATHOLOGIC LUNG SEGMENTATION......132

FIGURE 5-14: AMIRA PET SEGMENTATION......133

FIGURE 5-15: AMIRA HISTOGRAM......134

FIGURE 5-16: AMIRA HISTOGRAM FILE......135

Table of Tables

TABLE 1-1: ANIMAL MODELS OF CAVITATION.....22

TABLE 1-2: BACTERIA SPECIFIC PET PROBES.....23

TABLE 2-1: SENSITIVITY AND SPECIFICITY OF CAVITARY PREDICTIVE RADIOLOGY MARKERS.....56

TABLE 2-2: CONCEPT BOX.....56

TABLE 3-1: TOP 10 MOST UPREGULATED GENES PRESENT IN CAVITARY TISSUE.....81

TABLE 3-2: IPA CORE ANALYSIS FUNCTIONAL GENE SETS.....82

TABLE 3-3: IPA CORE ANALYSIS MOLECULES.....84

TABLE 4-1: CAVITY STATS.....112

Chapter 1: Introduction

Although tuberculosis is one of the oldest diseases known to affect man, it remains one of the major causes of morbidity and mortality worldwide [1]. Tuberculosis typically presents as a pulmonary infection and the disease is spread by aerosol transmission of the bacterial pathogen Mycobacterium tuberculosis. One third of the global population is estimated to be infected with latent tuberculosis. Individuals affected by latent tuberculosis do not have clinical symptoms and are not infectious. However, individuals with latent disease are at risk of developing active disease. Southeast Asia and Africa were responsible for 29% and 27% of total tuberculosis cases in 2012 **(Figure 1-1)**. Mortality is higher among men, but TB remains one of the top 10 killers globally for women. [2]

A standard six month, four drug antibiotic treatment regimen is recommended for drug susceptible cases; however, complications such as drug resistance or cavitary diseases can extend the treatment duration for up to two years [3]. There are three major factors that prolong the duration of treatment. One major challenge in shortening the treatment regimen is the successful killing of bacterial persisters, a subpopulation of bacteria that are able to survive in the presence of antibiotics. The persister population is thought to represent about 1% of the total bacterial population and requires prolonged treatment to ensure the sterilization of all bacteria [4, 5]. A deficiency of good biomarkers or sampling options is another challenge for rapidly assessing the successfulness of a treatment regimen, since sites of infection and disease burden are difficult to identify without robust biomarkers [6]. Lastly, tissue remodeling of the lung during the course of disease progression can lead to pathology that can have negative implications for drug distribution and penetration within lesions [7, 8]. While these three challenges are relevant to the study and treatment of tuberculosis, these are not unique to tuberculosis. This thesis will discuss advances in non-invasive imaging techniques that attempt to elucidate the pathogenesis of cavitary tuberculosis.

1.1 The rabbit model of cavitary tuberculosis

Mice, guinea pigs, rabbits, and non-human primates have been the traditional animal models for studying tuberculosis **(Table 1-1: Animal models of cavitation)**. Mice do not develop true granulomas which are one of the pathologic hallmarks of tuberculosis classically observed in humans. Granulomas are defined as densely organized cellular structures that are formed as a host immune response in an attempt to create a microenvironment that walls off the pathogen from the rest of the body **(Figure 1-2)**. Guinea pigs can develop granulomas, and the pathology is very similar to what is observed in humans; however, guinea pigs do not develop cavities. Rabbits and non-human primates both develop granulomas and cavities that are similar in pathology as to what is seen in humans, making these animals the better models for cavitary tuberculosis research **(Figure 1-3)** [9]. The rabbit model has historically been the most important model for the study of cavitary tuberculosis, and much of what is currently known about cavitary disease was studied in the rabbit model [9-13]. Rabbits provide the most accessible small animal model that is capable of modeling cavitary disease. However, the rabbit model does have its limitations, which are due to relatively few molecular and genetic tools available. After the rabbit genome became available though, the number of bioinformatic tools have expanded and the availability of the genome has now made global gene expression and systems biology studies possible through the use of microarrays or RNA-sequencing platforms [14-17].

The rate of cavity development, the number of cavities, and the frequency at which cavities develop is partially dependent of the species and strain of *Mycobacterium* that is used for infection. It is also possible to presenstitize rabbits, a process that makes rabbits hypersensitive to mycobacterial antigen, increasing the rate and frequency with which cavitary lesions develop [11, 13]. The work presented in this thesis is based on a presensitized rabbit model **(Figure 1-4)**.

One theory regarding the progression of cavitary tuberculosis is that the development of cavitary lesions is driven by the host immune response [11, 18, 19]. Presensitization of rabbits also offers support that these lesions are formed as a consequence of a host immune response. Cleavage and remodeling of the lung extracellular matrix, a necessity for cavity lesion formation, requires special proteases of the matrix metalloproteinase (MMP) class. These proteases are released during the inflammatory response and remodel the lung extracellular matrix. It is not believed that *Mycobacterium tuberculosis* has the capabilities to degrade the lung extracellular matrix and therefore the development of the cavitary lesions are driven by the host immune response **(Figure 1-5)** [20-24].

1.2 PET/CT imaging

X-rays were first discovered by Wilhelm Röntgen in 1895 and these discoveries would later lead to a Nobel prize in 1901. It did not take long for the X-rays to be applied to the health sciences and the field of radiology began in its infancy in the early 20th century.

Computed tomography (CT) imaging is a form of x-ray imaging that allows for the acquisition of multiple X-ray slices and then the subsequent reconstruction of the image stack to generate a 3D data set with information in the x, y, and z planes. Briefly, the CT scanner consists of an X-ray source located opposite a detector inside of a doughnut shaped housing apparatus. The subject to be scanned is placed inside the scanner and is situated between the X-ray source and the detector. The X-ray source and detector rotate around the subject and acquire multiple scans. The data set of 2D X-ray scans is then reconstructed into voxels, a unit of value that consists of volume and 3D spatial information **(Figure 1-6)**. These voxels are then compiled to make the 3D reconstructed images.

The data acquired from a CT scan is quantifiable. Each voxel represents a numerical value that is representative of X-ray attenuation. The numeric values are defined in the Hounsfield unit (HU) scale. The formula for determining the Hounsfield unit is determined by *Equation 1*. The value “0” on the Hounsfield scale is defined as the attenuation of water and the value of “-1000” is defined as the attenuation of air. Measurements made by the CT scanner are important for providing structural information. It should be noted that a CT scan requires many X-rays for the reconstruction of a 3D image, and therefore a patient receiving a CT scan receives more radiation as compared to a standard X-ray.

Equation (1) $\mathbf{HU} = [\boldsymbol{\mu}(\mathbf{x}) - \boldsymbol{\mu}(\mathbf{water})] \div \boldsymbol{\mu}(\mathbf{water})$

A positron emission tomography (PET) scan is a functional radioimaging technique. PET scans require the use of a radioactive tracer. The tracer provides both the signal and also the target specificity. The housing apparatus for a PET scanner is similar to a CT scanner, expect a PET scanner does not have a radiation source. The sole radiation source for a PET scan is the administered PET tracer.

The decay of the radiotracer produces a positron. Positrons and electrons annihilate and produce two high energy gamma rays that travel in opposite directions at an angle of approximately 180 degrees relative to each other

(Figure 1-7). The instruments are able to take advantage of each annihilation event producing two decay products that travel in nearly opposite directions by creating cutoffs of what can be considered a true signal as opposed to random background noise. These correction factors increase the sensitivity and specificity of the signal detected and also aid in determining the spatial origin of where an annihilation event occurs. The gamma rays are not able to be directly measured and therefore, the quantification of the gamma rays requires the aid of scintillation crystals and photomultiplier tubes. The scintillation crystals convert the high energy gamma rays into photons that are passed along to the photomultiplier tube. The photomultiplier tube converts the photons into an electrical current and the electrical current can then be measured and quantified.

1.3 Infectious disease imaging

CT provides a tool to visualize structural changes in anatomy during disease progression. However, it should be noted that CT is not capable of visualizing individual pathogens, nor is it able to distinguish all stages of infection. Appreciable structural changes at the initial stage of infection would most likely be below the limit of detection. Similarly, late stage changes in the resolving of the disease would also be difficult to distinguish as it is likely that structural changes would linger beyond the clearance of the pathogen. The utility of CT can therefore be summarized as being the most useful during active disease when structural changes are occurring and are visible. CT would also be useful in monitoring the decrease in disease related pathology as an indicator of the transition from the active stage to the resolving stage of the disease, but CT would not be an effective end point measure of disease.

Molecular imaging techniques and tools for infectious disease imaging, such as PET imaging, have traditionally been largely focused on measuring the process of inflammation. Inflammation is a general process that includes changes such as the increased vascular permeability and the recruitment of immune cells. Examples of these imaging techniques are the *ex-vivo* labeling of white blood cells and then tracking their migration, the labeling of macromolecules and measuring increased vascular permeability, and the labeling of circulating activated white blood cells *in-vivo.* It is important to note that these techniques do not directly label the pathogen, but rely on the indirect labeling of the host immune cells and the concentration of the probe at sites of inflammation [25].

Recently, the use of $[^{18}F]$-2-fluoro-deoxy-D-glucose ($[^{18}F]$-FDG) has gained popularity for its application to infectious disease imaging. The tracer is a modified glucose sugar and is taken up by the GLUT-1 transporter. The $[^{18}F]$-FDG sugar is then phosphorylated by hexokinase and the product, $[^{18}F]$-FDG-6-phosphate, is not able to undergo further metabolism by the cell and therefore is trapped inside the cell [26]. Clinical use of $[^{18}F]$-FDG first began with the oncology field. It was observed that cancer cells were highly metabolically active and would readily uptake higher amounts of glucose. In the context of infectious diseases imaging, [^{18}F]-FDG is still labeling highly metabolically cells but the cells being labeled are host immune cells such as neutrophils and macrophages [27]. Recent advances have been made in the development of pathogen specific tracers. The most common approach to date has been the modification of antibiotics to include a radioisotope **(Table 1-2)** [28-30].

There remains a need for improved non-invasive imaging probes and imaging techniques for infectious disease imaging. While the probes listed in **Table 1-2** are a significant advancement on the previous generation of probes targeting the inflammation process, these probes are still not capable of differentiating bacterial species. The potential benefits of improved non-invasive imaging would include the ability for rapid localization of the site of infection, diagnosis of the pathogen, and the rapid assessment of treatment efficacy among other benefits.

References

1. Nerlich, A. G., Haas, C. J., Zink, A., Szeimies, U., and Hagedorn, H. G. (1997). Molecular evidence for tuberculosis in an ancient Egyptian mummy. Lancet *350*, 1404.

2. World Health Organization (2013). Global tuberculosis report 2013.

3. Blumberg, H. M., Burman, W. J., Chaisson, R. E., Daley, C. L., Etkind, S. C., Friedman, L. N., Fujiwara, P., Grzemska, M., Hopewell, P. C., Iseman, M. D., et al. (2003). American Thoracic Society/Centers for Disease Control and Prevention/Infectious Diseases Society of America: treatment of tuberculosis. Am J Respir Crit Care Med *167*, 603–662.

4. Jindani, A., Doré, C. J., and Mitchison, D. A. (2003). Bactericidal and sterilizing activities of antituberculosis drugs during the first 14 days. Am J Respir Crit Care Med *167*, 1348–1354.

5. Ahmad, Z., Klinkenberg, L. G., Pinn, M. L., Fraig, M. M., Peloquin, C. A., Bishai, W. R., Nuermberger, E. L., Grosset, J. H., and Karakousis, P. C. (2009). Biphasic kill curve of isoniazid reveals the presence of drug-tolerant, not drug-resistant, Mycobacterium tuberculosis in the guinea pig. J Infect Dis *200*, 1136–1143.

6. Wallis, R. S., Kim, P., Cole, S., Hanna, D., Andrade, B. B., Maeurer, M., Schito, M., and Zumla, A. (2013). Tuberculosis biomarkers discovery: developments, needs, and challenges. Lancet Infect Dis *13*, 362–372.

7. Prideaux, B., Dartois, V., Staab, D., Weiner, D. M., Goh, A., Via, L. E., Barry, C. E., and Stoeckli, M. (2011). High-sensitivity MALDI-MRM-MS imaging of moxifloxacin distribution in tuberculosis-infected rabbit lungs and granulomatous lesions. Analytical chemistry *83*, 2112–2118.

8. Kjellsson, M. C., Via, L. E., Goh, A., Weiner, D., Low, K. M., Kern, S., Pillai, G., Barry, C. E., and Dartois, V. (2012). Pharmacokinetic evaluation of the penetration of antituberculosis agents in rabbit pulmonary lesions. Antimicrob Agents Chemother *56*, 446–457.

9. Helke, K. L., Mankowski, J. L., and Manabe, Y. C. (2006). Animal models of cavitation in pulmonary tuberculosis. Tuberculosis *86*, 337–348.

10. Dannenberg, A. M. (2006). Pathogenesis of Human Pulmonary Tuberculosis: Insights from the Rabbit Model. ASM Press.

11. Yamamura, Y., YASAKA, S., YAMAGUCHI, M., ENDO, K., IWAKURA, H., NAKAMURA, S., and Ogawa, Y. (1954). Experimental formation of the tuberculous cavity in the rabbit's lung; experimental study on the tuberculous allergy. I. Kekkaku *29*, 143–6– English abstract– 153–4.

12. Yamamura, Y., Ogawa, Y., Yamagata, H., and Yamamura, Y. (1968). Prevention of tuberculous cavity formation by immunosuppressive drugs. The American Review of respiratory disease *98*, 720–723.

13. Nedeltchev, G. G., Raghunand, T. R., Jassal, M. S., Lun, S., Cheng, Q.-J., and Bishai, W. R. (2009). Extrapulmonary dissemination of Mycobacterium bovis but not Mycobacterium tuberculosis in a bronchoscopic rabbit model of cavitary tuberculosis. *77*, 598–603.

14. Subbian, S., Tsenova, L., Yang, G., O'Brien, P., Parsons, S., Peixoto, B., Taylor, L., Fallows, D., and Kaplan, G. (2011). Chronic pulmonary cavitary tuberculosis in rabbits: a failed host immune response. Open Biol *1*, 110016.

15. Subbian, S., Bandyopadhyay, N., Tsenova, L., O Brien, P., Khetani, V., Kushner, N. L., Peixoto, B., Soteropoulos, P., Bader, J. S., Karakousis, P. C., et al. (2013). Early innate immunity determines outcome of Mycobacterium tuberculosis pulmonary infection in rabbits. Cell Commun. Signal *11*, 60.

16. Subbian, S., O'Brien, P., Kushner, N. L., Yang, G., Tsenova, L., Peixoto, B., Bandyopadhyay, N., Bader, J. S., Karakousis, P. C., Fallows, D., et al. (2013). Molecular immunologic correlates of spontaneous latency in a rabbit model of pulmonary tuberculosis. Cell Commun. Signal *11*, 16.

17. Subbian, S., Tsenova, L., O'Brien, P., Yang, G., Kushner, N. L., Parsons, S., Peixoto, B., Fallows, D., and Kaplan, G. (2012). Spontaneous Latency in a Rabbit Model of Pulmonary Tuberculosis. Am J Pathol.

18. Yamamura, Y., YASAKA, S., NAKAMURA, S., Ogawa, Y., YAMAGUCHI, M., ENDO, K., and IWAKURA, H. (1954). Experimental studies on the tuberculous allergy. III. Experimental formation of the tuberculous cavity in the rabbit's lung by killed tubercle bacillus. Kekkaku *29*, 361–7– English abstract– 376–7.

19. Yamamura, Y., Ogawa, Y., Maeda, H., and Yamamura, Y. (1974). Prevention of tuberculous cavity formation by desensitization with tuberculin-active peptide. The American Review of respiratory disease *109*, 594–601.

20. Elkington, P., Shiomi, T., Breen, R., Nuttall, R. K., Ugarte-Gil, C. A., Walker, N. F., Saraiva, L., Pedersen, B., Mauri, F., Lipman, M., et al. (2011). MMP-1 drives immunopathology in human tuberculosis and transgenic mice. J. Clin. Invest. *121*, 1827–1833.

21. Elkington, P. T., D'Armiento, J. M., and Friedland, J. S. (2011). Tuberculosis immunopathology: the neglected role of extracellular matrix destruction. Science Translational Medicine *3*, 71ps6–71ps6.

22. Walker, N. F., Clark, S. O., Oni, T., Andreu, N., Tezera, L., Singh, S., Saraiva, L., Pedersen, B., Kelly, D. L., Tree, J. A., et al. (2012). Doxycycline and HIV infection suppress tuberculosis-induced matrix metalloproteinases. Am J Respir Crit Care Med *185*, 989–997.

23. Ugarte-Gil, C. A., Elkington, P., Gilman, R. H., Coronel, J., Tezera, L. B., Bernabe-Ortiz, A., Gotuzzo, E., Friedland, J. S., and Moore, D. A. J. (2013). Induced sputum MMP-1, -3 & -8 concentrations during treatment of tuberculosis. PLoS ONE *8*, e61333.

24. Tadokera, R., Meintjes, G. A., Wilkinson, K. A., Skolimowska, K. H., Walker, N., Friedland, J. S., Maartens, G., Elkington, P. T. G., and Wilkinson, R. J. (2013). Matrix metalloproteinases and tissue damage in HIV-tuberculosis immune reconstitution inflammatory syndrome. Eur J Immunol.

25. Becker, W., and Meller, J. (2001). The role of nuclear medicine in infection and inflammation. Lancet Infect Dis *1*, 326–333.

26. Abouzied, M. M., Crawford, E. S., and Nabi, H. A. (2005). 18F-FDG imaging: pitfalls and artifacts. J Nucl Med Technol *33*, 145–55; quiz 162–3.

27. Goo, J. M., Im, J. G., Do, K. H., Yeo, J. S., Seo, J. B., Kim, H. Y., and Chung, J. K. (2000). Pulmonary tuberculoma evaluated by means of FDG PET: findings in 10 cases. Radiology *216*, 117–121.

28. Signore, A., Mather, S. J., Piaggio, G., Malviya, G., and Dierckx, R. A. (2010). Molecular imaging of inflammation/infection: nuclear medicine and optical imaging agents and methods. Chem. Rev. *110*, 3112–3145.

29. Weinstein, E. A., Liu, L., Ordonez, A. A., Wang, H., Hooker, J. M., Tonge, P. J., and Jain, S. K. (2012). Noninvasive Determination of 2-[18F]-Fluoroisonicotinicacid hydrazide Pharmacokinetics by Positron Emission Tomography in Mycobacterium tuberculosis Infected Mice. Antimicrob Agents Chemother.

30. Davis, S. L., Be, N. A., Lamichhane, G., Nimmagadda, S., Pomper, M. G., Bishai, W. R., and Jain, S. K. (2009). Bacterial thymidine kinase as a non-invasive imaging reporter for Mycobacterium tuberculosis in live animals. PLoS ONE *4*, e6297.

Figures

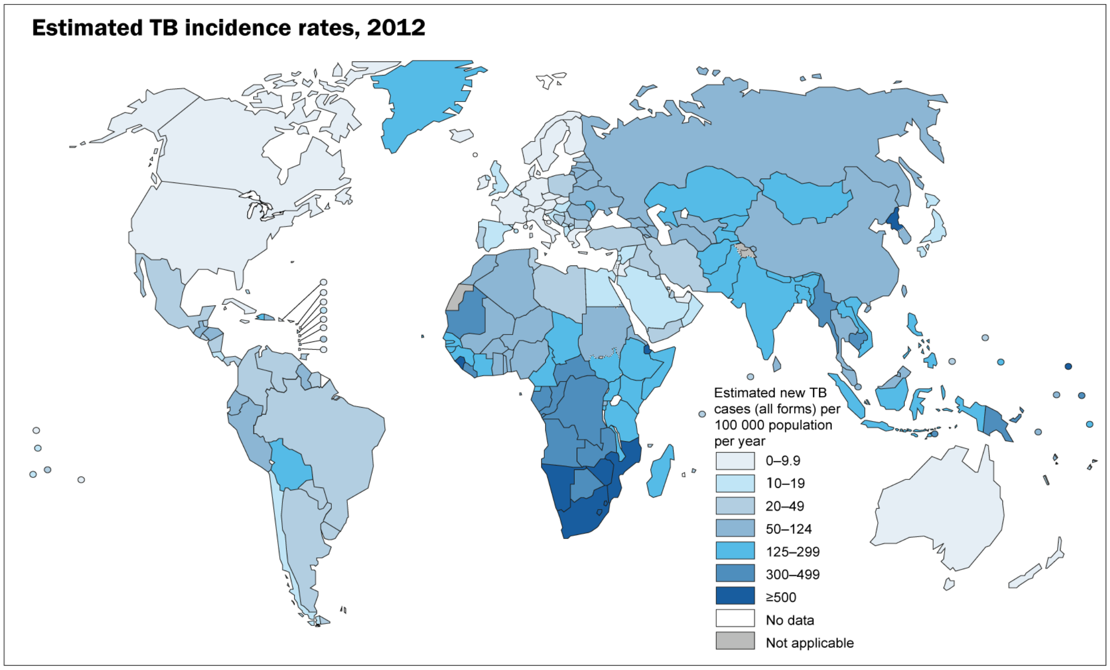

The boundaries and names shown and the designations used on this map do not imply the expression of any opinion whatsoever on the part of the World Health Organization concerning the legal status of any country, territory, city or area or of its authorities, or concerning the delimitation of its frontiers or boundaries. Dotted and dashed lines on maps represent approximate border lines for which there may not yet be full agreement.

Data Source: *Global Tuberculosis Report 2013*. WHO, 2013.

© WHO 2013. All rights reserved.

World Health Organization

Figure 1-1: Estimated TB incidence rate for 2012

The highest density of new TB cases were reported from Africa. India is the country with highest total number of new TB cases and represents approximately 29% of all new TB cases. The United States would not be considered a TB endemic country. There were about 1.3 million deaths due to TB in 2012.

Figure 1-2: TB pathogenesis

Inhaled bacteria are first phagocytosed by alveolar macrophages. This is followed by the recruitment of additional host immune cells to contain the infection in a process called granuloma formation. In the host that is resistant to cavitary lesions, the granuloma serves to isolate the encompassed bacteria in a microenvironment that is isolated from the rest of the host. It is possible for bacteria to persist and survive in this granuloma structure. In the susceptible host, the granuloma is unable to contain the replication of the bacteria. The bacteria are able to replicate to high numbers in the caseous center of the lesion. Eventually the structure of the lesion deteriorates and the lesion ruptures which allows the release of free extracellular bacteria into the airway. It is important to note that the pattern of lesion development should result in an increasingly dense structure prior to cavitation and after cavitation occurs the lesion should become a decreasingly dense structure.

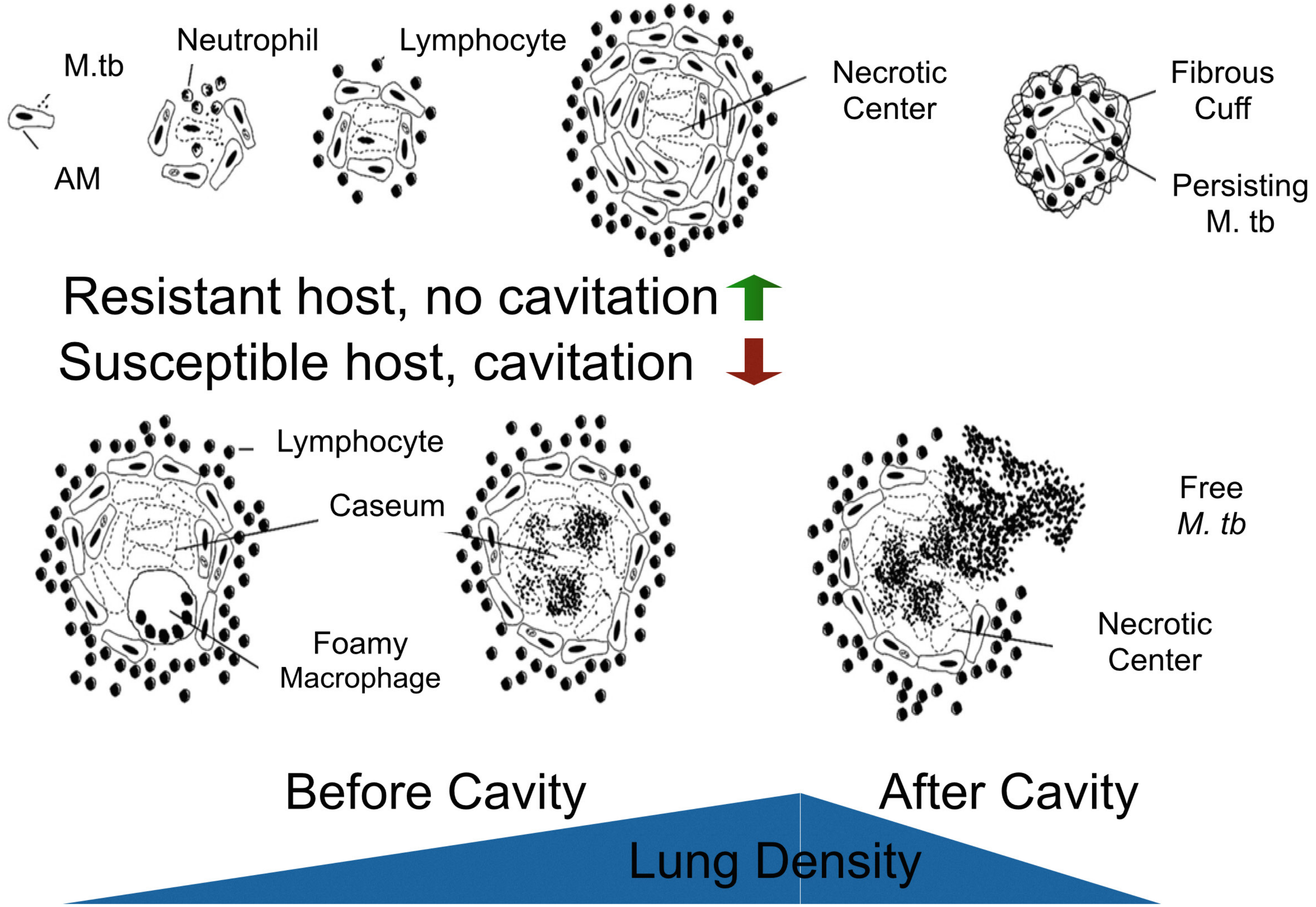

Resistant host, no cavitation ↑

Susceptible host, cavitation ↓

Before Cavity

After Cavity

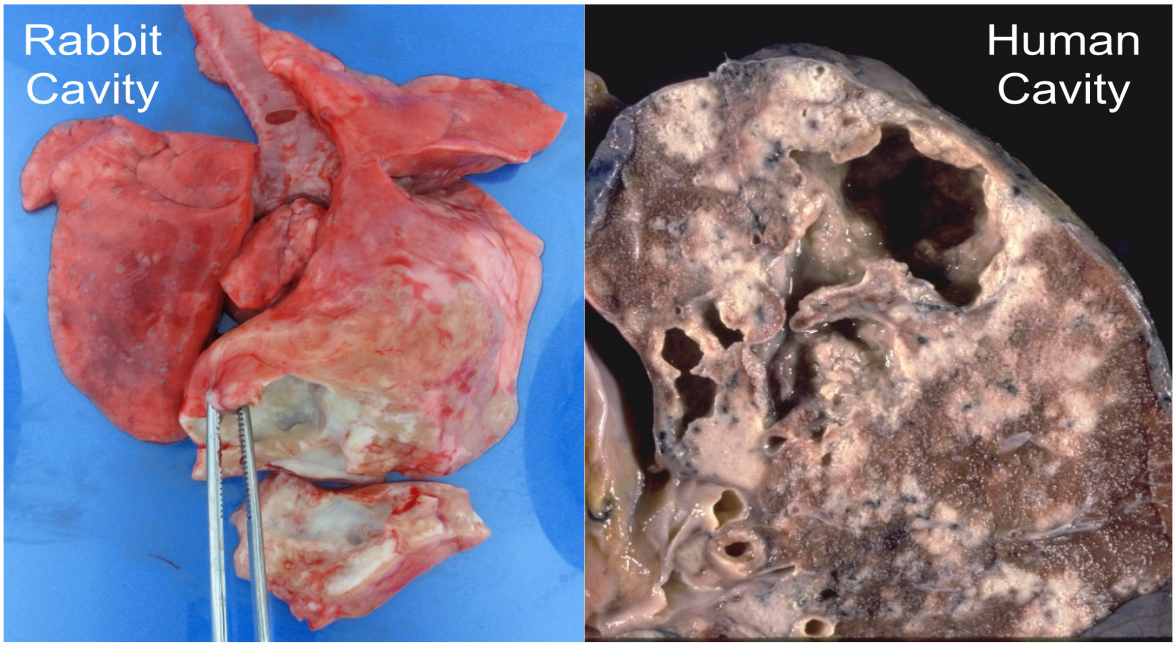

Figure 1-3: Cavity lesion in rabbits and humans

Cavitary lesions in rabbits is similar to the cavitary lesions that develop in humans. Tuberculosis cavity formation results in the formation of large air filled structures that are identifiable by gross pathology. Bacteria are able to replicate to high numbers in the caseous cavity space and rupture of the cavity wall into the airway allows for direct access of the bacilli to the airway which is an important step for disease transmission.

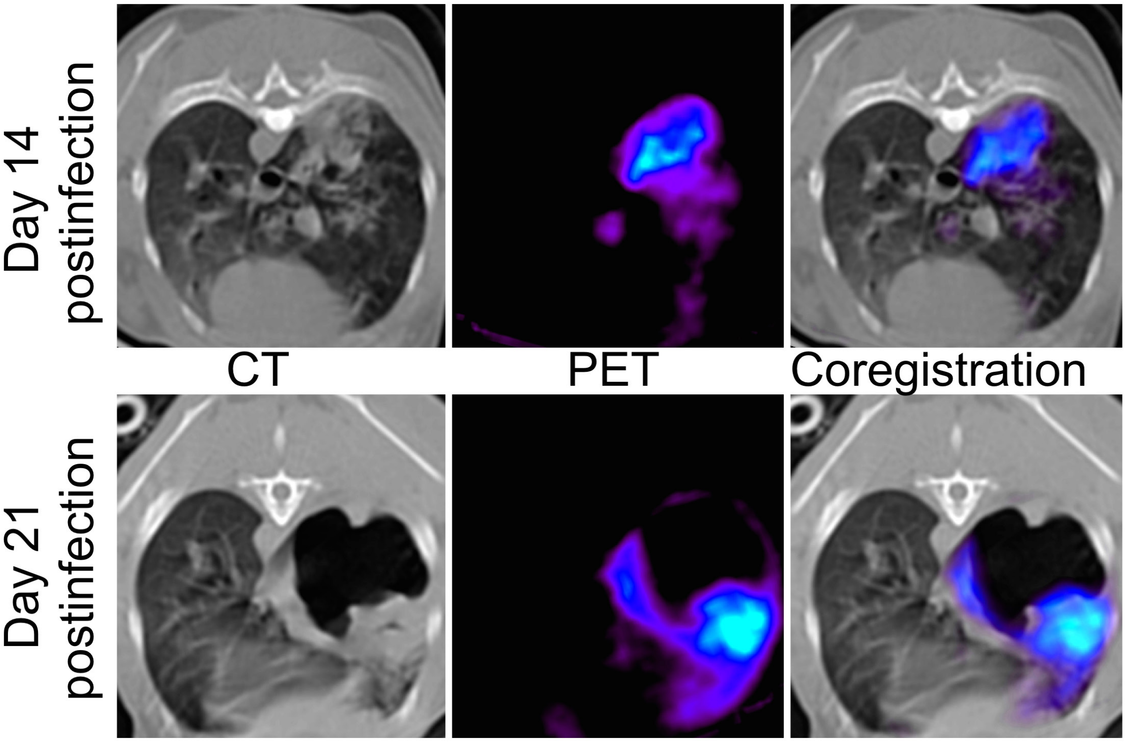

Figure 1-4: Rabbit cavity lesion

CT and PET scans were taken of the same animal at pre-cavitation and post-cavitation timepoints. A dense lesion that shows high [^{18}F]-FDG uptake is observed in the top right portion of the lung. This lesion then goes on to cavitate within the next 7 days. After cavitation occurs, the cavity wall still shows high uptake of [^{18}F]-FDG tracer. The process of presensitizing the rabbits allows for a more rapid development of cavitary lesion development and also development of lesions in a higher proportion of rabbits than what may be observed in non-sensitized rabbits.

Figure 1-5: MMP degradation of extracellular matrix

Cavitary lesions develop as result of extracellular matrix degradation. Degradation of the host extracellular matrix is believed to be driven by the host matrix metalloproteinase enzymes as shown by the pathway on the right side. The left hand pathway is the classical description of cavitary formation, but the classic description does not detail how the extracellular matrix is cleaved. Necrosis is not a sufficient mechanism to degrade the extracellular matrix. Elkington, P. T., D'Armiento, J. M., and Friedland, J. S. (2011). Tuberculosis immunopathology: the neglected role of extracellular matrix destruction. Science Translational Medicine 3, 71ps6–71ps6.

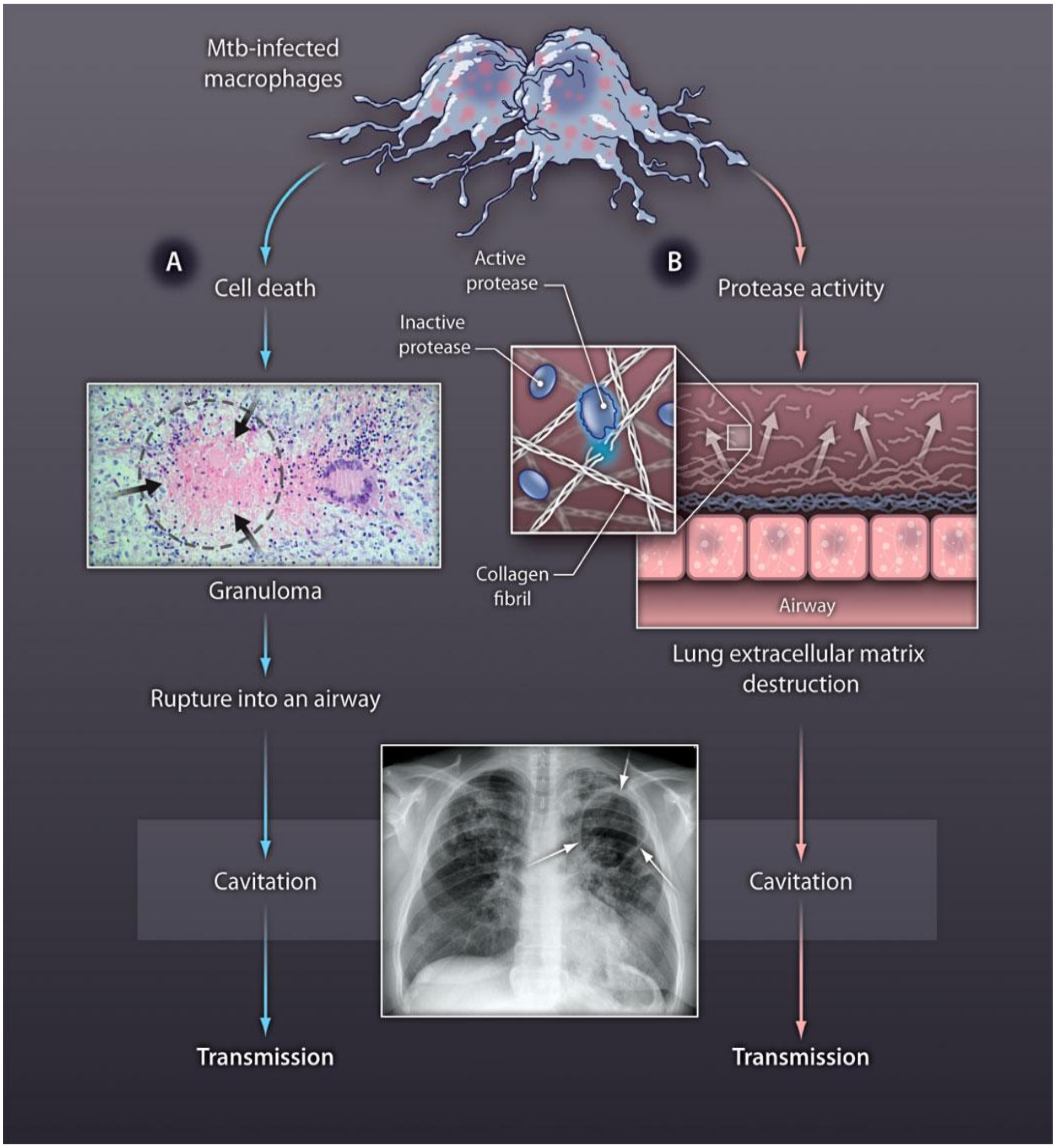
Mtb-infected macrophages
A
Cell death
Active protease
B
Protease activity
Inactive protease
Granuloma
Collagen fibril
Airway
Lung extracellular matrix destruction
Rupture into an airway
Cavitation
Cavitation
Transmission
Transmission

Figure 1-6: CT scanner schematic

Schematic of a CT scanner. The X-ray source is housed opposite the detector in a doughnut shaped setup. The subject is placed on a bed in between the the X-ray source and detectors in a stationary position. The X-ray source and detector rotate around the subject acquiring multiple X-rays during the course of the rotation. The reconstructed stack of images is then used to create a 3D visualization of the subject. Matter which is of higher density will attenuate the X-ray more compared to matter which is of a lower density. X-ray attenuation is represented by the Hounsfield unit (HU) scale with water and air defined as 0 HU and -1000 HU respectively. Reprinted from Goldman, L. W. (2007). Principles of CT and CT technology. J Nucl Med Technol *35*, 115–28– quiz 129–30.

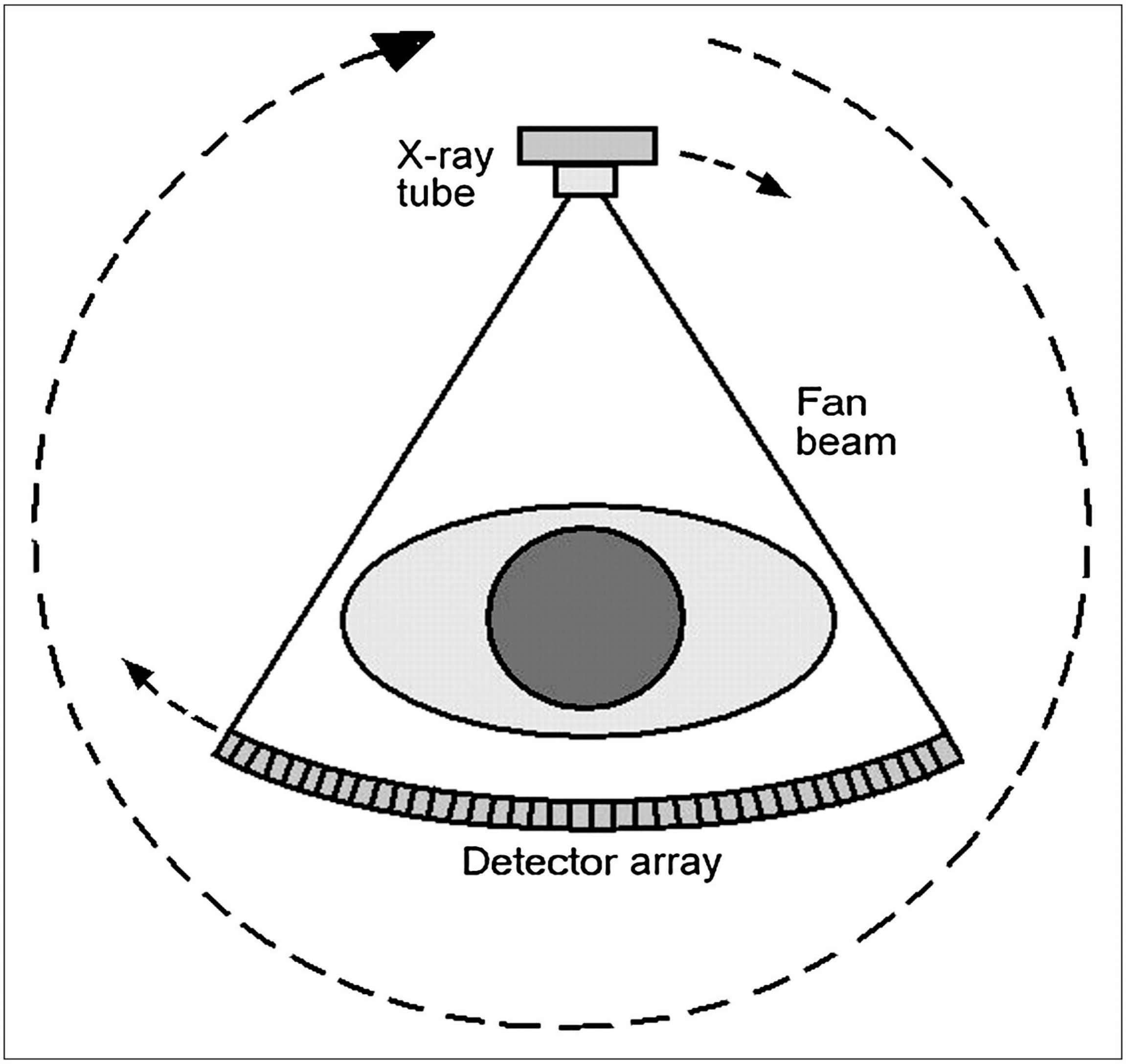
X-ray tube
Fan beam
Detector array

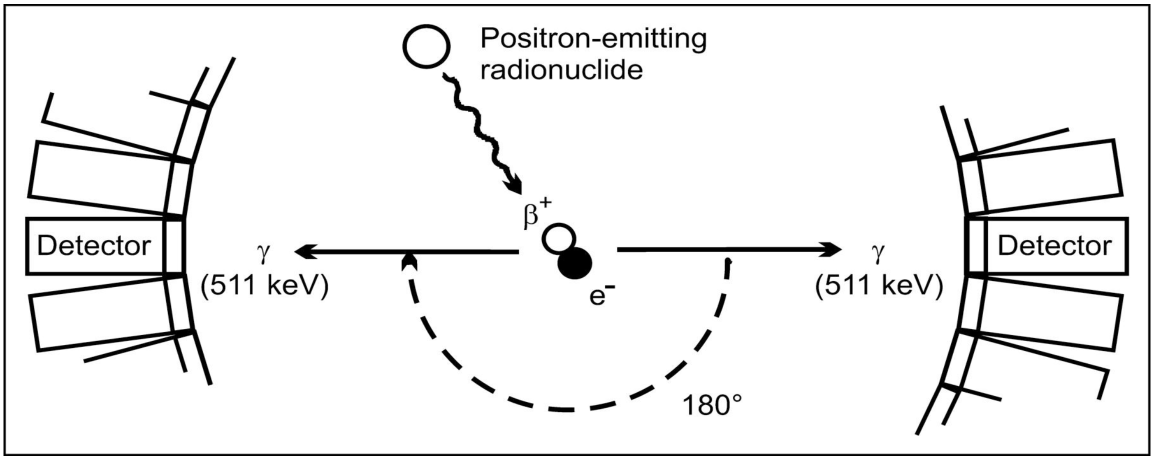

Figure 1-7: PET scanner schematic

Schematic of a PET scanner. A positron is formed during the decay of the radioisotope and the resulting positron collides with an electron. This annihilation event is detected by scintillation crystals that convert the high energy gamma radiation into photons. The photons are the quantified by photomultiplier tubes. The source of the radionuclide with vary depending on the imaging tracer utilized. Image reprinted from Verel, I., Visser, G. W. M., and van Dongen, G. A. (2005). The promise of immuno-PET in radioimmunotherapy. Journal of Nuclear Medicine *46 Suppl 1*, 164S–71S.

Table 1-1: Animal models of cavitation

The development of cavitary lesions is one of the hallmark characteristics of human tuberculosis. Rabbits are the smallest laboratory animal that develop cavitary disease. The frequency and rate of cavitation in rabbits can be increased by presensitizing rabbits to *mycobacterium* prior to infection. Mice do not develop granulomas or cavitary lesions. The table was reprinted from Helke, K. L., Mankowski, J. L., and Manabe, Y. C. (2006). Animal models of cavitation in pulmonary tuberculosis. Tuberculosis *86*, 337–348.

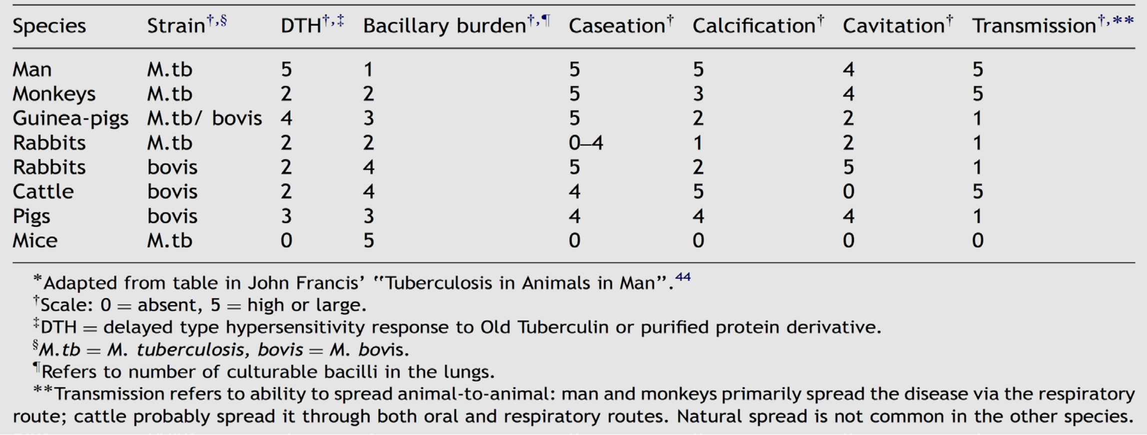

Species	Strain[†,§]	DTH[†,‡]	Bacillary burden[†,¶]	Caseation[†]	Calcification[†]	Cavitation[†]	Transmission[†,**]
Man	M.tb	5	1	5	5	4	5
Monkeys	M.tb	2	2	5	3	4	5
Guinea-pigs	M.tb/ bovis	4	3	5	2	2	1
Rabbits	M.tb	2	2	0–4	1	2	1
Rabbits	bovis	2	4	5	2	5	1
Cattle	bovis	2	4	4	5	0	5
Pigs	bovis	3	3	4	4	4	1
Mice	M.tb	0	5	0	0	0	0

[*] Adapted from table in John Francis' "Tuberculosis in Animals in Man".[44]

[†] Scale: 0 = absent, 5 = high or large.

[‡] DTH = delayed type hypersensitivity response to Old Tuberculin or purified protein derivative.

[§] *M.tb* = *M. tuberculosis, bovis* = *M. bovis*.

[¶] Refers to number of culturable bacilli in the lungs.

[**] Transmission refers to ability to spread animal-to-animal: man and monkeys primarily spread the disease via the respiratory route; cattle probably spread it through both oral and respiratory routes. Natural spread is not common in the other species.

Table 1-2: Bacteria specific PET probes

Below is a table of microbial specific PET probes. The majority of the probes have used known antibiotics as the backbone to provide specificity for the PET tracers. Several of the tracers listed below provide specificity at the genus level, but no tracer currently provides specificity at the species level.

Probe	**Target**
ethambutol	mycobacteria
isoniazid	mycobacteria
UBI 29-41	bacteria, fungus
FIAU	bacteria, herpes virus
ciprofloxacin	bacteria
fleroxacin	bacteria
trovafloxacin	bacteria

Chapter 2: *In vivo* Prediction of Tuberculosis Cavity Formation

Abstract

Rationale: Cavity tuberculosis is a risk factor for transmission and antibiotic treatment failure. There are no clinical tests available that test for the risk of cavitary lesion development. **Objectives:** To define a non-invasive imaging algorithm that is predictive of cavitary lesion development using a rabbit model of cavitary tuberculosis. **Methods:** We conducted a training study in which we collected and analyzed 114 PET/CT imaging data sets. We designed our predictive algorithms based on the data from this training data set and then validated our algorithms on a test data set collected from a second rabbit study consisting of 38 PET/CT imaging data sets. **Measurements and Main Results:** In the test data set, the PET ROI predicted cavitary disease with 100% sensitivity and 76% specificity and use of the CT ROI predicted cavitary disease with 83.3% sensitivity and 76.9% specificity. **Conclusions:** We were able to predict the development of cavitary lesions 1 week in advance. Our results show that restricting our analysis to regions with high [^{18}F]-FDG uptake provided the best combination of sensitivity and specificity. Inclusion of additional criteria to improve the predictive power of the algorithm warrants further study.

Introduction

In 2011, tuberculosis (TB) was responsible for an estimated 1.4 million deaths [1]. *Mycobacterium tuberculosis (M. tb)* is the primary etiological agent of TB in humans [2]. The initial infection is usually cleared or otherwise contained by the host immune system in a granuloma. Cavities evolve when solid caseous necrotic granulomas liquefy [3, 4]. Cavities are a risk factor for disease transmission [5-9]. The tissue destruction that results from cavitation contributes to the morbidity and mortality of TB [4, 10-12]. Cavitary disease is also an indicator of treatment failure and disease relapse [9, 13-15].

There are no clinical tests that are designed to assay the risk of cavitary lesion development and thus there is a need for markers to address this shortcoming [16-19]. Imaging markers provide an attractive option due to their benefit of providing a real-time, non-invasive tool. Additionally, non-invasive imaging tests allow for monitoring disease progression within a patient over time.

We used a rabbit cavitary model of TB to develop imaging markers predictive of cavitary lesion development. In this study, we demonstrate that while inflammation, as measured by [^{18}F]-fluorodeoxyglucose ([^{18}F]-FDG) uptake does not positively correlate with cavitary disease, changes in lung density as measured by CT are predictive of cavitary lesion development. We believe this novel method can be used as a non-invasive tool to analyze the progression of

TB disease and to identify the population most at risk for developing cavitary lesions. Such imaging biomarkers could shorten the time and cost of TB drug trials and are valuable in evaluating therapeutics which target the cavitation process.

Materials and Methods

Ethics statement

All animal experiments were carried out in strict accordance with the recommendations in the “Guide for the Care and Use of Laboratory Animals of the National Institutes of Health” and all procedures were approved by the Johns Hopkins University Animal Care and Use Committee.

Modified rabbit cavitary model

Sensitization and infection of New Zealand White female rabbits were done as previously described [20]. Briefly, rabbits received 5 separate injections of 10^8 CFUs of heat killed *M. bovis* Ravenel. Twenty-five days after the final injection the animals were given a skin test using purified protein derivative [PPD] to measure hypersensitivity. Positivity was defined as any measurable induration. Animals which did not convert their skin test were still included in this study. Following the skin test results, rabbits were challenged with 10^4 live *M. tuberculosis* H37Rv bacilli. The bacterial suspension was delivered to the right lower lung lobe by bronchoscopy. Inoculum dose was determined by plating the inoculum on 7H11 selective plates.

[^{18}F]-FDG PET/CT imaging

Rabbits were anesthetized with ketamine (20 mg/kg), xylazine (5 mg/kg), and acepromazine (10 mg). Animals were maintained under 3 L/min O_2 and 1% isoflurane for the duration of the imaging. Because the imaging facility is located in a BSL-2 facility, the infected animals were placed into a biosafety imaging chamber (Mediso). This chamber allowed for the filtration of gas exchange and for the safe transport of the animal. 2 mCi of [^{18}F]-FDG was administered intravenously by the marginal ear vein. PET scans were acquired on a Philips Mosaic PET scanner. 45 minutes post injection, PET data was acquired by a 30 minute static scan. CT scans were performed with a clinical 8-slice CereTom CT (NeuroLogica) scanner.

Imaging processing, segmentation, coregistration, and ROIs

An overview of the image processing is summarized in **figure 2-1 and figure 2-2**. Fiducial markers were used to coregister PET scans to the CT scans. A group of 5 thin-walled PCR tubes containing 5 µCi of [^{18}F]-FDG were used as the fiducial markers. Rigid image coregistration was done using AMIRA (Visualization Science Group). Image segmentation was done using both AMIRA and the ANNOTATION TOOL (NIH) software packages. Methods for image segmentation were followed as described by *Bagci et al.* [21]. Briefly, lung segmentation was conducted by an adaptive region growing algorithm in which the user defined voxels were labeled as being "lung" or "non-lung" regions [22]. Explicitly labeled voxels are used to determine the status of the unlabeled voxels. Furthermore, manual interaction for refinement of dense pathological regions within the lung was also possible using the brush tools or random walk region segmentation algorithm [21, 23]. The segmented lung regions were then converted into binary masks such that non-lung regions were removed from the raw images. PET ROIs were defined by thresholding the top 5 percentile of [^{18}F]-FDG uptake. CT ROIs were defined as being between −200:200 Hounsfield HU.

Statistical analyses.

Statistical analysis was done using PRISM (GraphPad Software). For analysis which consisted of comparing multiple time points, statistical significance was determined by a repeated measures 1-way ANOVA with a Bonferroni's multiple comparison test. For pairwise analysis, a 2-tailed, unpaired student T-test was done. P values of less than 0.05, 0.01, and 0.001 were summarized as *, **, and *** respectively. P values of less than 0.05 were considered non-significant.

Results

Rabbit model of cavitary disease training set. We used a modified version of the rabbit cavitary model reported by Nedeltchev *et al* [20] which produced cavitation in about 50% of animals within 5 weeks post-infection. Twelve rabbits were presensitized with a series of 5 injections of 10^8 heat killed *M. bovis* bacilli suspended in incomplete Freund's adjuvant and infected with 10^4 colony forming units (CFUs) of *M. tuberculosis* H37Rv. The rabbits underwent PET/CT scans at the following time points: pre-infection, and on days 14, 21, 28, 35, 70, and 140 post-infection. In total 114 image sets, comprised of 57 PET and 57 CT data sets, were collected and analyzed. Cavitary progressive disease was defined by visual assessment of a cavity structure during necropsy or observing a region with density value less than −900 Hounsfield units (HU) as measured by CT. Animals in which no cavitary disease was observed were labeled as having non-cavitary progressive disease.

PET and CT regions of interest (ROI). Raw PET and CT images were acquired, coregistered, and then segmented. The PET ROI was defined as a global threshold of the top 5 percentile of [^{18}F]-FDG uptake, and the CT ROI was defined by the density range of -200:200 HU. The PET and CT ROIs were applied to the segmented PET and CT data sets, respectively **(Figure 2-1, Figure 2-2A)**. The PET ROI can be summarized as defining a region with high inflammation; and the CT ROI can be summarized as defining a consolidated region. Both regions identify abnormalities that can be interpreted as signs of disease. A summary of the main types of pathology that are visualized by CT are summarized in **Figure 2-3A**. Because PET and CT images have been coregistered, application of the ROI is not restricted to the data set used to generate the ROI. For example the spatial volume defined by the PET ROI can be applied to the CT image set and also the PET data set **(Figure 2-2B).**

Uptake of [^{18}F]-FDG was not discriminative for cavitary progressing disease versus non-cavitary progressing disease. It has been previously reported that uptake of [^{18}F]-FDG is a marker of inflammation and disease progression both animal models and also human TB disease. Additionally, uptake of [^{18}F]-FDG has been shown to be useful in measuring antibiotic treatment efficacy [24-26]. To investigate whether the uptake of [^{18}F]-FDG can differentiate cavitary progressive from non-cavitary progressive disease, the standardized uptake value maximum (SUVmax) was measured for each animal using the PET ROI. No significant difference could be found in cavitary progressing animals compared to non-cavitary progressing animals on day 14, which was seven days prior to the time of cavitation for 80% of the rabbits **(Figure 2-4A)**.

We then measured the total distribution of [^{18}F]-FDG standardized uptake within the segmented lung field on day 14 **(Figure 2-4B)**. There was no significant difference in PET signal when examining the transition time from pre-cavitation to cavitation. We measured no significant difference in [^{18}F]-FDG uptake when in either CT ROI or PET ROI was used **(Figure 2-4 C-D)**.

Changes in lung density during disease progression. Progression of active TB disease in the rabbit model leads to structural changes, such as fibrosis, that can be measured as an increase in lung tissue density **(Figure 2-3B)**. Changes in density can be measured by CT, and it was observed that the distribution of lung density changes over time **(Figure 2-5)**. A significant difference (*p* = 0.0038) was found when comparing the lung density distribution in cavitary progressive animals the week of cavitation versus the week prior to cavitation **(Figure 2-3B)**. A significant difference was also observed when measuring the density distribution at the week of cavitation compared to the week prior to cavitation using the PET ROI (two-tailed unpaired t-test) **(Figure 2-3C, Figure 2-6)**. The density distribution of cavitary progressing animals did show an increasing trend in the 0:100 HU domain in the CT ROI **(Figure 2-3D)**.

Defining an imaging marker of cavitation. We observed that the shifts in the density distribution from the PET ROI produced a peak in the −200:200 HU region **(Figure 2-7)**. It was also observed that a significant increase (p = 0.0003), in lung density in range of −200:200 HU occurs after infection **(Figure 2-8A)**. There was a significant difference (p = 0.0001) between cavitary progressing and non-cavitary progressing animals when measuring the percentage of lung within the −200:200 HU range **(Figure 2-8B)**.

To better refine the HU range that was enriched in cavitary progressing animals, we calculated the sum of differences between day 14 cavitary progressing animals (4) and non-cavitary progressing animals (7) **(Figure 2-6A)**. *Equation 1* calculates the difference of sums for a particular cavitary progressing animal defined as y_j and non-cavity progressing animals defined as x_i . The difference of sums can then be plotted as shown in **Figure 2-6A**. The domain of the curve (x-values) that corresponds to the range of $y > 0$ represents the HU that are enriched in the cavitary progressive animals. Alternatively, the domain of the curve that corresponds to the range of $y < 0$ represents the HU units that are underrepresented in the cavitary progressive animals. The individual curves generated by *Equation 1* can be summarized by calculating the sum of sums which is represented by *Equation 2* **(Figure 2-6B)**. The domain of 3.3-69.34 HU was identified from **Figure 2-6B** as being enriched in cavitary disease. We next checked if the area under the curve (AUC) for this domain was similarly different when measuring the density distribution in either the PET ROI or the CT ROI. We found that the density distribution was significantly different for both ROIs ($p < 0.0001$) **(Figure 2-9 A-B)**.

Assessment of the predictive power of the imaging markers using the test set. We developed two methods for predicting cavitary lesion progression using the data we collected from the training set series of animals. The methods quantify the density distribution as measured by CT using differently defined ROIs. The cutoffs of AUC > 90 and AUC > 115, for the PET and CT ROIs respectively, were positive predictors for the development of cavitary disease. These criteria were designed to provide the best combination of both sensitivity and specificity. Scans defined as positive were the week of cavitation and the week prior to cavitation. Therefore the training set consisted of 10 positive imaging sets, and 47 negative imaging sets **(Table 2-1, Figure 2-9C)**.

To validate the utility of these methods, these predictive criteria were applied to a new test set of rabbits. The test set was subjected to the same infection conditions as the training set group. Three out of four animals developed cavitary disease from the test set. The test set were imaged at pre-infection, 1, 2, 3, and 5 weeks post-infection and consisted of 6 positive scans and 13 negative scans (the week 5 scan from one rabbit was not used because it represented 2 weeks after cavitation occurred in this animal). Use of the PET ROI predicted cavitary disease with 100% sensitivity and 76% specificity and use of the CT ROI predicted cavitary disease with 83.3% sensitivity and 76.9% specificity **(Table 2-1, Figure 2-9C)**. Cavitary lesions that were identified by PET/CT imaging were consistent with histopathology findings as well **(Figure 2-10)**. Cavitary disease was reliably predicted up to 1 week in advance of cavitation.

Discussion

Tuberculosis biomarkers for monitoring disease outcome are urgently needed. The use of imaging biomarkers could have an immediate impact in a clinical trial setting in which resources are more abundant. At present, the cost of clinical trials for new TB vaccines and drugs is staggering because of poor biomarkers. Identification of robust biomarkers to monitor treatment outcome could dramatically reduce both the financial cost and study duration needed to evaluate new therapeutics [17, 18, 27].

Also, while it is true that TB is a disease that mainly affects the poor and underserved populations, the use of computational radiology techniques are not out of reach. For example the financial costs of providing radiology services are cheaper in India compared to the US [28]. There are current efforts to expand radiology services to underserved populations for public health reasons [29]. Treatment and clinical care of TB could be aided by improved imaging capabilities. While we show that the PET ROI provides the best sensitivity, the CT ROI does provide respectable prediction power. This is important because the resources for CT imaging are more widely available than the resources for PET imaging.

The improved sensitivity of predicting cavitary disease for the PET ROI compared to the CT ROI is likely due to a positive correlation between [^{18}F]-FDG uptake and inflammation. Inflammation results in the release of enzymes capable of remodeling the extracellular matrix. The role of proteases and collagenases and their necessity for producing the disease pathology typically observed in TB has previously been reported [4, 11, 12].

It is important to note that increasing uptake of [^{18}F]-FDG was observed during disease progression, consistent with recent studies [24-26, 30-32]. These studies established that [^{18}F]-FDG uptake is correlated with CFU burden. While it has been reported that cavities provide an environment for high bacterial burden, it is unknown if a high bacterial burden is a necessary prerequisite for cavitary formation [20, 33, 34]. It is plausible that the CFU burden prior to cavitation was similar between cavitary and non-cavitary groups and therefore there was a similar uptake of [^{18}F]-FDG. The density region that we observed to be increased during the course of disease progression was also independently reported in a marmoset model recently published by Via *et al* [31]. This suggests that the density region that we identified in this study may have more broad application outside of the rabbit model.

Currently our algorithms are able to predict cavitary disease up to 1 week in advance of cavitation. However we believe it may still be possible to improve the predictive power beyond 1 week by incorporating additional non-radiological tests that were not included in the present study. Tests such as sputum smear microscopy, Interferon-Gamma Release Assays (IGRAs), quantification of lung matrix and break down products, and other non-invasive tests could be considered.

References

1. Global Tuberculosis Report 2012 (2012). Global Tuberculosis Report 2012.

2. Garnier, T., Eiglmeier, K., Camus, J.-C., Medina, N., Mansoor, H., Pryor, M., Duthoy, S., Grondin, S., Lacroix, C., Monsempe, C., et al. (2003). The complete genome sequence of Mycobacterium bovis. Proc Natl Acad Sci USA *100*, 7877–7882.

3. Perrin, F. M. R., Woodward, N., Phillips, P. P. J., McHugh, T. D., Nunn, A. J., Lipman, M. C. I., and Gillespie, S. H. (2010). Radiological cavitation, sputum mycobacterial load and treatment response in pulmonary tuberculosis. Int J Tuberc Lung Dis *14*, 1596–1602.

4. Dannenberg, A. M. (2009). Liquefaction and cavity formation in pulmonary TB: a simple method in rabbit skin to test inhibitors. Tuberculosis (Edinb) *89*, 243–247.

5. Nam, K. J., Jeong, Y. J., Kim, Y. D., Kim, K.-L., Lee, J. W., Park, H. K., and Hoseok, I. (2012). Chronic destructive pulmonary tuberculosis: assessment of disease activity by computed tomography. Acta Radiol.

6. Matsuoka, S., Uchiyama, K., Shima, H., Suzuki, K., Shimura, A., Sasaki, Y., and Yamagishi, F. (2004). Relationship between CT findings of pulmonary tuberculosis and the number of acid-fast bacilli on sputum smears. Clin Imaging *28*, 119–123.

7. Yoder, M. A., Lamichhane, G., and Bishai, W. R. (2004). Cavitary pulmonary tuberculosis: the Holy Grail of disease transmission. CURRENT SCIENCE-BANGALORE- *86*, 74–81.

8. Erkens, C. G. M., Kamphorst, M., Abubakar, I., Bothamley, G. H., Chemtob, D., Haas, W., Migliori, G. B., Rieder, H. L., Zellweger, J.-P., and Lange, C. (2010). Tuberculosis contact investigation in low prevalence countries: a European consensus. Eur Respir J *36*, 925–949.

9. Benator, D., Bhattacharya, M., Bozeman, L., Burman, W., Cantazaro, A., Chaisson, R., Gordin, F., Horsburgh, C. R., Horton, J., Khan, A., et al. (2002). Rifapentine and isoniazid once a week versus rifampicin and isoniazid twice a week for treatment of drug-susceptible pulmonary tuberculosis in HIV-negative patients: a randomised clinical trial. Lancet *360*, 528–534.

10. Hunter, R. L. (2011). Pathology of post primary tuberculosis of the lung: An illustrated critical review. Tuberculosis (Edinb).

11. Elkington, P. T., D'Armiento, J. M., and Friedland, J. S. (2011). Tuberculosis immunopathology: the neglected role of extracellular matrix

destruction. Science Translational Medicine *3*, 71ps6–71ps6.

12. Elkington, P., Shiomi, T., Breen, R., Nuttall, R. K., Ugarte-Gil, C. A., Walker, N. F., Saraiva, L., Pedersen, B., Mauri, F., Lipman, M., et al. (2011). MMP-1 drives immunopathology in human tuberculosis and transgenic mice. J. Clin. Invest. *121*, 1827–1833.

13. Blumberg, H. M., Burman, W. J., Chaisson, R. E., Daley, C. L., Etkind, S. C., Friedman, L. N., Fujiwara, P., Grzemska, M., Hopewell, P. C., Iseman, M. D., et al. (2003). American Thoracic Society/Centers for Disease Control and Prevention/Infectious Diseases Society of America: treatment of tuberculosis. Am J Respir Crit Care Med *167*, 603–662.

14. Coninx, R., Mathieu, C., Debacker, M., Mirzoev, F., Ismaelov, A., de Haller, R., and Meddings, D. R. (1999). First-line tuberculosis therapy and drug-resistant Mycobacterium tuberculosis in prisons. Lancet *353*, 969–973.

15. Pomerantz, B. J., Cleveland, J. C., Olson, H. K., and Pomerantz, M. (2001). Pulmonary resection for multi-drug resistant tuberculosis. J. Thorac. Cardiovasc. Surg. *121*, 448–453.

16. Doherty, M., Wallis, R. S., Zumla, A., WHO-Tropical Disease Research/European Commission joint expert consultation group (2009). Biomarkers for tuberculosis disease status and diagnosis. Curr Opin Pulm Med *15*, 181–187.

17. Wallis, R. S., Pai, M., Menzies, D., Doherty, T. M., Walzl, G., Perkins, M. D., and Zumla, A. (2010). Biomarkers and diagnostics for tuberculosis: progress, needs, and translation into practice. Lancet *375*, 1920–1937.

18. Wallis, R. S., Kim, P., Cole, S., Hanna, D., Andrade, B. B., Maeurer, M., Schito, M., and Zumla, A. (2013). Tuberculosis biomarkers discovery: developments, needs, and challenges. Lancet Infect Dis *13*, 362–372.

19. McNerney, R., Maeurer, M., Abubakar, I., Marais, B., McHugh, T. D., Ford, N., Weyer, K., Lawn, S., Grobusch, M. P., Memish, Z., et al. (2012). Tuberculosis diagnostics and biomarkers: needs, challenges, recent advances, and opportunities. J Infect Dis *205 Suppl 2*, S147–58.

20. Nedeltchev, G. G., Raghunand, T. R., Jassal, M. S., Lun, S., Cheng, Q.-J., and Bishai, W. R. (2009). Extrapulmonary dissemination of Mycobacterium bovis but not Mycobacterium tuberculosis in a bronchoscopic rabbit model of cavitary tuberculosis. *77*, 598–603.

21. Bagci, U., Yao, J., Miller-Jaster, K., Chen, X., and Mollura, D. J. (2013). Predicting Future Morphological Changes of Lesions from Radiotracer Uptake in 18F-FDG-PET Images. PLoS ONE *8*, e57105.

22. Foster, B., Bagci, U., Luna, B., Dey, B., Bishai, W. R., Jain, S., Xu, Z., and Mollura, D. J. (2013). Robust segmentation and accurate target definition for positron emission tomography images using Affinity Propagation. 2013 IEEE 10th International Symposium on Biomedical Imaging, 1461–1464.

23. Bagci, U., Udupa, J. K., Yao, J., and Mollura, D. J. (2012). Co-segmentation of functional and anatomical images. Med Image Comput Comput Assist Interv *15*, 459–467.

24. Via, L. E., Schimel, D., Weiner, D. M., Dartois, V., Dayao, E., Cai, Y., Yoon, Y.-S., Dreher, M. R., Kastenmayer, R. J., Laymon, C. M., et al. (2012). Infection Dynamics and the Response to Chemotherapy in a Rabbit Model of Tuberculosis using [18F]-2-Fluoro-deoxy-D-glucose Positron Emission Tomography -- Computed Tomography. Antimicrob Agents Chemother.

25. Davis, S. L., Nuermberger, E. L., Um, P. K., Vidal, C., Jedynak, B., Pomper, M. G., Bishai, W. R., and Jain, S. K. (2009). Noninvasive pulmonary [18F]-2-fluoro-deoxy-D-glucose positron emission tomography correlates with bactericidal activity of tuberculosis drug treatment. Antimicrob Agents Chemother *53*, 4879–4884.

26. Soussan, M., Brillet, P.-Y., Mekinian, A., Khafagy, A., Nicolas, P., Vessieres, A., and Brauner, M. (2012). Patterns of pulmonary tuberculosis on FDG-PET/CT. Eur J Radiol *81*, 2872–2876.

27. Koul, A., Arnoult, E., Lounis, N., Guillemont, J., and Andries, K. (2011). The challenge of new drug discovery for tuberculosis. Nature *469*, 483–490.

28. Yu, K. H., and Levy, F. (2010). Offshoring professional services: institutions and professional control. British Journal of Industrial Relations *48*, 758–783.

29. Mollura, D. J., Carrino, J. A., Matuszak, D. L., Mnatsakanyan, Z. R., Eng, J., Cutchis, P., Babin, S. M., Sniegoski, C., and Lombardo, J. S. (2008). Bridging radiology and public health: the emerging field of radiologic public health informatics. J Am Coll Radiol *5*, 174–181.

30. Lin, P. L., Coleman, T., Carney, J. P. J., Lopresti, B. J., Tomko, J., Fillmore, D., Dartois, V., Scanga, C., Frye, L. J., Janssen, C., et al. (2013). Radiologic responses in cynomolgous macaques for assessing tuberculosis chemotherapy regimens. Antimicrob Agents Chemother.

31. Via, L. E., Weiner, D. M., Schimel, D., Lin, P. L., Dayao, E., Tankersley, S. L., Cai, Y., Coleman, M. T., Tomko, J., Paripati, P., et al. (2013). Differential Virulence and Disease Progression Following Mycobacterium tuberculosis Complex Infection of the Common Marmoset (Callithrix jacchus). Infect Immun.

32. Russell, D. G., Barry, C. E., and Flynn, J. L. (2010). Tuberculosis: what we don't know can, and does, hurt us. Science *328*, 852–856.

33. Dannenberg, A. M. (2006). Pathogenesis of Human Pulmonary Tuberculosis: Insights from the Rabbit Model. ASM Press.

34. Subbian, S., Tsenova, L., Yang, G., O'Brien, P., Parsons, S., Peixoto, B., Taylor, L., Fallows, D., and Kaplan, G. (2011). Chronic pulmonary cavitary tuberculosis in rabbits: a failed host immune response. Open Biol *1*, 110016.

Figures

Figure 2-1: Algorithms for predicting cavitary disease.

The algorithms outline the steps involved in both the processing and analysis of image data sets. The basic steps involved are to co-register PET and CT data sets, segment the lung region, define a ROI, apply the ROI to the CT data set, and to calculate the AUC to evaluate if the animal is expected to develop cavitary disease. A) Algorithm which applies a PET ROI to the CT data set. B) Algorithm which applies a CT ROI to the CT data set.

A

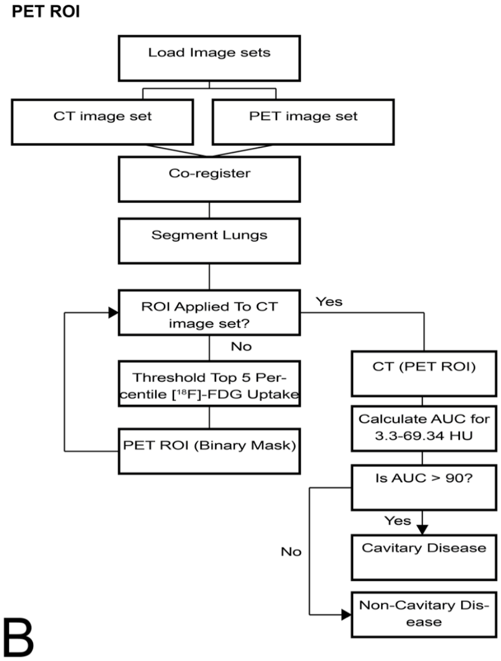
PET ROI
Load Image sets
CT image set
PET image set
Co-register
Segment Lungs
ROI Applied To CT image set?
Yes
No
Threshold Top 5 Percentile [18F]-FDG Uptake
PET ROI (Binary Mask)
CT (PET ROI)
Calculate AUC for 3.3-69.34 HU
Is AUC > 90?
Yes
No
Cavitary Disease
Non-Cavitary Disease

B

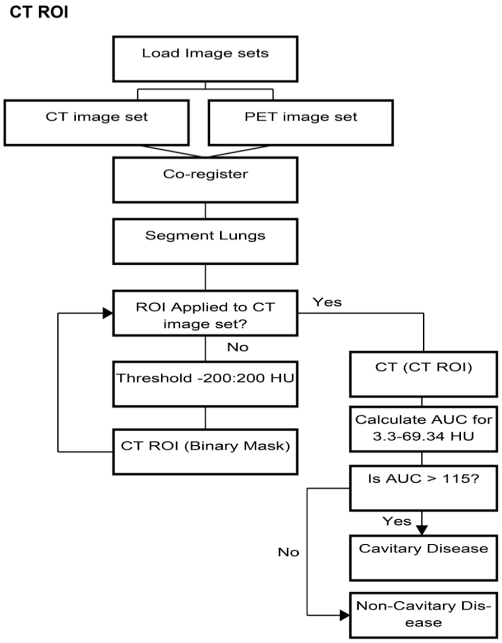
CT ROI
Load Image sets
CT image set
PET image set
Co-register
Segment Lungs
ROI Applied to CT image set?
Yes
No
Threshold -200:200 HU
CT ROI (Binary Mask)
CT (CT ROI)
Calculate AUC for 3.3-69.34 HU
Is AUC > 115?
Yes
No
Cavitary Disease
Non-Cavitary Disease

Figure 2-2: Image segmentation and registration.

A) Outline of the process of image coregistration and segmentation. a) CT coregistered image. b) PET coregistered image. c) CT/PET coregistered image fusion. d) Binary mask generated from segmentation of the lung by CT. e) Product of image “B” x “D”. f) Product of image “A” x “D”. g) A representative 3D reconstruction of the PET and CT segmented image data. B) Image shows the visual representations of the PET ROI and CT ROI. The upper panels of represent the region of the lung included in the CT ROI and the bottom panels represent the region of the lung included by the PET ROI.

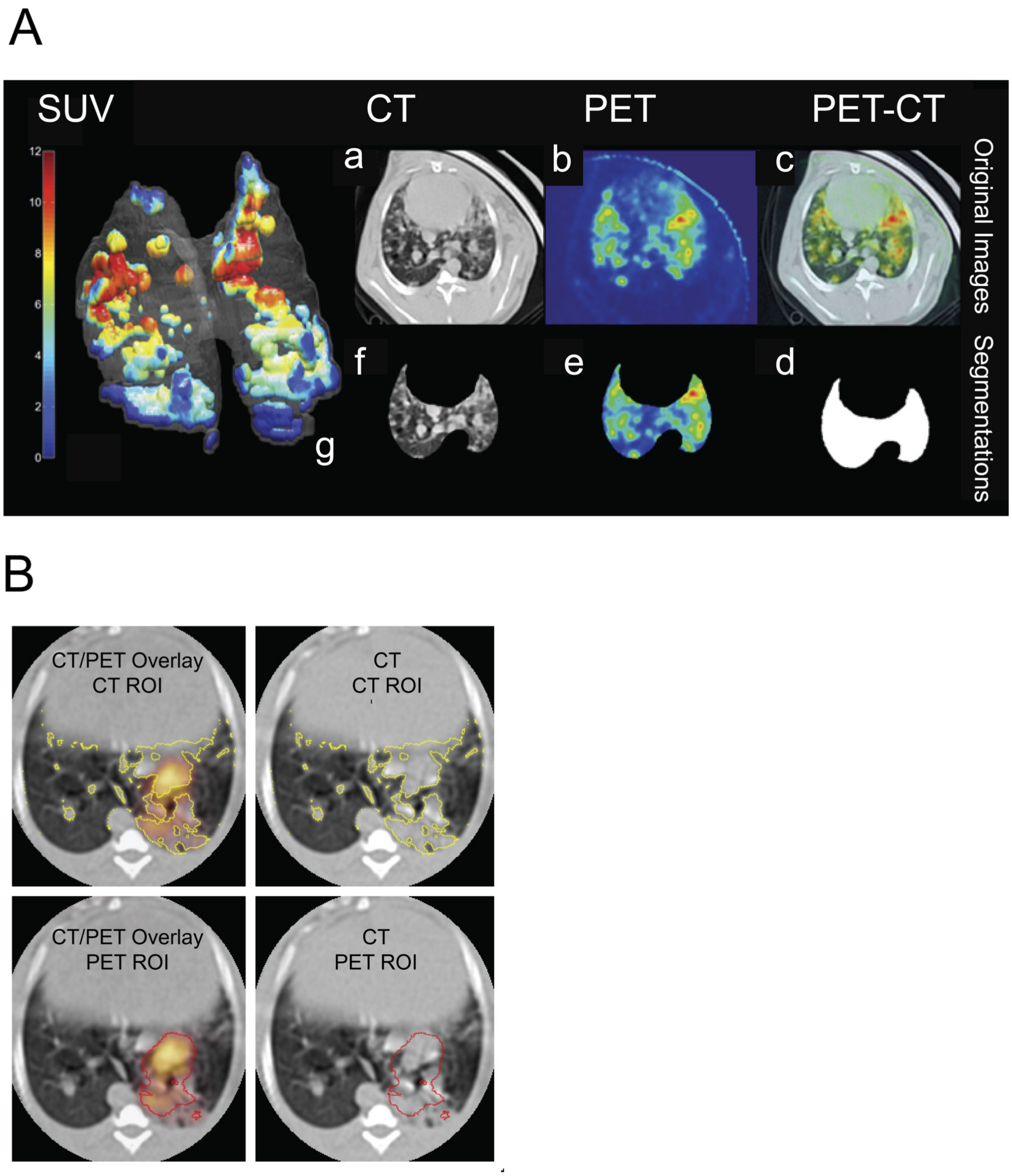
A
SUV
CT
PET
PET-CT
12
10
8
6
4
2
0
a
b
c
Original Images
f
e
d
Segmentations
g
B
CT/PET Overlay
CT ROI
CT
CT ROI
CT/PET Overlay
PET ROI
CT
PET ROI

Figure 2-3: Density change in cavitary progressing and non-cavitary progressing groups.

PET and CT image sets were first coregistered and the lung field was defined by CT. A binary mask of the CT defined lung field was then multiplied against the PET image stack to define the lung field in the PET image stack. Subsequent ROIs were defined by either CT or PET as described below. A) A general representation of the densities associated with different disease pathologies observed by CT. “A” represents a cavity, “B” represents normal lung, and “C” represents a region of consolidation. B) Density as measured from the segmented, total lung reconstruction. A significant difference was observed between the two groups (p = 0.0038) C) Density distribution within the CT ROI. The cavitary progressing group showed increased density in the 0:100 HU domain. D) Density distribution within the PET ROI. A significant difference was observed between the groups (p = 0.038).

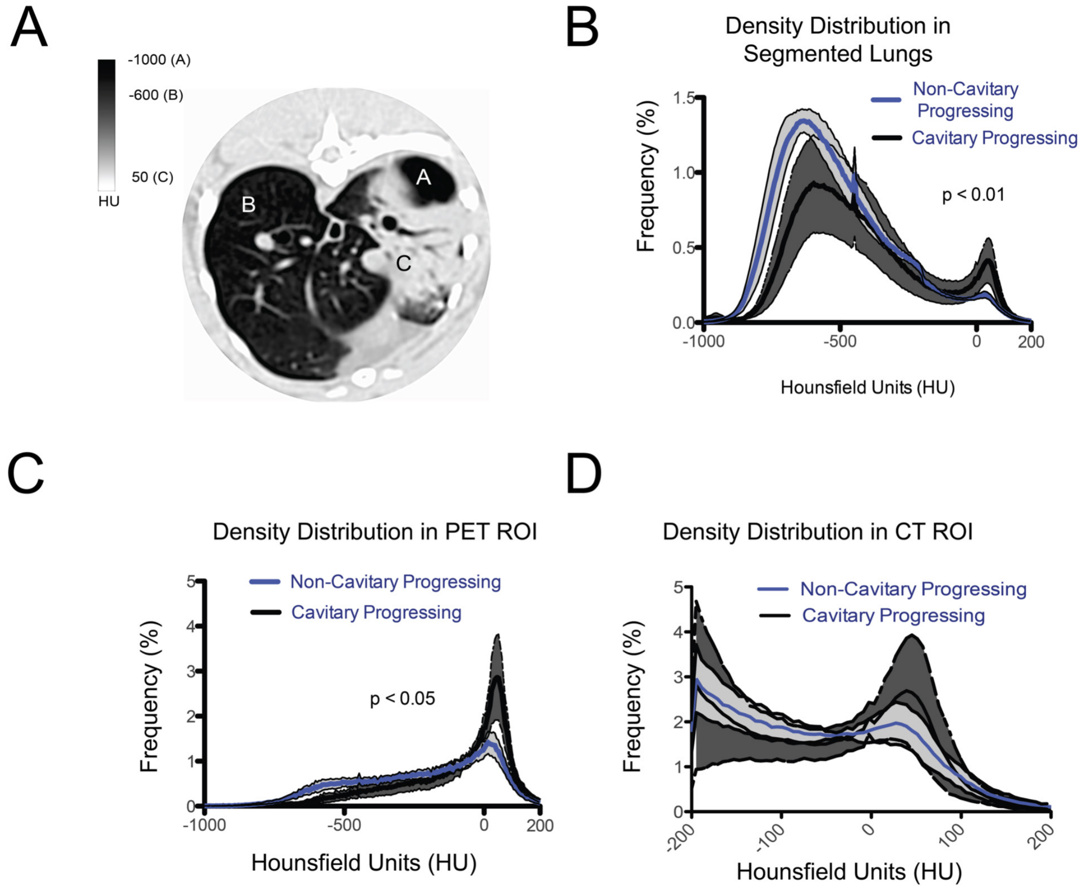
A
-1000 (A)
-600 (B)
50 (C)
HU
A
B
C
B
Density Distribution in Segmented Lungs
Non-Cavitary Progressing
Cavitary Progressing
p < 0.01
Frequency (%)
1.5
1.0
0.5
0.0
-1000
-500
0
200
Hounsfield Units (HU)
C
Density Distribution in PET ROI
Non-Cavitary Progressing
Cavitary Progressing
p < 0.05
Frequency (%)
5
4
3
2
1
0
-1000
-500
0
200
Hounsfield Units (HU)
D
Density Distribution in CT ROI
Non-Cavitary Progressing
Cavitary Progressing
Frequency (%)
5
4
3
2
1
0
-200
-100
0
100
200
Hounsfield Units (HU)

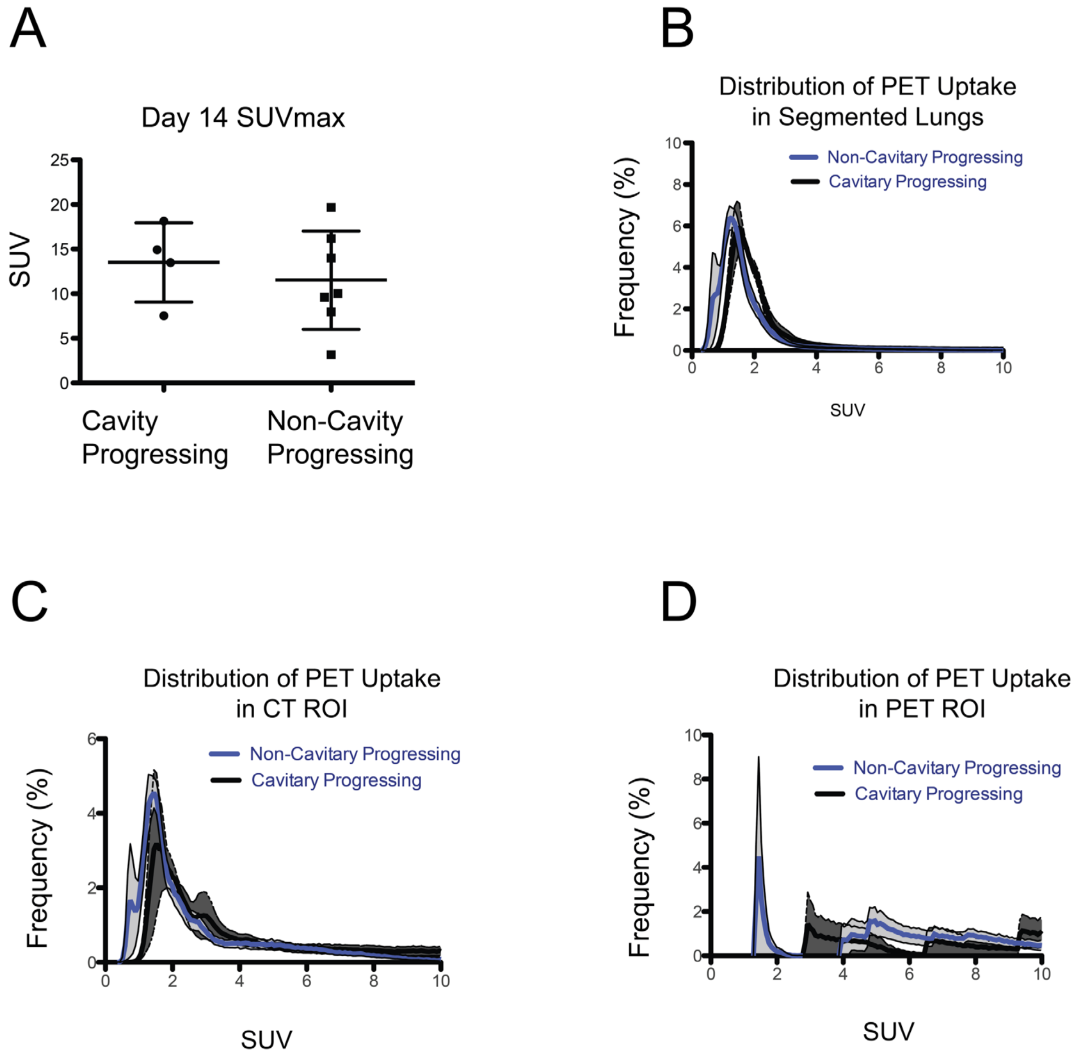

Figure 2-4: Change in [^{18}F]-FDG SUVmax between cavitary progressing and non-cavitary progressing groups over time.

A) There is no difference in [^{18}F]-FDG SUVmax between cavitary-progressing and non-cavitary progressing disease D14. B) [^{18}F]-FDG uptake as measured from the segmented, total lung image, showing no significant difference. C) PET uptake in the CT ROI. No significant difference was observed between groups. D) PET uptake in the PET ROI. No significant difference was observed.

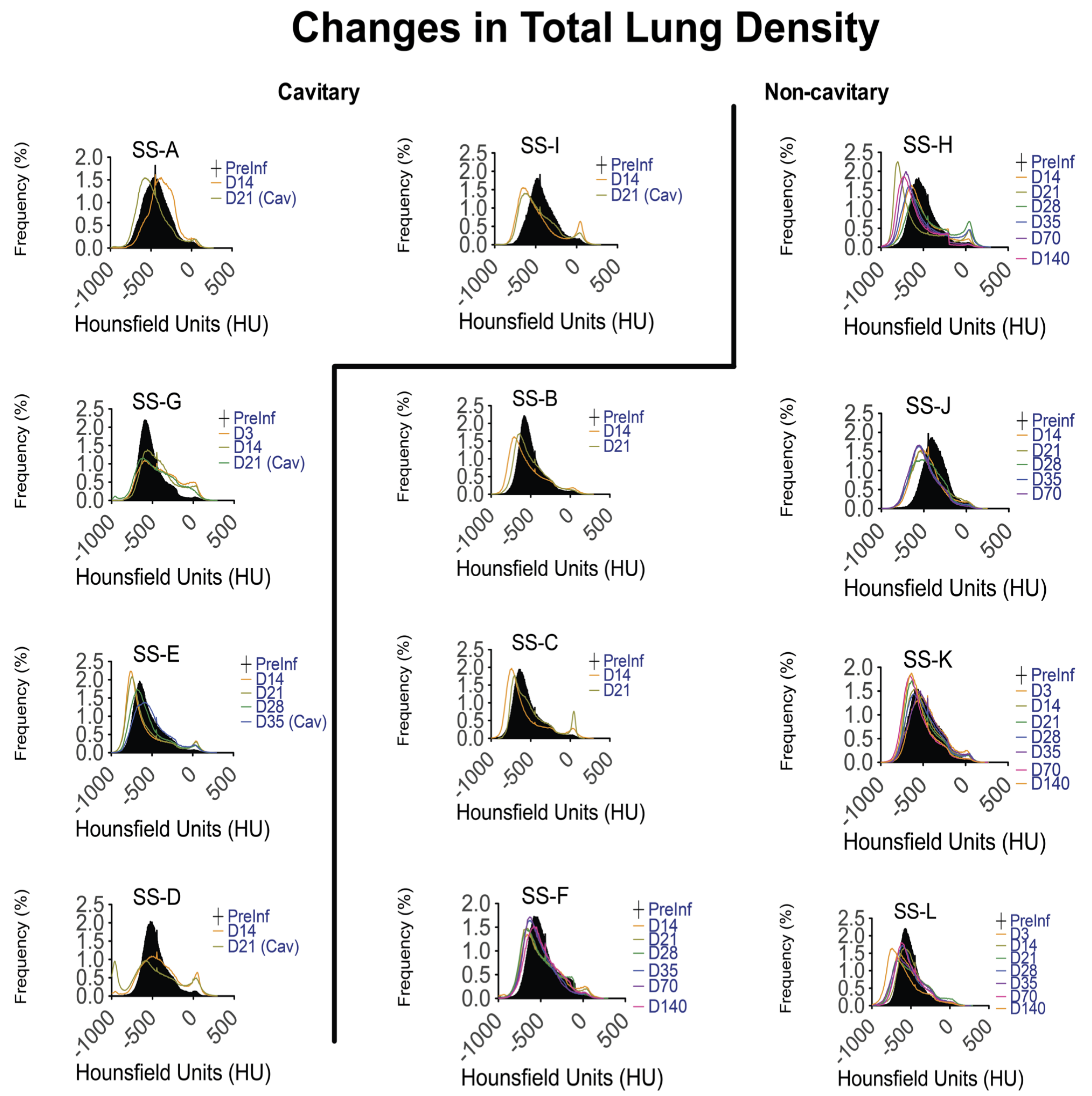

Fig. 2-5: Change in total lung density over time.

Lung regions were manually segmented prior to analysis. The graphs represent the change in lung density (HU units) as measured by CT. Appearance of cavity by CT is denoted as “Cav”. The black, filled in histogram is the pre-infection baseline. A peak in the 0:100 HU range can be observed in cavitary progressing animals.

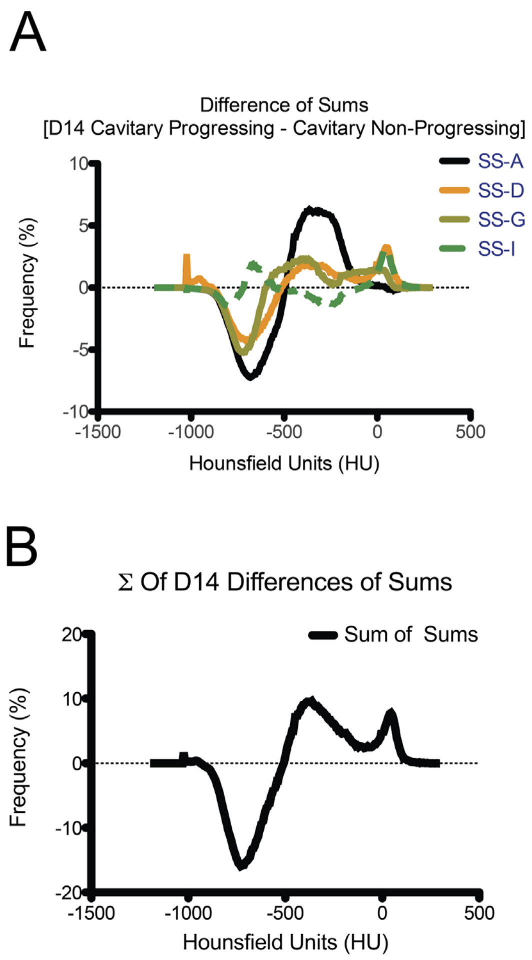

Fig. 2-6: The sum of differences and sum of sums.

The domain of the curve (x-values) that corresponds to the range of $y > 0$ represents the HU that are enriched in the cavitary progressive animals. Alternatively, the domain of the curve that corresponds to the range of $y < 0$ represents the HU units that are underrepresented in the cavitary progressive animals. A) The sum of differences as calculated by *Equation 1* for individual cavitary progressing animal. B) The sum of differences as calculated by *Equation 2*.

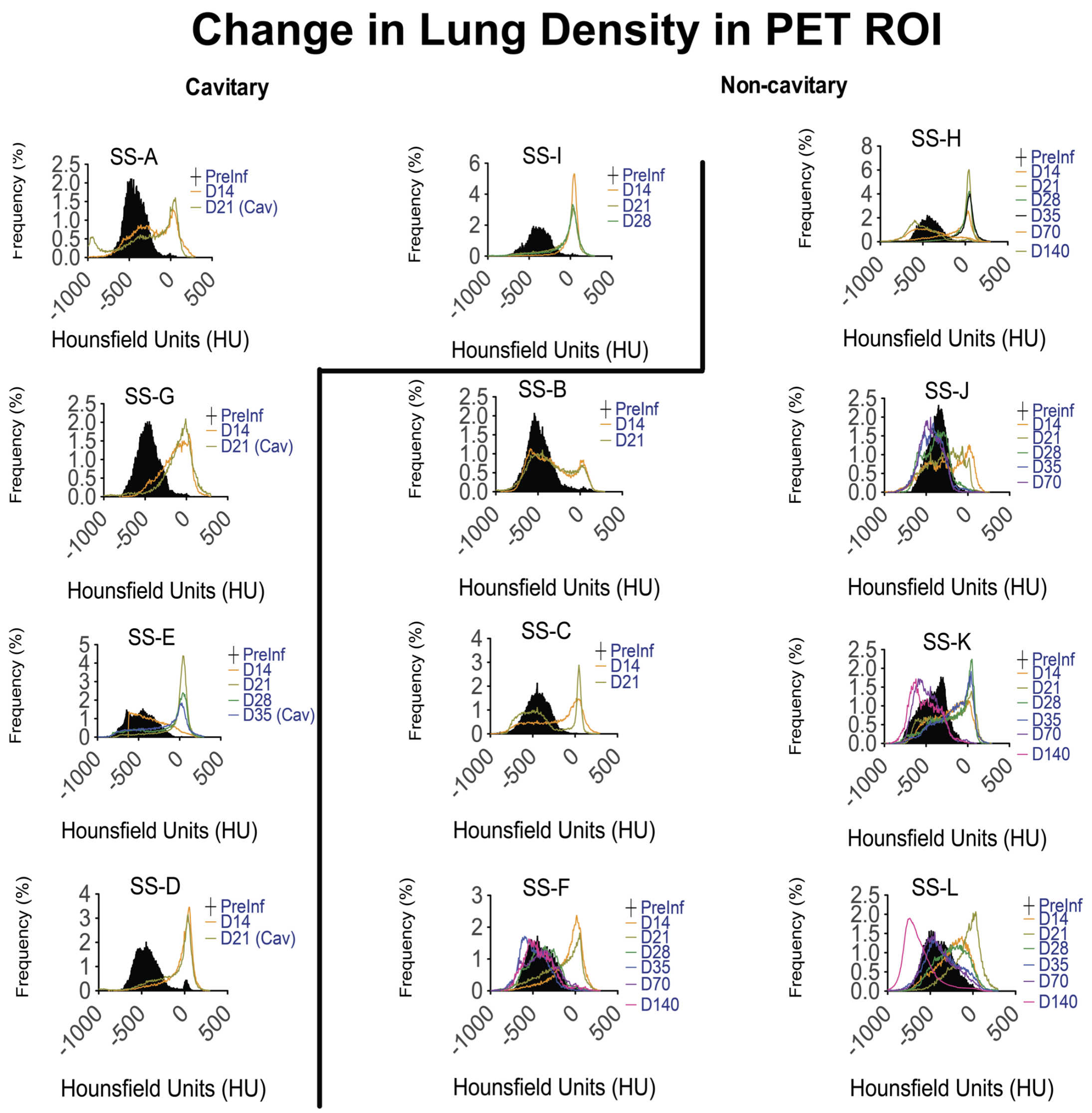

Figure 2-7: Change in lung density in PET ROI.

Lung regions were manually segmented and the ROIs were defined by uptake of [^{18}F]-FDG tracer. The graphs represent the change in lung density (HU units) as measured by CT. Appearance of cavity by CT is denoted as “(Cav)”.

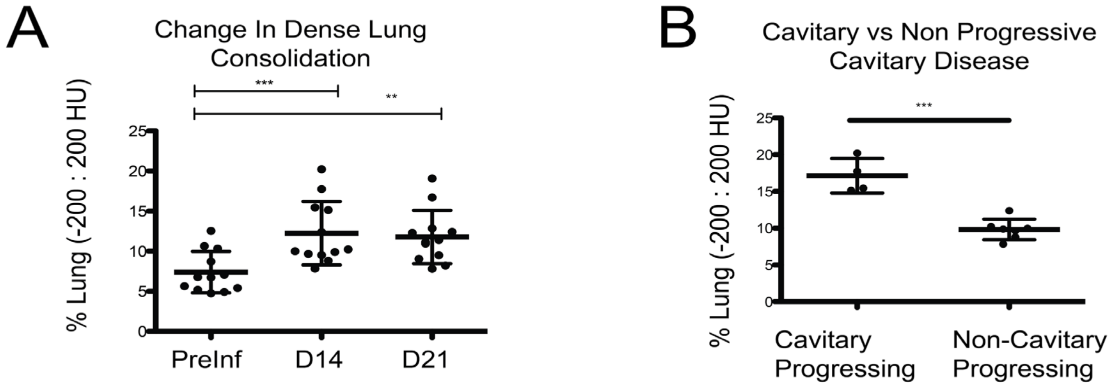

Figure 2-8: Change in the proportion of densely consolidated lung tissue.

Total lung regions were defined by manual segmentation. Densely consolidated tissue was defined by the range −200:200 HU. A) The change of densely consolidated tissue over time. B) The change of densely consolidated tissue by disease state. There is a significant difference in the amount of lung consolidation present in cavitary progressing and non-cavitary progressing rabbits at day 14.

Figure 2-9: AUC test for predicting cavitary progression.

The AUC corresponding to the range defined by 3.3-69.34 HU was found to be significant ($p < 0.0001$, two-tailed unpaired t-test) for A) CT ROI and B) PET ROI. C) ROC curves which use either PET or CT defined ROIs. All curves perform similarly. Each step in the curve corresponds to an increasing cutoff value of the AUC which would be defined as positive. As the curves progress to the right of the graph there is a decrease in sensitivity but an increase in specificity.

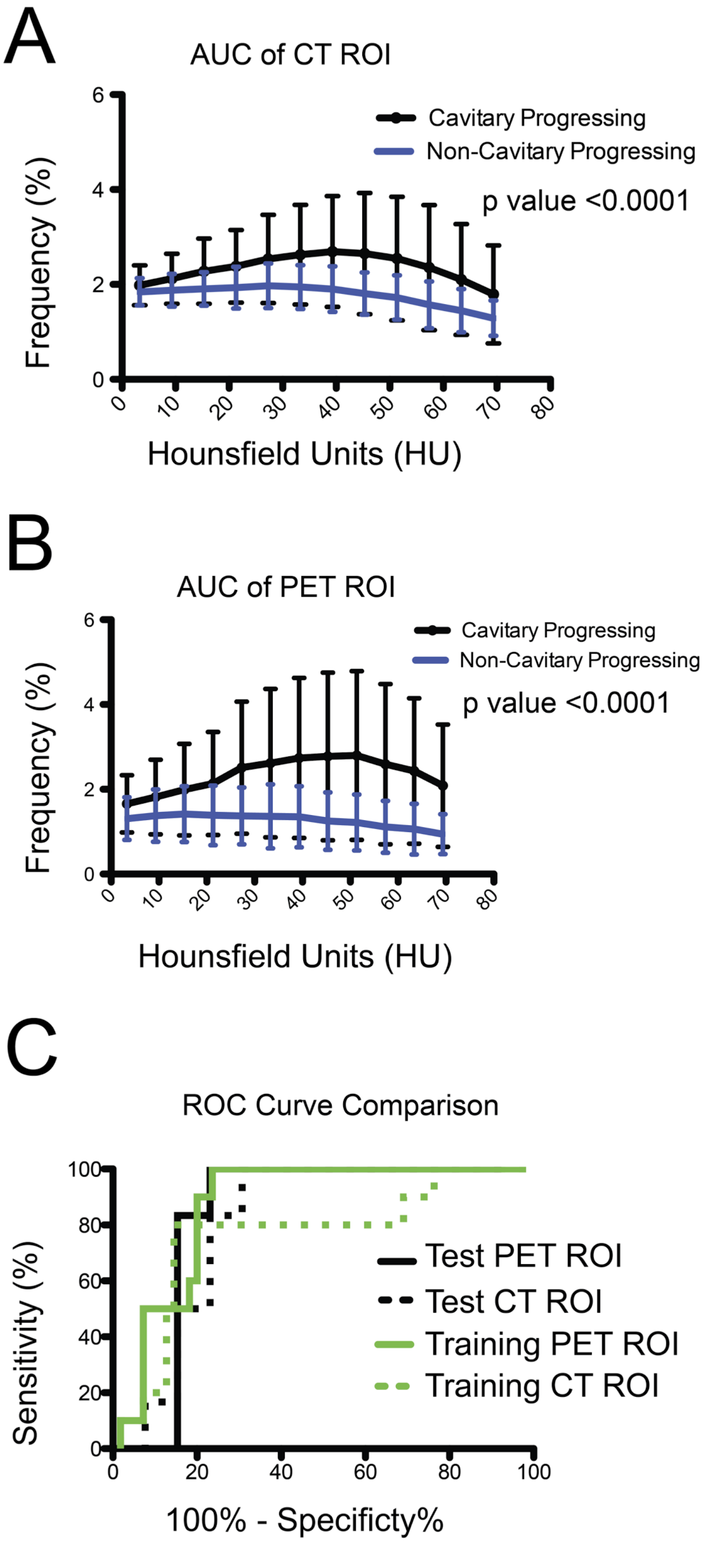
A
AUC of CT ROI
Frequency (%)
Hounsfield Units (HU)
Cavitary Progressing
Non-Cavitary Progressing
p value <0.0001
0
2
4
6
0
10
20
30
40
50
60
70
80
B
AUC of PET ROI
Frequency (%)
Hounsfield Units (HU)
Cavitary Progressing
Non-Cavitary Progressing
p value <0.0001
0
2
4
6
0
10
20
30
40
50
60
70
80
C
ROC Curve Comparison
Sensitivity (%)
100% - Specificty%
Test PET ROI
Test CT ROI
Training PET ROI
Training CT ROI
0
20
40
60
80
100
0
20
40
60
80
100

Figure 2-10: Rabbit cavity lesion.

A) A cavity lesion is shown by the crosshairs in a *M. tb* infected rabbit. The cavity is identifiable as a region of low density by CT and uptake of the PET tracer is localized to the cavity wall. Localization of PET tracer uptake to the cavity wall is expected since the cavity is air filled and void of any cells capable of taking up the tracer. B) Confirmation of a cavity lesion by histopathology. Tissue was stained by H&E stain. The inset shows a 10x magnified view.

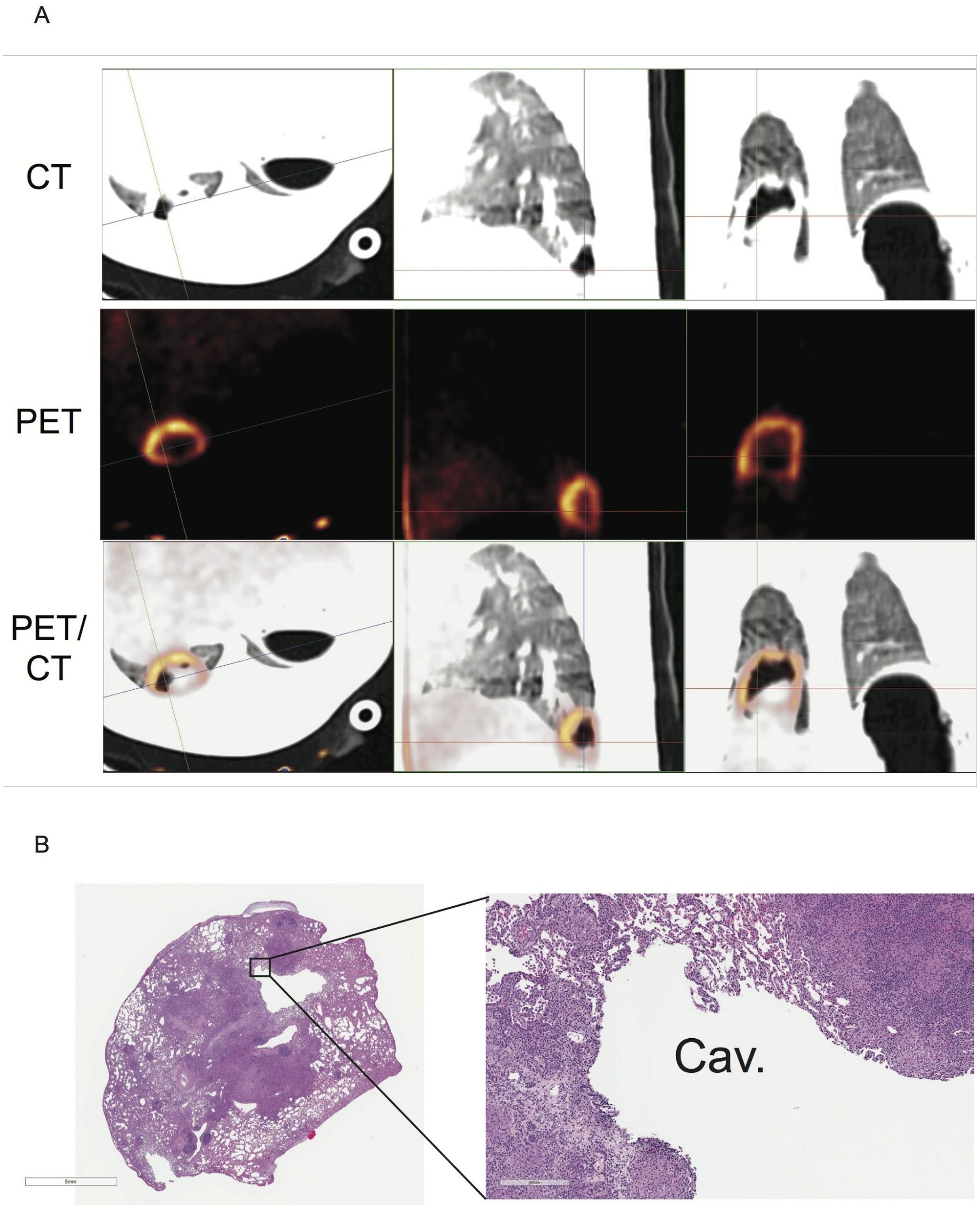
A
CT
PET
PET/
CT
B
5mm
Cav.

Equation 1

$$fy_j(x_i) = \sum_{i=1}^{7} y_j - x_i$$

Equation 2

$$f(y_j, x_i) = \sum_{j=1}^{4} \sum_{i=1}^{7} y_j - x_i$$

Table 2-1: Sensitivity and specificity of cavitary predictive radiology markers.

Use of the *Pet** ROI outperformed the *CT** ROI.

	Training Set. **10 True Positive.** **55 True negatives.**		**Test Set.** **6 True Positives.** **13 True negatives.**	
ROI	PET	CT	PET	CT
AUC	90	115	90	115
Sensitivity	90	80	100	83.333
Specificity	78.182	72.727	76.923	76.923

Table 2-2: Concept box

Terms	Definitions
Standardized Uptake Value (SUV)	Unit of normalized uptake of PET tracer. SUV = (pixel dose (mCi/CC) * body weight (kg))/ injected dose (mCi)
Region of Interest (ROI)	An arbitrary region of interest defined by the analyst
Hounsfield Units (HU)	Scale of density measured by CT. Air = -1000 HU, water = 0 HU, and bone = 1000 HU
Coregistration	The process of spatially transforming image “a”□ to align with image “b”
Segmentation	Dividing an image into defined parts

Chapter 3: RNA-seq of host expression profile in a rabbit model of cavitary tuberculosis

Abstract

Rationale: Cavitary disease is thought to form as the result of an unfavorable host immune response. The rabbit is capable of modeling cavitary tuberculosis disease, however the lack of commercial tools for studying the genetic and molecular host factors have made progress slow in studying the rabbit host response. **Objectives:** Microarrays have been the standard for assessing global expression changes, however these tools are currently unavailable for rabbits. Here we present a study in which we perform a RNA-seq analysis of the rabbit host response to cavitary disease. **Methods:** 3 Female New Zealand White rabbits were challenged with live virulent *M. tb* H37Rv strain and cavitary lesions were allowed to develop. 3 female New Zealand White rabbits were included in the study as uninfected controls. From the infected rabbit group, RNA was extracted from the cavity wall and from uninvolved tissue from the contralateral lung. RNA was also isolated from 3 non-infected control animals. Total RNA was extracted by the TRIZOL method and sequenced using the AB SOLiD deep sequencer. **Measurements and Main Results:** A total of 8737 transcripts were mapped and 3380 transcripts were unmapped. For pathway analysis using the Ingenuity Pathway Analysis software, we used a 3-fold (log2) cutoff and identified

194 differentially expressed genes. The uninvolved tissue clustered better with the naive tissue and the cavity wall was distinctly different from uninvolved and naive samples. *mmp-1* was among the most upregulated genes in the cavity wall compared to naive or uninvolved tissue. Cell recruitment, wound healing, and microbial response pathways were all significantly upregulated. **Conclusions:** Because CFUs were culturable from the uninvolved lung, the expression changes observed were not simply due to the presence or absence of bacteria. The data is consistent with the hypothesis that cavitary lesions are driven by the host immune response.

Introduction

Tuberculosis is one of the major causes of morbidity and mortality due to a single bacterial pathogen [1]. Development of cavitary lesions have negative implications for both drug treatment efficacy and disease transmission [2]. It is believed that the breakdown of the lung extracellular matrix is necessary for the development of cavitary lesions and that matrix remodeling is a host driven process [3-5]. Granulomas and cavitary lesions are pathological hallmarks of human tuberculosis disease. BALB/c and C57BL/6 mice, the most common mice strains used historically for tuberculosis research, do not develop granulomas and cavitary lesions. Rabbits and non-human primates do develop granulomas and cavitary lesions, additionally the disease pathology developed by these animal models looks similar to tuberculosis pathology in humans [6-11].

Despite the abundance of genetic and molecular tools available for the mouse which make the mouse an attractive model system, the mouse does not faithfully recapitulate cavitary disease and is therefore not the appropriate system to study cavitary lesion development. Rabbits are the most accessible laboratory animal that reliably develops cavitary disease, and the majority of research concerning cavitary disease has been done in the rabbit model [11].

One of the limitations regarding the rabbit model is the relative lack of genetic and molecular tools compared to those available for other model organisms.

However the availability of the sequenced rabbit genome allows for the use of PCR based assays such as RNA sequencing. RNA sequencing provides a platform for whole genome expression analysis with unbiased results [12, 13].

Prior to RNA sequencing, microarrays have been the primary platform for global gene expression studies. The basic principle behind microarrays is that labeled samples are washed over a slide that contains unlabeled probes specific to targets of interest. The relative abundance is determined by the signal intensity from binding of labeled samples and mapping of the probe provides information about the identity of the hybridized sample. While microarrays have proven to be extremely valuable research tools, there remains one major technical hurdle inherent to microarray assays. Microarrays can only provide information for targets in which probes have been printed. This means that there needs to be some knowledge of the potential targets before the microarray is designed [14]. The result is that microarrays are of limited utility for the identification of novel events such as novel splice variants or unannotated transcripts.

One important benefit of RNA sequencing as compared to microarrays is that that RNA sequencing does not require prior knowledge of the expected transcripts and is therefore not constrained by the need to design probes to the prospective targets of interest [13]. RNA sequencing provides a more robust and unbiased platform for measuring whole genome expression compared to microarray assays.

In this study we use RNA sequencing as a way of interrogating the host response to cavitary disease. We then did a pathway analysis to determine which biologically relevant pathways were differentially expressed using a commercially available software, Ingenuity Pathway Analysis (IPA). Next we confirmed our pathway analysis by using the Gene Set Enrichment Analysis (GSEA) software package [15, 16]. Lastly, we used a third analysis package, the Tuxedo Suite, for identifying unannotated transcripts [17].

Materials and Methods

Ethics Statement

All animal experiments were carried out in strict accordance with the recommendations in the “Guide for the Care and Use of Laboratory Animals of the National Institutes of Health” and all procedures were approved by the Johns Hopkins University Animal Care and Use Committee.

Rabbit Sensitization and infection

Rabbits were presensitized and infected as described previously [18]. Briefly, rabbits were administered a series of 5 subcutaneous injections of a 1:1 suspension of Freund's incomplete adjuvant mixed with 1 x 10^8 heat killed bacilli. The injections were spread out over 2.5 weeks and the rabbits were subsequently allowed to rest for 2.5 weeks. Rabbits were administered a PPD test to confirm sensitization. Prior to infection rabbits were anaesthetized with a combination of ketamine (17-35 mg/kg), xylazine (5-10 mg/kg), and acepromazine (0.75 mg/kg). Rabbits were infected by depositing a bacterial suspension containing 10^4 colony forming units (CFU) of live, virulent *M. tb* H37Rv strain in the right lower lobe of the lung by bronchoscopy. The CFU of the infectious suspension was determined by serial dilution and plating on 7H11 agar plates.

Necropsy

Rabbits were anaesthetized with ketamine (17-35 mg/kg), xylazine (5-10 mg/kg), and acepromazine (0.75 mg/kg) and then euthanized with 3 ml of Euthasol Euthanasia Solution (Virbac Animal Health, Fort Worth, Texas). Following euthanasia, rabbits were necropsied and the lungs were harvested. Lung tissue from cavitary animals were separated by gross pathology into cavity wall, granulomatous, and uninvolved groups. Tissue for RNA extractions were stored immediately in RNA*later* (Ambion).

RNA extraction

Lung samples were stored in RNA*later* (Ambion) per manufacturer’s protocol. Lung tissue was homogenized in TRIZOL (Invitrogen) using a bead beater and 2 mm glass beads. RNA was extracted by following the TRIZOL protocol. RNA was further purified using the RNeasy kit (Qiagen) following the manufacturer's protocol. RNA was eluted and cleaned, prior to Turbo DNAse treatment

(Ambion). Final RNA concentration was measured by Nanodrop (Nanodrop 2000C ThermoScientific, DE, USA), and adjusted to 0.5 µg/µl. The RNA is then converted to cDNA by the Agilent Superscript cDNA synthesis kit (Agilent, CA) according to the manufacturer's protocol. RNA integrity was determined with the Agilent 2100 Bioanalyzer (Agilent Technologies) and mRNA was enriched for using the RIBOMinus kit according to the manufacturer's protocol (Life Technologies). Depletion of rRNA was determined by the Agilent 2100 Bioanalyzer.

RNA-seq

The library preparation of rRNA depleted RNA was done using the Applied Biosystems SOLiD Total RNA-Seq kit (Applied Biosystems) according to the manufacturer's protocol. RNA was fragmented and purified using the Invitrogen RiboMinus Concentration Module (Life Technologies). The size distribution was determined by the Bioanalyzer using the RNA 6000 Pico Chip Kit (Agilent Technologies). RNA yield was quantified using the Qubit Fluorometer (Life Technologies). Library amplification was done using the Applied Biosystems SOLiD Total RNA-Seq kit and samples were barcoded with unique 3' primer. The quality of the library was assessed using the DNA1000 chip and the Agilent Bioanalyzer. Libraries were quantified by qPCR and equimolar concentrations were amplified by emulsion PCR and 50 bp paired end sequencing was done on the AB 5500xl SOLiD deep sequencer (Applied Biosystems).

Sequencing reads were aligned to the *Oryctolagus cuniculus* genome (ensembl, release-70, <ftp://ftp.ensembl.org/pub/release-70/fasta/oryctolagus_cuniculus/>) using the Bioscope 1.3 Whole Transcriptome Analysis Pipeline software package (Applied Biosystems). HTSeq-count v0.5.3 was used to calculate the number of reads per transcript. The DESeq v1.4.1 R package (bioconductor.org) was used for calculating differential expression between groups. Transcripts with adjusted p-values < 0.05 were considered differentially expressed.

Tuxedo Suite

Determination of differential expression was done using the Tuxedo protocol as described in Trapnell *et al* 2012 [17]. Briefly, raw transcript reads are aligned to a reference genome using TopHat. The aligned transcripts from TopHat are then passed to Cufflinks in which transcripts are assembled. Because it is possible that not all isoforms of a gene may be expressed in a cell at a given time, it is necessary to create a definition of a gene which includes all isoforms. The Cuffmerge tool is used to merge transcript assemblies from multiple transcript assembly files to create a comprehensive view of the gene. Lastly Cuffdiff is used to calculate differential expression and CummeRbund was used for interacting with the data.

Ingenuity Pathway Analysis (IPA)

Because IPA does not officially supports the rabbit model, rabbit gene names were converted to orthologous mouse gene names. Fragment reads per kilobase pairs (FPKM) and adjusted p-values were calculated using the DESeq package. Pathway analysis was restricted to genes that met the following conditions: 3x (log2) differential expression, lung organ restricted, non-cancer cell line, and non-neurological cell. Pathway analysis was done using the built in Core Analysis and Functional Gene Set Enrichment tools.

Gene Set Enrichment Analysis (GSEA)

To confirm the functional gene set enrichments identified by through the IPA platform, a secondary analysis was done using the freely available Gene Set Enrichment Analysis (GSEA) software (Broad Institute) [15, 16]. The same starting data table with orthologous mouse gene names and the respective p-values were used for the analysis. Curated functional gene sets from the Reactome database were used.

Results

Differentially expressed genes

RNA was isolated from 3 distinct tissue types: cavity wall, uninvolved, and naive **(Figure 3-1)**. There were a total of 12,117 mapped transcripts. 8737 of these transcripts were successfully converted to a mouse orthologue gene IDs for use in pathway analysis through Ingenuity Pathway Analysis (IPA) or Gene Set Enrichment Analysis (GSEA) tools. The remaining 3380 transcripts were hypothetical or did not share a orthologue with the mouse genome. 903 putative unnamed genes were differentially expressed in the cavity wall and uninvolved lung tissue. The 903 genes further breaks down into 196 and 807 genes that were upregulated in the cavity wall and uninvolved lung tissue respectively. The naive and uninvolved samples clustered closer together when comparing the global expression changes, and the cavitary sample was distinctively different (**Figure 3-2**).

Analysis was done using Fragments Per Kilobase of exon per Million fragments mapped (FPKM). The FPKM value provides a normalized value which allows for the relative comparison of genes with different transcript length. The MMP class of enzymes was well represented among the top 20 overexpressed genes in the cavity wall, consisting of *mmp-1, mmp-13, and mmp-3* **(Table 3-1)**. While there were many genes that were upregulated in the cavitary tissue compared to the uninvolved tissue, there was only 1 gene that were uniquely expressed only in the cavitary tissue at high abundance, *q2lda4*. Other genes that were uniquely expressed in the cavity wall were present at FPKM reads of less than 50 and were considered low abundance transcripts.

Differentially expressed pathways

Use of the IPA platform yielded functional gene sets involving the inflammatory response, infectious disease response, respiratory disease, and connective tissue disorders that were all found to be upregulated in the cavity wall **(Table 3-2)**. Pathways involved with extracellular matrix remodeling were also found to be significantly differentially expressed in the cavity wall tissue (**Table 3-2 and Table 3-3)**.

For validation of the IPA results, we conducted a second pathway analysis using the GSEA software tool. The GSEA tool is an open ended pathway analysis tool in which the user supplies a functional gene list with the corresponding gene identifiers. For our analysis we used the KEGG and Reactome functional gene sets. Upregulation of the inflammatory response was also identified using the GSEA software tool, suggesting that IPA identified pathways were in fact differentially expressed **(Figure 3-3)**. Additional pathways such as the cell death and cell proliferation pathways were also identified using the GSEA tool, however due to the different definitions of functional gene sets across the KEGG, Reactome, and IPA libraries, it was not always possible to find identical functional gene set definitions across the different libraries. Lastly, the libraries require different gene identifier annotations which creates another layer of complexity when trying to directly compare gene sets across platforms. While we feel confident that there is a similarity among the pathway analysis using the KEGG, Reactome, and IPA libraries, quantitation of the overlap proved to be difficult. For these reasons we will focus only on the data generated from the IPA analysis.

The process of inflammation is known to be involved with tuberculosis disease [19, 20]. Inflammation is a host immune response that describes processes such as the release of chemokines and cytokines, increased vascular permeability, recruitment of immune cells, and immune cell proliferation. It has been shown that naive macrophages are recruited to the site of *mycobacterium* infection to attempt to control the spread of bacteria [21, 22]. Differential expression of 104 genes comprising the cellular growth and proliferation pathway were differentially expressed and the pathway was found to be enriched in the cavitary tissue compared to the uninvolved tissue (p=1.41E-16). Cellular proliferation is most likely due to the activation of the immune system and proliferation of immune cells. Cellular proliferation would suggest that the disease state is in an inflammatory stage.

Also supporting the process of a local inflammatory response at the site of cavitation are upregulation of cellular migration pathways. There were 47 genes differentially expressed in the in the immune cell trafficking pathway and the pathway was found to be upregulated in the cavitary wall (p= 3.54E-14). There were 44, 34, and 26 genes differentially expressed in the pathways involving the activation of leukocytes, monocytes, and T-cells respectively and the pathways were enriched in the cavitary wall tissue (p={5.25E-15, 1.86E-12, 2.30E-10}). The enrichment of cell proliferation, cell migration, and cell activation pathways in the cavity wall tissue suggests that cavitary lesions are associated with the recruitment of activated immune cells.

Tissue destruction and cell death are observed in cavitary lesions. Cell death can occur through apoptosis which is a programmed cell death pathway, or through necrosis which is a non-programmed cell death pathway. Our data indicates that both processes are enriched for in the cavitary lesion. 70 genes are differentially expressed in the apoptosis pathway (p= 4.48E-9) and 55 genes in the necrosis pathway (p = 9.79E-9).

IFN-gamma signaling was predicted to be a significant transcriptional regulator in the cavitary lesion. A putative signaling cascade modeling IFN-gamma signaling network was created (**Figure 3-4)**. Enrichment of the IFN-gamma network is associated with a proinflammatory immune state. NFkB activation is of interest because there remain conflicting reports about the involvement of NFkB in the immune response to tuberculosis [23, 24]. NFkB is known to influence T cell division and also promote the production of the proinflammatory cytokine IL-6. Cavitary lesion development may be a specific situation in which NFkB is upregulated and helps drive a proinflammatory response.

Lastly, it is possible to make a de novo pathway map that shows the most likely signaling relationships based on the expression data set. In this study we developed a model that described a relationship that incorporates the relationship between TNF-alpha, a major factor in the inflammation process, and with extracellular matrix remodeling proteases such as MMP-1 **(Figure 3-5)**. Both of these factors have been reported in the literature to be upregulated at both the RNA and protein level, consistent with our current model [3, 5, 21, 25-27].

Discussion

The rabbit build used for the analysis of the sequencing data (GenBank Assembly ID GCA_000003625.1, release build 70) has been sequenced to a 7x coverage depth and the overall depth of coverage and annotation quality are not at the current standard as model organisms such as the mouse or rat genomes. It was estimated that about 80% of the genome was properly anchored to a chromosome, and the remaining sequences were annotated as a virtual chromosome. While the genome build quality was sufficient for the RNA seq analysis, there are currently some limitations. It would be possible to re-run the sequencing analysis using an updated reference sequence to improve the annotation at a later date.

It was also surprising that the expression data from uninvolved lung tissue harvested from *M. tb* infected animals clustered better with lung tissue from naive, non-infected rabbits. Bacteria was culturable from the uninvolved lung tissue and it is therefore not possible to attribute the similarity between the uninvolved and naive tissue as being because both tissue lacked bacilli. We cannot rule out that there is a threshold of bacterial burden that needs to be reached in order to observe expression changes that differ from naive lung.

Another possible explanation for why the global gene expression of uninvolved tissue clusters well with the naive tissue could be due to our infection model. Rabbits are infected by bronchoscope and a bolus infectious dose is deposited in right lower lung lobe. It could be possible that the infection is so intense and focused in a discrete area that there is immune cell depletion in other areas of the lung as intensive immune cell trafficking is targeted to the site of infection.

Despite the limitations of some the current genome build there is still a considerable amount of data that was generated and is interpretable. A number of previously identified immune related pathways were identified in our study and identification of these pathways serve as a good control for our data set and analysis. Upregulation of the inflammatory response is typical of tuberculosis and that finding would be expected to be represented at the gene expression level.

More research is needed to investigate what the major mechanism of cell death is during cavitary disease. It is not possible from our data set to extrapolate which pathway is the predominant death pathway. Identification of which cell death pathway is predominant would allow for further research investigating if modulating the cell death pathway towards either necrotic or apoptotic pathways would be beneficial for the host in the context of cavitary lesion development.

Traditional explanations about the process of cavitary lesion development have focused on necrotic and proinflammatory processes. However, neither of these explanations specifically address the process for breaking down the extracellular matrix. Involvement of the MMP class of enzymes in the destruction of the extracellular matrix provides a testable hypothesis for the specific mediator of extracellular matrix degradation. It is therefore encouraging that our expression data reflects both the proinflammatory response and additionally the specific involvement of the MMP class of enzymes.

References

1. World Health Organization (2013). Global tuberculosis report 2013.

2. Blumberg, H. M., Burman, W. J., Chaisson, R. E., Daley, C. L., Etkind, S. C., Friedman, L. N., Fujiwara, P., Grzemska, M., Hopewell, P. C., Iseman, M. D., et al. (2003). American Thoracic Society/Centers for Disease Control and Prevention/Infectious Diseases Society of America: treatment of tuberculosis. Am J Respir Crit Care Med *167*, 603–662.

3. Elkington, P., Shiomi, T., Breen, R., Nuttall, R. K., Ugarte-Gil, C. A., Walker, N. F., Saraiva, L., Pedersen, B., Mauri, F., Lipman, M., et al. (2011). MMP-1 drives immunopathology in human tuberculosis and transgenic mice. J. Clin. Invest. *121*, 1827–1833.

4. Elkington, P. T., D'Armiento, J. M., and Friedland, J. S. (2011). Tuberculosis immunopathology: the neglected role of extracellular matrix destruction. Science Translational Medicine *3*, 71ps6–71ps6.

5. Ugarte-Gil, C. A., Elkington, P., Gilman, R. H., Coronel, J., Tezera, L. B., Bernabe-Ortiz, A., Gotuzzo, E., Friedland, J. S., and Moore, D. A. J. (2013). Induced sputum MMP-1, -3 & -8 concentrations during treatment of tuberculosis. PLoS ONE *8*, e61333.

6. Subbian, S., Tsenova, L., O'Brien, P., Yang, G., Kushner, N. L., Parsons, S., Peixoto, B., Fallows, D., and Kaplan, G. (2012). Spontaneous Latency in a Rabbit Model of Pulmonary Tuberculosis. Am J Pathol.

7. Subbian, S., Tsenova, L., Yang, G., O'Brien, P., Parsons, S., Peixoto, B., Taylor, L., Fallows, D., and Kaplan, G. (2011). Chronic pulmonary cavitary tuberculosis in rabbits: a failed host immune response. Open Biol *1*, 110016.

8. Lin, P. L., Rodgers, M., Smith, L., Bigbee, M., Myers, A., Bigbee, C., Chiosea, I., Capuano, S. V., Fuhrman, C., Klein, E., et al. (2009). Quantitative comparison of active and latent tuberculosis in the cynomolgus macaque model. Infect Immun *77*, 4631–4642.

9. Helke, K. L., Mankowski, J. L., and Manabe, Y. C. (2006). Animal models of cavitation in pulmonary tuberculosis. Tuberculosis *86*, 337–348.

10. Orme, I., and Gonzalez-Juarrero, M. (2007). Animal models of M. tuberculosis Infection. Current protocols in microbiology *Chapter 10*, Unit 10A.5.

11. Dannenberg, A. M. (2006). Pathogenesis of Human Pulmonary

Tuberculosis: Insights from the Rabbit Model. ASM Press.

12. Trapnell, C., Hendrickson, D. G., Sauvageau, M., Goff, L., Rinn, J. L., and Pachter, L. (2013). Differential analysis of gene regulation at transcript resolution with RNA-seq. Nat Biotechnol *31*, 46–53.

13. Wang, Z., Gerstein, M., and Snyder, M. (2009). RNA-Seq: a revolutionary tool for transcriptomics. Nat Rev Genet *10*, 57–63.

14. Schulze, A., and Downward, J. (2001). Navigating gene expression using microarrays--a technology review. Nat. Cell Biol. *3*, E190–5.

15. Subramanian, A., Tamayo, P., Mootha, V. K., Mukherjee, S., Ebert, B. L., Gillette, M. A., Paulovich, A., Pomeroy, S. L., Golub, T. R., Lander, E. S., et al. (2005). Gene set enrichment analysis: a knowledge-based approach for interpreting genome-wide expression profiles. Proc Natl Acad Sci USA *102*, 15545–15550.

16. Mootha, V. K., Lindgren, C. M., Eriksson, K.-F., Subramanian, A., Sihag, S., Lehar, J., Puigserver, P., Carlsson, E., Ridderstråle, M., Laurila, E., et al. (2003). PGC-1alpha-responsive genes involved in oxidative phosphorylation are coordinately downregulated in human diabetes. Nat Genet *34*, 267–273.

17. Trapnell, C., Roberts, A., Goff, L., Pertea, G., Kim, D., Kelley, D. R., Pimentel, H., Salzberg, S. L., Rinn, J. L., and Pachter, L. (2012). Differential gene and transcript expression analysis of RNA-seq experiments with TopHat and Cufflinks. Nat Protoc *7*, 562–578.

18. Nedeltchev, G. G., Raghunand, T. R., Jassal, M. S., Lun, S., Cheng, Q.-J., and Bishai, W. R. (2009). Extrapulmonary dissemination of Mycobacterium bovis but not Mycobacterium tuberculosis in a bronchoscopic rabbit model of cavitary tuberculosis. *77*, 598–603.

19. Kaufmann, S. H. E., and Dorhoi, A. (2013). Inflammation in tuberculosis: interactions, imbalances and interventions. Curr Opin Immunol *25*, 441–449.

20. Sasindran, S. J., and Torrelles, J. B. (2011). Mycobacterium Tuberculosis Infection and Inflammation: what is Beneficial for the Host and for the Bacterium? Front Microbiol *2*, 2.

21. Algood, H. M. S., Chan, J., and Flynn, J. L. (2003). Chemokines and tuberculosis. Cytokine Growth Factor Rev. *14*, 467–477.

22. Davis, J. M., and Ramakrishnan, L. (2009). The role of the granuloma in expansion and dissemination of early tuberculous infection. Cell *136*, 37–49.

23. Dhiman, R., Raje, M., and Majumdar, S. (2007). Differential expression of NF-kappaB in mycobacteria infected THP-1 affects apoptosis. Biochim Biophys Acta *1770*, 649–658.

24. Pathak, S. K., Basu, S., Basu, K. K., Banerjee, A., Pathak, S., Bhattacharyya, A., Kaisho, T., Kundu, M., and Basu, J. (2007). Direct extracellular interaction between the early secreted antigen ESAT-6 of Mycobacterium tuberculosis and TLR2 inhibits TLR signaling in macrophages. Nat Immunol *8*, 610–618.

25. Lin, P. L., Myers, A., Smith, L., Bigbee, C., Bigbee, M., Fuhrman, C., Grieser, H., Chiosea, I., Voitenek, N. N., Capuano, S. V., et al. (2010). Tumor necrosis factor neutralization results in disseminated disease in acute and latent Mycobacterium tuberculosis infection with normal granuloma structure in a cynomolgus macaque model. Arthritis Rheum *62*, 340–350.

26. Casarini, M., Ameglio, F., Alemanno, L., Zangrilli, P., Mattia, P., Paone, G., Bisetti, A., and Giosuè, S. (1999). Cytokine levels correlate with a radiologic score in active pulmonary tuberculosis. Am J Respir Crit Care Med *159*, 143–148.

27. Clay, H., Volkman, H. E., and Ramakrishnan, L. (2008). Tumor necrosis factor signaling mediates resistance to mycobacteria by inhibiting bacterial growth and macrophage death. Immunity *29*, 283–294.

Figures

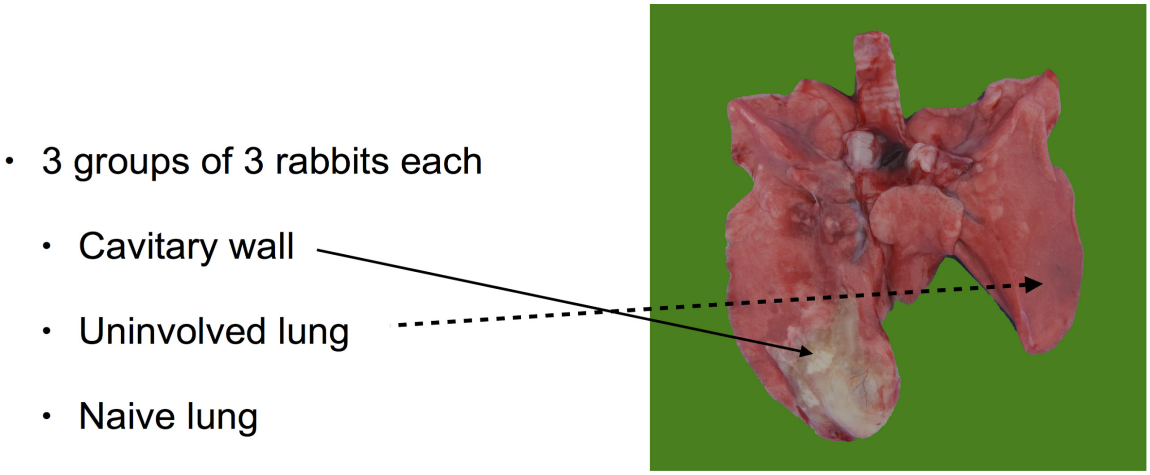

- 3 groups of 3 rabbits each
  - Cavitary wall
  - Uninvolved lung
  - Naive lung

Figure 3-1: RNA tissue sampling

Lungs were harvested from presensitized New Zealand White rabbits after the cavities were confirmed by CT scan. RNA was isolated from specific regions as determined by gross pathology. RNA was additionally isolated from a naive, non-infected rabbit. Rabbits were infected using by bronchoscope and the infection is largely localized to the site of bacterial suspension instillation.

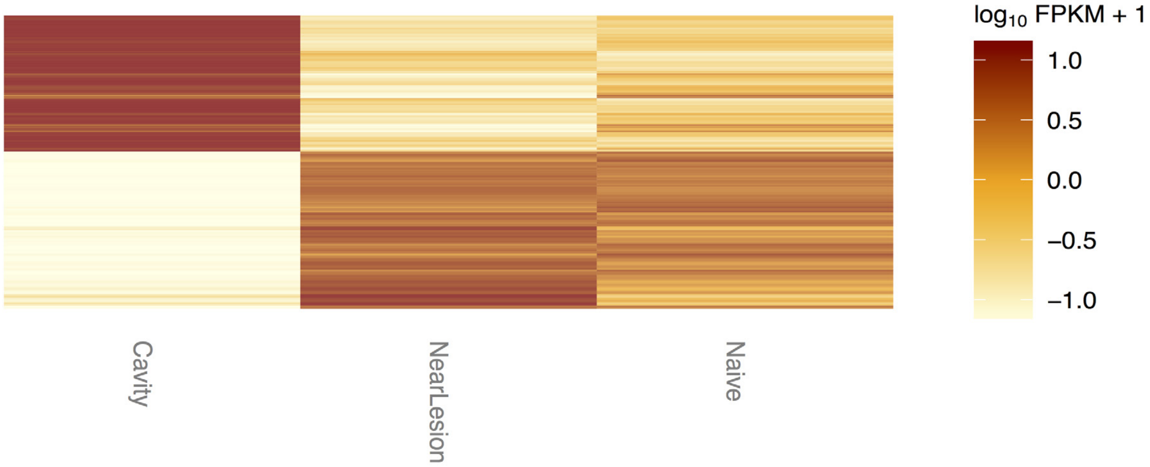

Figure 3-2: Tuxedo global clustering

A heatmap representing the global gene expression changes among the samples collected. The gene expression pattern was distinctively different compared to the uninvolved and cavity wall tissue. The uninvolved and naive tissue samples displayed a higher amount of clustering than originally anticipated. Because CFUs were culturable from the uninvolved tissue from *M. tb* infected animals it the major difference in gene expression clustering between cavity wall and uninvolved tissue is not simply due to the presence or absence of bacteria.

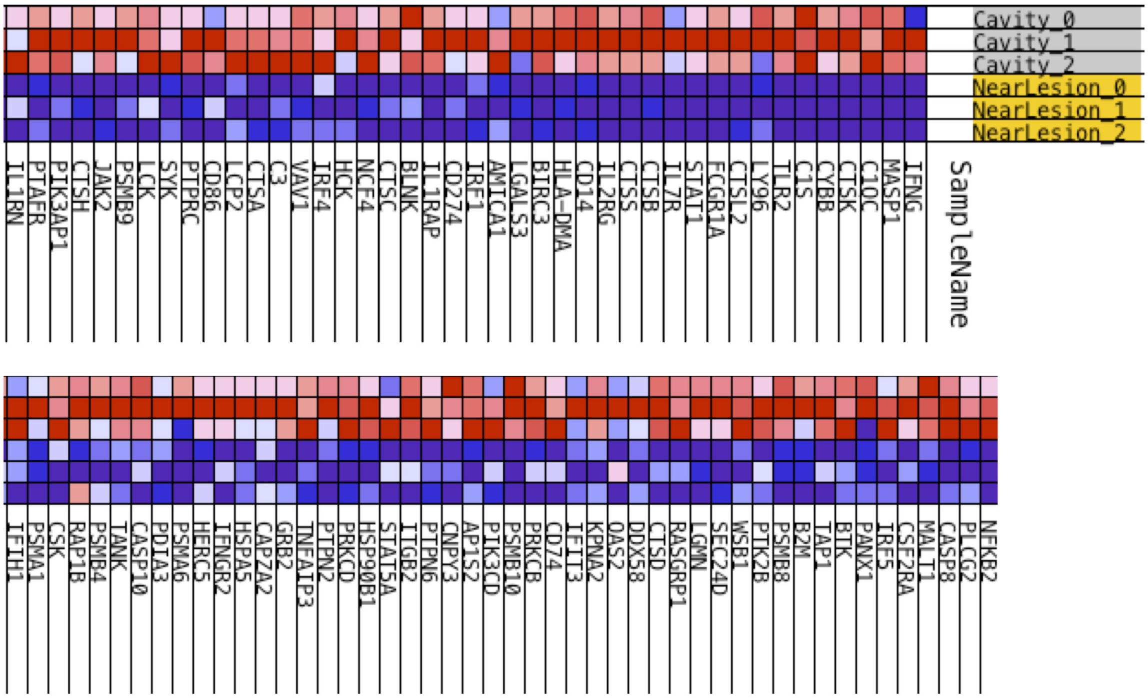

Figure 3-3: Reactome immune response gene set

In addition to the IPA functional gene set analysis, the freely available GSEA software was used as well. A list of functional gene sets was downloaded from the reactome database and a functional gene set enrichment analysis was done. Similar to the IPA results, the immune response functional set was also found to be upregulated in the cavity wall sample. Similar identification of upregulated pathways using different functional gene set definitions and different analysis software provides support that the identified functional pathways are truly differentially expressed.

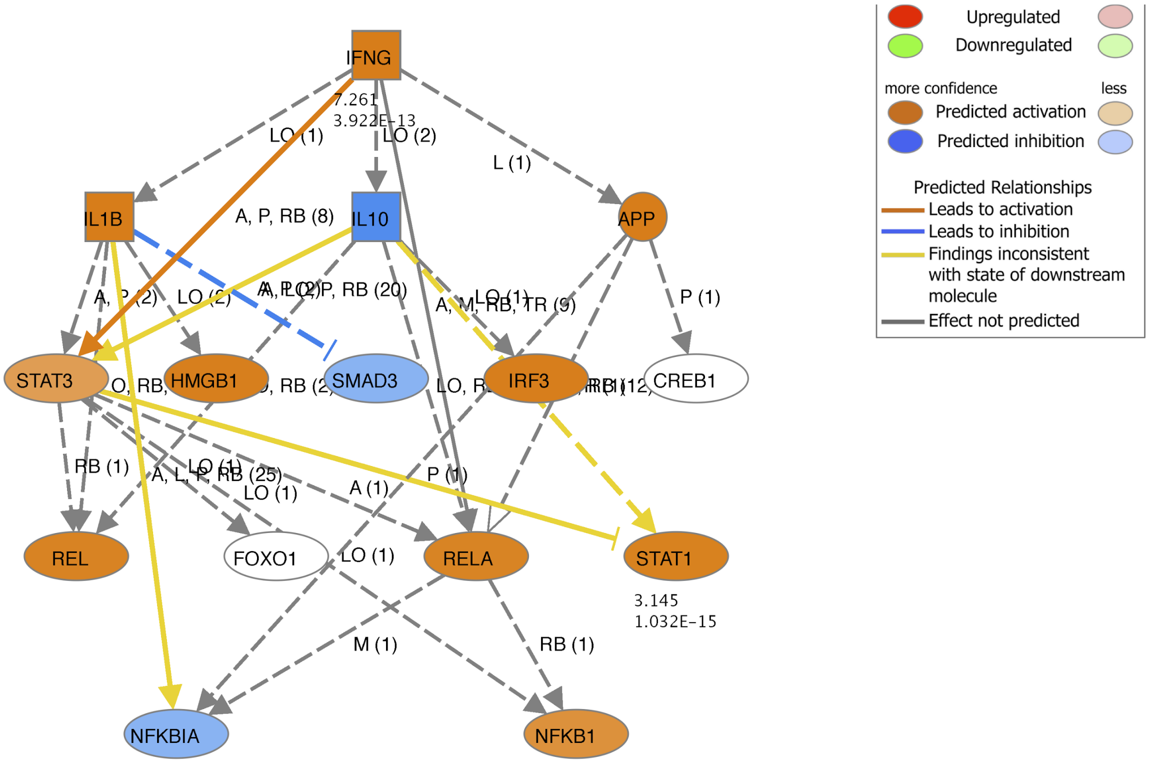

Figure 3-4: IPA IFN-gamma network

IFN gamma is known to be important for the a successful host response to *Mycobacterium tuberculosis*. This network describes the putative cavitary disease associated IFN gamma signaling network.

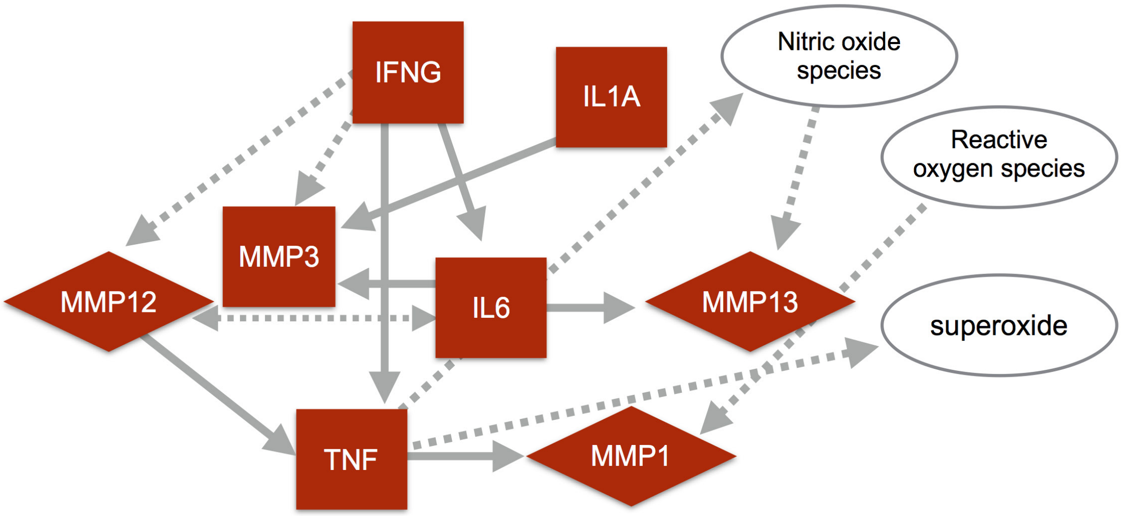

Figure 3-5: IPA cavity signaling

A novel network summary that best describes the gene expression changes measured in the cavitary wall compared to the uninvolved lung tissue. MMP-1 and and TNF alpha play a central role in the map and it has previously been suggested that both of these host factors are important for the development of cavitary lesions. This putative map describes the combined involvement of both inflammatory and tissue remodeling processes in cavitary disease development.

Table 3-1: Top 10 most upregulated genes present in cavitary tissue.

A list of the most upregulated genes present in the cavity wall tissue compared to the uninvolved tissue. *mmp1, mmp13, mmp3,* and *cthrc1* are involved with maintenance and remodeling of the extracellular matrix in part due to their functional ability of cleaving collagen.

Gene Name	log2 fold change	adj. p
mmp-1	11	9.77E-55
bozyq7 (cxcl13)	10	5.87E-24
b6a7p9	9	4.49E-11
q8hyv6	9	4.27E-23
vtnc	8	1.37E-08
mmp-13	8	1.49E-24
ubd	8	1.87E-26
mmp-3	8	3.32E-36
cthrc1	7	1.87E-26
ifn-gamma	7	3.32E-36

Table 3-2: IPA core analysis functional gene sets

Significantly differentially regulated gene sets in the cavitary compared to uninvolved samples. Of the functional gene sets identified, the majority were related to inflammation and the immune response. The table was generated using the IPA software package. The inflammatory pathway and connective tissue disorders pathways were significantly upregulated. The connective tissue disorders gene set includes the upregulation of proteases such as the MMP class of enzymes.

	p-value	# of Molecules
Diseases and Disorders		
Inflammatory Response	5.25E-15 - 2.49E-04	79
Connective Tissue Disorders	3.76E-11 - 1.44E-05	27
Inflammatory Disease	3.76E-11 - 1.01E-10	26
Skeletal and Muscular Disorders	3.76E-11 - 1.01E-10	26
Immunological Disease	1.01E-10 - 2.44E-04	24
Molecular and Cellular Functions		
Cell-To-Cell Signaling and Interaction	6.21E-17 - 2.49E-04	82
Cellular Growth and Proliferation	1.41E-16 - 2.70E-04	109
Cellular Function and Maintenance	1.29E-14 - 2.51E-04	69
Cellular Movement	3.54E-14 - 2.44E-04	68
Cellular Development	1.30E-12 - 2.70E-04	94
Physiological System Development and Function		
Hematological System Development and Function	7.82E-18 - 2.70E-04	103
Tissue Morphology	7.82E-18 - 1.92E-04	73
Immune Cell Trafficking	5.25E-15 - 2.49E-04	68
Humoral Immune Response	5.81E-12 - 2.38E-04	29
Cell-mediated Immune Response	6.33E-11 - 2.51E-04	38

Table 3-3: IPA core analysis molecules

Molecules that were upregulated in the cavity sample. MMP1, MMP13, and MMP3 were among the most upregulated molecules identified by IPA. The MMP family of enzymes have been shown to have functional roles in remodeling the extracellular matrix.

	p-value
Top Canonical Pathways	
Hepatic Fibrosis	2.36E-10
Role of HyperCytokinemia in the Pathogenesis of Influenza	1.17E-09
Atherosclerosis Signaling	1.39E-09
Role of Osteoblasts, Osteoclasts and Chondrocytes in Rheumatoid Arthritis	2.8E-08
Pathogenesis of Multiple Sclerosis	1E-07
Top Molecules	Log2 fold Increase
MMP1	10.990
MMP13	8.145
UBD	7.699
MMP3	7.638
IFNG	7.261
CTLA4	7.066
CMA1	6.816
HAVCR1	6.586
CXCL11	6.496
CELA1	6.406

Chapter 4: Small molecule inhibition of MMP-1 alters pathology in a rabbit model of tuberculosis.

Abstract

Rationale: The development of cavitary lesions is an important risk factor to disease transmission and antibiotic treatment failure in tuberculosis. Inhibition of cavitary lesion development could be an important adjunctive therapy for treatment of tuberculosis, as none of the current drugs used for the treatment of tuberculosis have any specific activity aimed at the inhibition of cavity formation. **Objective:** Breakdown of the extracellular matrix requires the activity of special enzymes of the matrix metalloprotease (MMP) class. MMP-1 is upregulated in tuberculosis patients and this enzyme is thought to be important for remodelling of the extracellular matrix. RO32-3555 is a small molecule inhibitor of MMP-1 and it is hypothesized that inhibition of MMP-1 will inhibit the development of cavitary lesions. **Methods:** New Zealand White rabbits were presensitized and infected with *M. tb* H37Rv by bronchoscopy. Rabbits were divided into three groups and treated with either RO32-3555, INH, or vehicle alone daily. Disease progression was monitored by weekly breath hold CT scans acquired at 20 cm of water pressure. At necropsy lungs were fixed with formalin at a set pressure of 20 cm and the fixed lungs were analyzed by histopathology. **Main Results:** In the first infection group, the RO32-3555 treated animals showed reduced lung pathology by CT up until 2 weeks postinfection (week 2, $p<0.001$). The RO32-3555 treated

animals showed the highest lung consolidation at week 5 (p<0.001). In the second study, the RO32-3555 group showed the greatest amount of lung consolidation at week 2 post infection (p<0.001). Rabbits developed cavities in all treatment groups but the size and volume of cavities was lowest in the RO32-3555 group. **Conclusions:** Preliminary data suggest that use of the inhibition of MMP-1 by RO32-3555 can alter tuberculosis associated pathology.

Introduction

Tuberculosis (TB) was responsible for 1.3 millions deaths in 2012 [1]. The disease is caused by the pathogen *Mycobacterium tuberculosis* (*M. tb)*. During the early stages of infection *M. tb* is phagocytosed by host alveolar macrophages and additional lymphocytes are recruited to the site of infection to form a granuloma. Cellular recruitment and lung matrix remodeling during granuloma development serve the purpose of creating an isolated microenvironment for containment of the bacilli [2-6].

Studies have shown that tumor necrosis factor alpha (TNF-α) is important for proper granuloma formation and that inhibition of TNF-αresults in a granuloma disorganization [7-9]. Other studies have shown that the addition of TNF-αinhibitors to the standard tuberculosis antibiotic regimen results in faster clearance of bacteria from the host [10]. Liquefaction of the granuloma lesion is suggested to precede the formation of a cavitary lesion [11].

Reduced lung pathology and cavitation have been observed in immunosuppressed HIV-TB coinfected individuals [12-15]. It is predicted that the host matrix metalloproteinase (MMP) class of enzymes are responsible for remodeling of the lung extracellular matrix during *M. tb* infection [16-18]. Taken together, these data suggest that tissue destruction is driven by a host mediated response and not a direct action by the bacteria.

Bacteria are able to replicate to high numbers in the cavity and a combination of the high bacterial numbers and cavity structure contribute to presence of cavitary lesions as being a risk factor for transmission and antibiotic treatment failure [19-21]. Therefore, inhibiting cavity lesion formation may reduce the relative infectiousness of an individual and reduce the rate of antibiotic treatment failure.

The standard treatment regimen for tuberculosis consists of isoniazid, rifampicin, ethambutol, and pyrazinamide. None of the previously mentioned drugs possess any anti-MMP activity and none of the drugs directly inhibits tissue destruction processes. Inhibition of lung matrix remodelling would be an attractive adjunctive therapy that could be introduced for TB treatment [17, 18]. Destruction of the extracellular matrix is not a quickly reversible process and changes such as cavitation may persist [22, 23]. Therefore it would seem that prevention of tissue remodeling would be the preferential.

The main mechanical extracellular matrix components of the lung are collagen (type 1 and IV) and elastin [24]. The MMPs that are capable of cleaving collagen are MMPs 1, 8, and 13. MMP 9 is a gelatinase but it also possesses collagenase activity [25]. MMP-1 has previously been reported to be elevated in tuberculosis patients [13, 16]. Additionally in a humanized mouse model expressing the human *mmp-1* gene, mice infected with *M. tb* developed disease pathology more closely resembling human disease pathology [17].

In this study we hypothesised that the inhibition of MMP-1 would reduce the lung pathology that is typically observed in tuberculosis. Rabbits, not mice, express MMP-1 in the lung and therefore we tested our hypothesis by treating *M. tuberculosis* infected rabbits with RO32-3555 (Trocade) and graded lung pathology by non-invasive computed tomography (CT) imaging and by histopathology [17, 26]. RO32-3555 is a pharmacologically relevant small molecule inhibitor of MMP-1 which has been shown to be safe in humans [26]. Inhibition of tissue destructive processes would be an attractive adjunctive tuberculosis therapy.

Methods

Ethics Statement

All animal experiments were carried out in strict accordance with the recommendations in the “Guide for the Care and Use of Laboratory Animals of the National Institutes of Health” and all procedures were approved by the Johns Hopkins University Animal Care and Use Committee.

Set pressure CT imaging

Rabbits were anesthetized with ketamine (20 mg/kg), xylazine (5 mg/kg), and acepromazine (10 mg). Animals were maintained under 3 L/min O_2 and 1% isoflurane for the duration of the imaging. Because the imaging facility is located in a BSL-2 facility, the infected animals were placed into a biosafety imaging chamber. This chamber allowed for the filtration of gas exchange and for the safe transport of the animal.

Rabbits were intubated with a 3.0 mm cuffed endotracheal tube. The endotracheal tube was connected to a Y-port in which one connection was exposed to the ambient environment of the container and was controlled by an on/off valve. The other Y-port was connected to the gas supply. Pressure was regulated by sealing the port connected to the ambient environment of the inside of the container and thus creating a closed system with the gas supply. The pressure of the gas supply was set by adjusting the height of a water trap to the desired depth of either 20 cm of water.

Image processing, segmentation, ROIs, and longitudinal coregistration

Images were preprocessed using FIJI (NIH). Image segmentation was done using the AMIRA (Visualization Science Group) software package. Pathological regions of interest (ROI) were manually segmented from individual slices. The esophagus and main bronchi were segmented and removed from analysis of the lung region.

Rigid coregistration of longitudinal data sets was done using the coregistration tool in Amira. Image sets were coregistered by using the skeletal bones as a guide.

Sensitization and infection

Adult female New Zealand White rabbits weighing 3.5-4.0 kg were used for this study. *M. bovis* was grown in 7H9 broth culture, cell density was adjusted to a concentration of 1 x 10^9 CFU/ml, and heat killed at 72 C for 3 hours. The heat killed suspension was mixed 1:1 with Freund's incomplete adjuvant and 0.2 mls of this suspension was administered for the sensitization injections. Rabbits were given a series of 5 sensitization injections over the course of 2.5 weeks and then the rabbits were rested for an additional 2.5 weeks.

Rabbits were anaesthetized with a combination of ketamine, xylazine, and acepromazine. Anaesthetized rabbits were infected with live, virulent *Mycobacterium tuberculosis* H37Rv strain using a bronchoscope. 0.4 mL of a bacterial suspension was deposited in the lung and the total CFU was determined by plating the inoculum on 7H10 plates. For the first infection study animals were infected with bacteria that were previously frozen at -80C and thawed the day of infection. For the second infection study rabbits were challenged with actively growing, log-phase cultures.

Necropsy

Rabbits were anaesthetized with a combination of ketamine, xylazine, and acepromazine and then euthanized with Euthasol euthanasia solution. The lungs were fixed with 10% neutral buffered formalin (NBF) by hanging a bag containing

10% NBF at 20 cm above the surface of the safety cabinet in which the necropsy was performed. The thoracic ribs were removed to expose the heart and lungs. While leaving the organs inside the animal, the lungs were flushed through the trachea 4x with 30 mls of Ringer’s solution. A line connected to a reservoir of 10% NBF was placed in the trachea. The trachea was tied off with sutures to create a closed system with the bag of 10% NBF and the lungs. The lungs were insufflated with 10% NBF for 30 minutes and the heart/lung block were removed from the rabbit and placed in a jar containing 500 mls of 10% NBF. After 24 hours the heart/lung block was trimmed and the trimmed lungs were returned to fresh 10% NBF.

Histology

Formalin fixed paraffin embedded tissues were sectioned and stained by Histoserv (Germantown, MD). Serial sections were stained with H&E, acid fast, Masson’s trichrome, and picrosirius red stains. Pathology assessment was performed by a trained veterinary pathologist.

Oral dosing of rabbits

RO32-3555 (Roche, USA) was resuspended in Pediasure (Abbott Nutrition, Ohio) at a concentration of 100 mg/ml. Rabbits were treated orally with 100 mg/kg of RO32-3555 on weekdays. Vehicle control rabbits were given Pediasure alone and INH treated rabbits were given 25 mg/kg or INH dissolved in water. Drug or vehicle solutions were administered with a veterinary feeding needle at the back of the tongue to ensure the animals swallowed the dose. Treatment was provided daily on weekdays beginning the day after infection.

Results

Group 1

Rabbits were infected with 4.01 (log10) CFU of *M. tb* H37Rv from a frozen stock. Following infection rabbits were treated with RO32-3555, INH, or vehicle daily on weekdays **(Figure 4-1)**. Rabbits in the INH treatment group began losing weight rapidly after treatment. Treatment was halted for 1 week and the animals were allowed to regain their weight. Following the weight gain, rabbits in the INH treatment group resumed their treatment but INH was dissolved in water instead of Pediasure. The rabbits did not have any further weight loss complications after the change of the INH vehicle solution.

Lung consolidation was monitored by weekly breath hold CT imaging. RO32-3555 treated rabbits showed reduced lung consolidation at early timepoints up until 2 weeks post infection ($p<0.001$ at week 2), but the effect of the drug was lost at later timepoints. At weeks 4 and 5 postinfection, the RO32-3555 treated rabbits showed the highest lung consolidation relative to the other treatment groups ($p<0.001$ for week 4 and 5). The INH treated rabbits consistently showed the least amount of lung consolidation **(Figure 4-2).**

Animals were necropsied after 5 weeks post infection and lungs were harvested and formalin fixed for histopathology. It was also observed that the RO32-3555 treated animals showed the presence of vasculitis as determined by histopathology **(Figure 4-3).** The presence of vasculitis was also observed in the vehicle control group but not in the INH treated group. While the frequency of occurrence was not different in RO32-3555 versus the vehicle group, however the severity of vasculitis appeared to be worse. Vasculitis had not been previously associated as a side effect of the drug.

Group 2

Rabbits were infected with with 4.24 (log10) log-phase growth *M. tb* H37Rv. Following infection rabbits were treated with RO32-3555, INH, or vehicle daily on weekdays **(Figure 4-4)**. Due to the complications that arose from the INH being resuspended in Pediasure as a vehicle, water was used vehicle solution for INH. No weight loss issues were observed.

Lung consolidation was monitored weekly as previously described. Imaging was done at preinfection and at day 7 and day 14 postinfection **(Figure 4-5)**. Animals were necropsied after 2 weeks post infection and lungs were harvested and formalin fixed for histopathology.

The relative amount of lung consolidation represented by the 3 treatment groups did not follow the same trend that was observed in the first group. At week 1 there was no significant difference between treatment groups. At week 2 the RO32-3555 treated group showed increased lung consolidation relative to the vehicle and INH treated group ($p<0.05$ and $p<0.001$ respectively) **(Figure 4-6)**.

Between week 1 and week 2, the volume of the main lesion had increased in the RO32-3555 group in contrast to the INH and vehicle only groups in which the volume had decreased **(Figure 4-7A)**. In a related measurement, it was also observed that the total lung volume decreased in the RO32-3555 treated animals in contrast to an increase in total lung volume in the INH and vehicle treated groups **(Figure 4-7B)**. Most likely the increase in lung volume can be attributed to a decrease in lung consolidation and a relative increase in “healthy” lung tissue. A breath hold CT protocol is used in which the animals lungs are inflated to a set pressure. Normal lung tissue is able to inflate and expand under the increase in air pressure, but the consolidated lung tissue is not as pliable and allows for relatively little expansion. It would therefore follow that an increase in the volume of the main lesion would lead to a relative decrease in the total lung volume of the inflated lung.

Cavities, unlike the first infection group, were observed in all treatment groups by CT imaging. The number of cavities and the size of cavities were lowest in the RO32-3555 treatment group as compared to the other treatment groups **(Table 4-1)**. Histopathology showed the presence of a cavitary lesion in 1 additional rabbit from the vehicle control group that was not observed by CT

Discussion

Two groups of animals were infected and treated orally with RO32-3555, INH, or vehicle alone as a control. In the first group of infections, rabbits were infected using a titrated frozen stock of bacteria. Bacteria were thawed, and directly used for animal infections. The rabbits appeared to be clearing the infection, and all treatment groups showed a decrease in lung consolidation over time and each treatment group returned to near baseline levels of lung consolidation by the end of the study. This can most likely be attributed to a decrease in fitness from the freeze-thawed cells and 10^4 CFU of the titrated frozen stock may not show equivalent growth in an animal host as 10^4 CFU from a freshly growing broth culture. Infections were done in this manner as an attempt to decrease the amount of variation across rabbit studies. However, this seemed to provide the unintended consequence that the newly thawed cells were not as fit and or virulent as broth cultured bacteria. At necropsy, the gross pathology displayed little signs of disease.

The drug was able to provide an apparent benefit in the short term, however no benefit was observed at week 3 and beyond relative to the vehicle control. However since none of the rabbits cavitated in group 1, an assessment of the drugs effect on preventing cavitation could not be determined.

In the second study the rabbits did develop cavitary lesions. Lesions had developed in all groups but the volume and number of cavities were lower in the RO32-3555 treated animals. Treatment of rabbits with the RO32-3555 inhibitor alone was not sufficient to prevent cavitation, however use of the drug as part of antibiotic containing drug regimen may prove useful.

The breakdown of the extracellular matrix requires the activity of special enzymes of the matrix metalloproteinase class. Cellular necrosis is not sufficient to break down the extracellular matrix. Cavitary lesion development has been classically described as the result of a granuloma that undergoes central necrosis. While we do not refute that necrosis is a necessary event that does occur during cavitary lesion development, we believe that the enzymatic breakdown of the extracellular matrix is also required.

References

1. World Health Organization (2013). Global tuberculosis report 2013.

2. Barry, C. E., Boshoff, H. I., Dartois, V., Dick, T., Ehrt, S., Flynn, J. L., Schnappinger, D., Wilkinson, R. J., and Young, D. (2009). The spectrum of latent tuberculosis: rethinking the biology and intervention strategies. Nat Rev Microbiol *7*, 845–855.

3. Paige, C., and Bishai, W. R. (2010). Penitentiary or penthouse condo: the tuberculous granuloma from the microbe's point of view. Cell Microbiol *12*, 301–309.

4. Davis, J. M., Clay, H., Lewis, J. L., Ghori, N., Herbomel, P., and Ramakrishnan, L. (2002). Real-time visualization of mycobacterium-macrophage interactions leading to initiation of granuloma formation in zebrafish embryos. Immunity *17*, 693–702.

5. Davis, J. M., and Ramakrishnan, L. (2009). The role of the granuloma in expansion and dissemination of early tuberculous infection. Cell *136*, 37–49.

6. Flynn, J. L., and Chan, J. (2001). Immunology of tuberculosis. Annu Rev Immunol *19*, 93–129.

7. Roca, F. J., and Ramakrishnan, L. (2013). TNF dually mediates resistance and susceptibility to mycobacteria via mitochondrial reactive oxygen species. Cell *153*, 521–534.

8. Lin, P. L., Myers, A., Smith, L., Bigbee, C., Bigbee, M., Fuhrman, C., Grieser, H., Chiosea, I., Voitenek, N. N., Capuano, S. V., et al. (2010). Tumor necrosis factor neutralization results in disseminated disease in acute and latent Mycobacterium tuberculosis infection with normal granuloma structure in a cynomolgus macaque model. Arthritis Rheum *62*, 340–350.

9. Bigbee, C. L., Gonchoroff, D. G., Vratsanos, G., Nadler, S. G., Haggerty, H. G., and Flynn, J. L. (2007). Abatacept treatment does not exacerbate chronic Mycobacterium tuberculosis infection in mice. Arthritis Rheum *56*, 2557–2565.

10. Skerry, C., Harper, J., Klunk, M., Bishai, W. R., and Jain, S. K. (2012). Adjunctive TNF inhibition with standard treatment enhances bacterial clearance in a murine model of necrotic TB granulomas. PLoS ONE *7*, e39680.

11. Dannenberg, A. M. (2009). Liquefaction and cavity formation in pulmonary TB: a simple method in rabbit skin to test inhibitors. Tuberculosis (Edinb)

89, 243–247.

12. Walker, N. F., Clark, S. O., Oni, T., Andreu, N., Tezera, L., Singh, S., Saraiva, L., Pedersen, B., Kelly, D. L., Tree, J. A., et al. (2012). Doxycycline and HIV infection suppress tuberculosis-induced matrix metalloproteinases. Am J Respir Crit Care Med *185*, 989–997.

13. Tadokera, R., Meintjes, G. A., Wilkinson, K. A., Skolimowska, K. H., Walker, N., Friedland, J. S., Maartens, G., Elkington, P. T. G., and Wilkinson, R. J. (2013). Matrix metalloproteinases and tissue damage in HIV-tuberculosis immune reconstitution inflammatory syndrome. Eur J Immunol.

14. Kesavan, A. K., Mendez, S. E., Hatem, C. L., Lopez-Molina, J., Aird, K., Pitt, M. L. M., Dannenberg, A. M., and Manabe, Y. C. (2005). Effects of dexamethasone and transient malnutrition on rabbits infected with aerosolized Mycobacterium tuberculosis CDC1551. Infect Immun *73*, 7056–7060.

15. Hunter, R. L. (2011). Pathology of post primary tuberculosis of the lung: An illustrated critical review. Tuberculosis (Edinb).

16. Ugarte-Gil, C. A., Elkington, P., Gilman, R. H., Coronel, J., Tezera, L. B., Bernabe-Ortiz, A., Gotuzzo, E., Friedland, J. S., and Moore, D. A. J. (2013). Induced sputum MMP-1, -3 & -8 concentrations during treatment of tuberculosis. PLoS ONE *8*, e61333.

17. Elkington, P., Shiomi, T., Breen, R., Nuttall, R. K., Ugarte-Gil, C. A., Walker, N. F., Saraiva, L., Pedersen, B., Mauri, F., Lipman, M., et al. (2011). MMP-1 drives immunopathology in human tuberculosis and transgenic mice. J. Clin. Invest. *121*, 1827–1833.

18. Elkington, P. T., D'Armiento, J. M., and Friedland, J. S. (2011). Tuberculosis immunopathology: the neglected role of extracellular matrix destruction. Science Translational Medicine *3*, 71ps6–71ps6.

19. Singla, R., Srinath, D., Gupta, S., Visalakshi, P., Khalid, U. K., Singla, N., Gupta, U. A., Bharty, S. K., and Behera, D. (2009). Risk factors for new pulmonary tuberculosis patients failing treatment under the Revised National Tuberculosis Control Programme, India. Int J Tuberc Lung Dis *13*, 521–526.

20. Benator, D., Bhattacharya, M., Bozeman, L., Burman, W., Cantazaro, A., Chaisson, R., Gordin, F., Horsburgh, C. R., Horton, J., Khan, A., et al. (2002). Rifapentine and isoniazid once a week versus rifampicin and isoniazid twice a week for treatment of drug-susceptible pulmonary tuberculosis in HIV-negative patients: a randomised clinical trial. Lancet *360*, 528–534.

21. Palaci, M., Dietze, R., Hadad, D. J., Ribeiro, F. K. C., Peres, R. L., Vinhas, S. A., Maciel, E. L. N., do Valle Dettoni, V., Horter, L., Boom, W. H., et al. (2007). Cavitary disease and quantitative sputum bacillary load in cases of pulmonary tuberculosis. Journal of Clinical Microbiology *45*, 4064–4066.

22. Long, R., Maycher, B., Dhar, A., Manfreda, J., Hershfield, E., and Anthonisen, N. (1998). Pulmonary tuberculosis treated with directly observed therapy: serial changes in lung structure and function. Chest *113*, 933–943.

23. Lee, J.-J., Chong, P.-Y., Lin, C.-B., Hsu, A.-H., and Lee, C.-C. (2008). High resolution chest CT in patients with pulmonary tuberculosis: characteristic findings before and after antituberculous therapy. Eur J Radiol *67*, 100–104.

24. Price, A. P., England, K. A., Matson, A. M., Blazar, B. R., and Panoskaltsis-Mortari, A. (2010). Development of a decellularized lung bioreactor system for bioengineering the lung: the matrix reloaded. Tissue Eng Part A *16*, 2581–2591.

25. Greenlee, K. J., Werb, Z., and Kheradmand, F. (2007). Matrix metalloproteinases in lung: multiple, multifarious, and multifaceted. Physiol. Rev. *87*, 69–98.

26. Hemmings, F. J., Farhan, M., Rowland, J., Banken, L., and Jain, R. (2001). Tolerability and pharmacokinetics of the collagenase-selective inhibitor Trocade in patients with rheumatoid arthritis. Rheumatology (Oxford) *40*, 537–543.

Figures

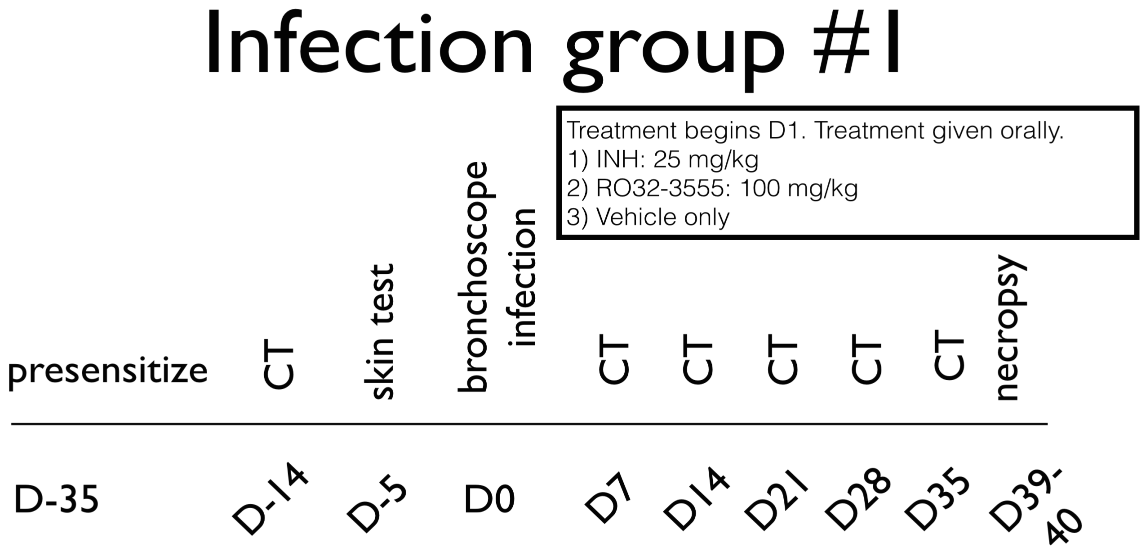

Figure 4-1: Group 1 study outline

Rabbits were presensitized prior to infection. Rabbits underwent a series of 5 subcutaneous sensitization injections of 10^8 heat killed bacilli in Freund's incomplete adjuvant. Following infection rabbits were treated daily with INH, RO32-3555, or vehicle alone. Rabbits underwent weekly set pressure CT scans and were necropsied at the end of the study.

Figure 4-2: Group 1 CT density plots

Rabbits underwent weekly CT breath hold scans at 20 cm water pressure. Total lung regions were first segmented and then a global threshold of -200:200 HU was applied to define the pathological region of interest. This threshold selects dense tissue which is associated with disease. A) Preinfection scan shows no difference between groups. B) INH treated rabbits show less lung consolidation as compared to the vehicle group ($p<0.01$). C) Both the INH and RO32-3555 treated groups show significantly less lung consolidation as compared to the vehicle control group ($p<0.001$). D) INH shows significantly less lung consolidation as compared to vehicle and RO32-3555 groups. E) RO32-3555 animals show the greatest amount of lung consolidation ($p<0.001$). F) INH treated animals show the lowest amount of lung consolidation and RO32-3555 animals show the greatest amount of lung consolidation ($p<0.001$).

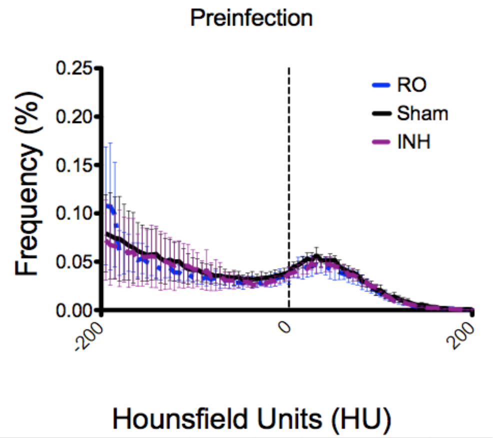

Tukey's Multiple Comparison Test	Mean Diff.	q	Significant? P < 0.05?	Summary
Sham vs INH	0.002854	1.235	No	ns
Sham vs RO	0.003563	1.542	No	ns
INH vs RO	0.0007095	0.3070	No	ns

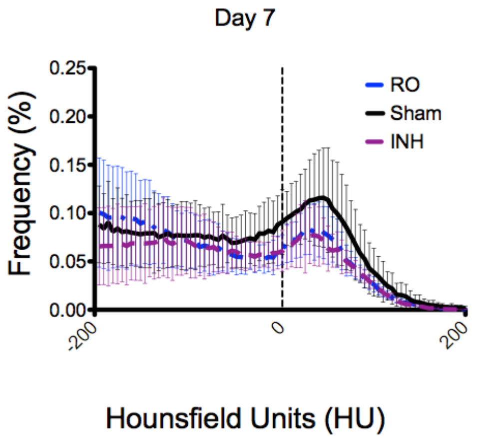

Tukey's Multiple Comparison Test	Mean Diff.	q	Significant? P < 0.05?	Summary
Sham vs INH	0.01594	4.627	Yes	**
Sham vs RO	0.01024	2.972	No	ns
INH vs RO	-0.005701	1.655	No	ns

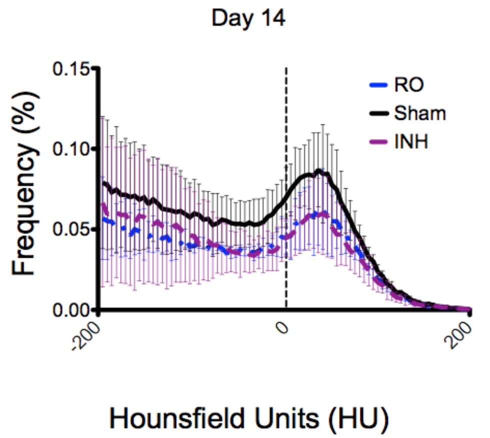

Tukey's Multiple Comparison Test	Mean Diff.	q	Significant? P < 0.05?	Summary
Sham vs INH	0.01325	5.277	Yes	***
Sham vs RO	0.01447	5.761	Yes	***
INH vs RO	0.001217	0.4845	No	ns

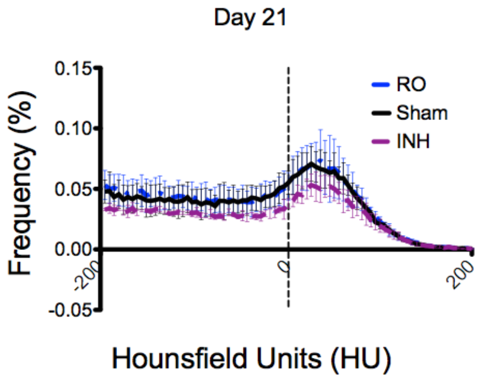

Tukey's Multiple Comparison Test	Mean Diff.	q	Significant? P < 0.05?	Summary
Sham vs INH	0.008971	4.330	Yes	**
Sham vs RO	-0.001714	0.8272	No	ns
INH vs RO	-0.01069	5.157	Yes	**

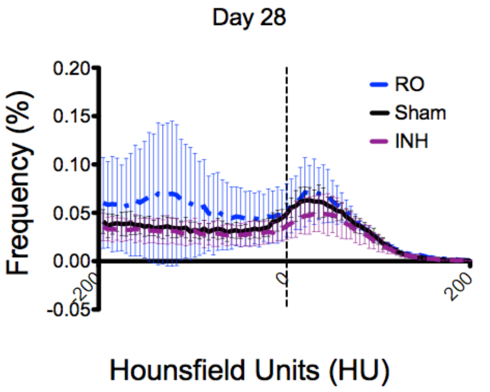

Tukey's Multiple Comparison Test	Mean Diff.	q	Significant? P < 0.05?	Summary
Sham vs INH	0.004975	2.380	No	ns
Sham vs RO	-0.01145	5.479	Yes	***
INH vs RO	-0.01643	7.858	Yes	***

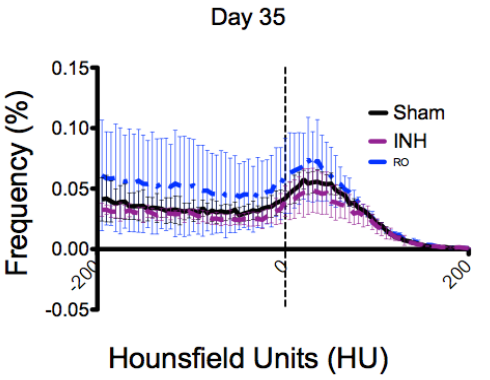

Tukey's Multiple Comparison Test	Mean Diff.	q	Significant? P < 0.05?	Summary
Sham vs INH	0.004530	2.335	No	ns
Sham vs RO	-0.01112	5.734	Yes	***
INH vs RO	-0.01565	8.069	Yes	***

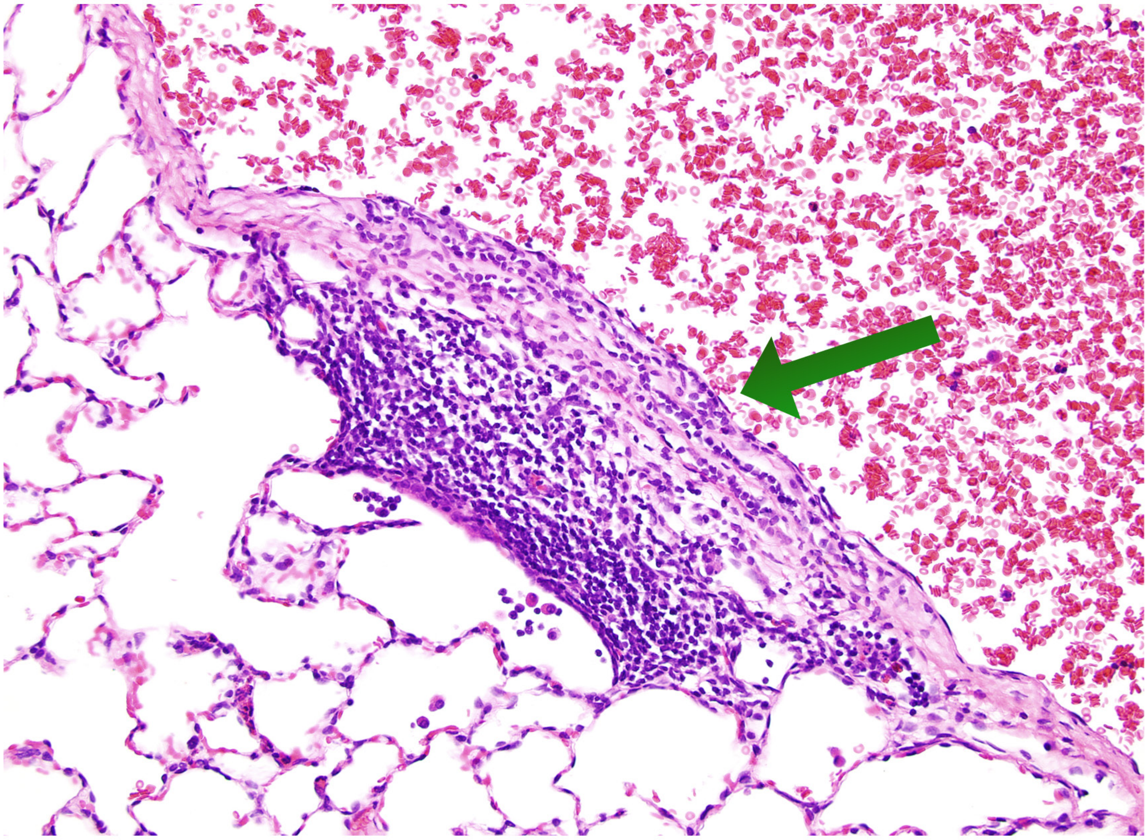

Figure 4-3: Vasculitis

The presence of vasculitis was observed in the RO32-3555 treatment group. Vasculitis had not been previously reported as a side effect of the drug. Further studies are needed to determine the effect of RO32-3555 on vasculitis in animals infected with tuberculosis.

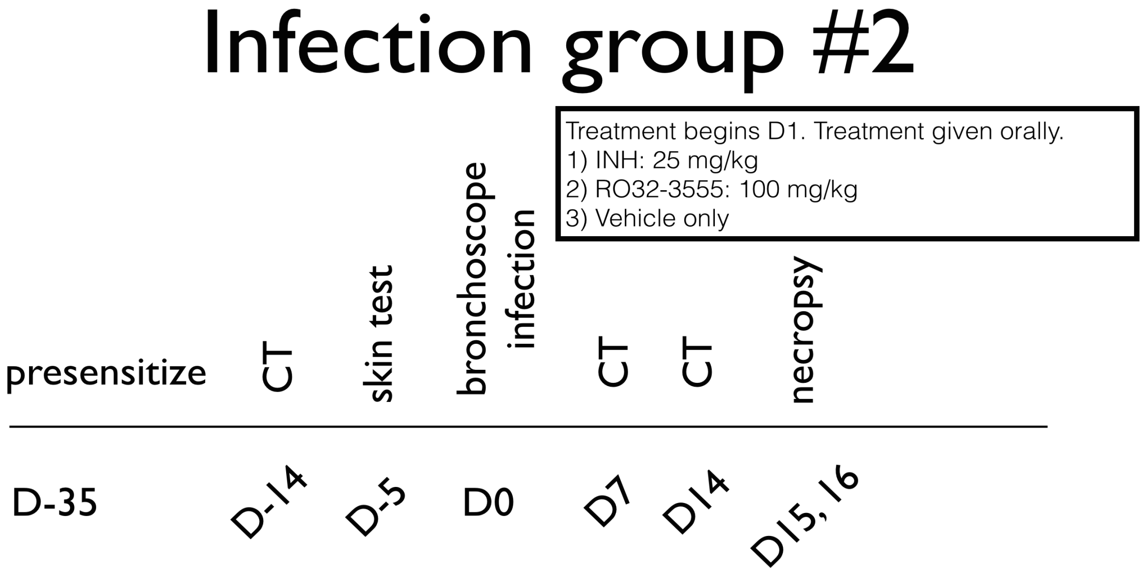

Treatment begins D1. Treatment given orally.
1) INH: 25 mg/kg
2) RO32-3555: 100 mg/kg
3) Vehicle only

Figure 4-4: Group 2 study outline

Rabbits were presensitized prior to infection. Rabbits underwent a series of 5 subcutaneous sensitization injections of 10^8 heat killed bacilli in Freund's incomplete adjuvant. Following infection rabbits were treated daily with INH, RO32-3555, or vehicle alone. Rabbits underwent weekly set pressure CT scans and were necropsied at the end of the study. Rabbits were only monitored for 2 weeks unlike the first infection group which was monitored for 5 weeks postinfection.

Figure 4-5: Group 2, 3D lung images

Rabbits underwent weekly set pressure CT scans. The lungs were inflated to a set pressure of 20 cm water to reduce the amount of breathing artifact. Animals were infected by bronchoscopy and the bacterial suspension was localized to single lung lobe. Cavities are indicated with red arrows. Cavities and signs of disease were present in all treatment groups.

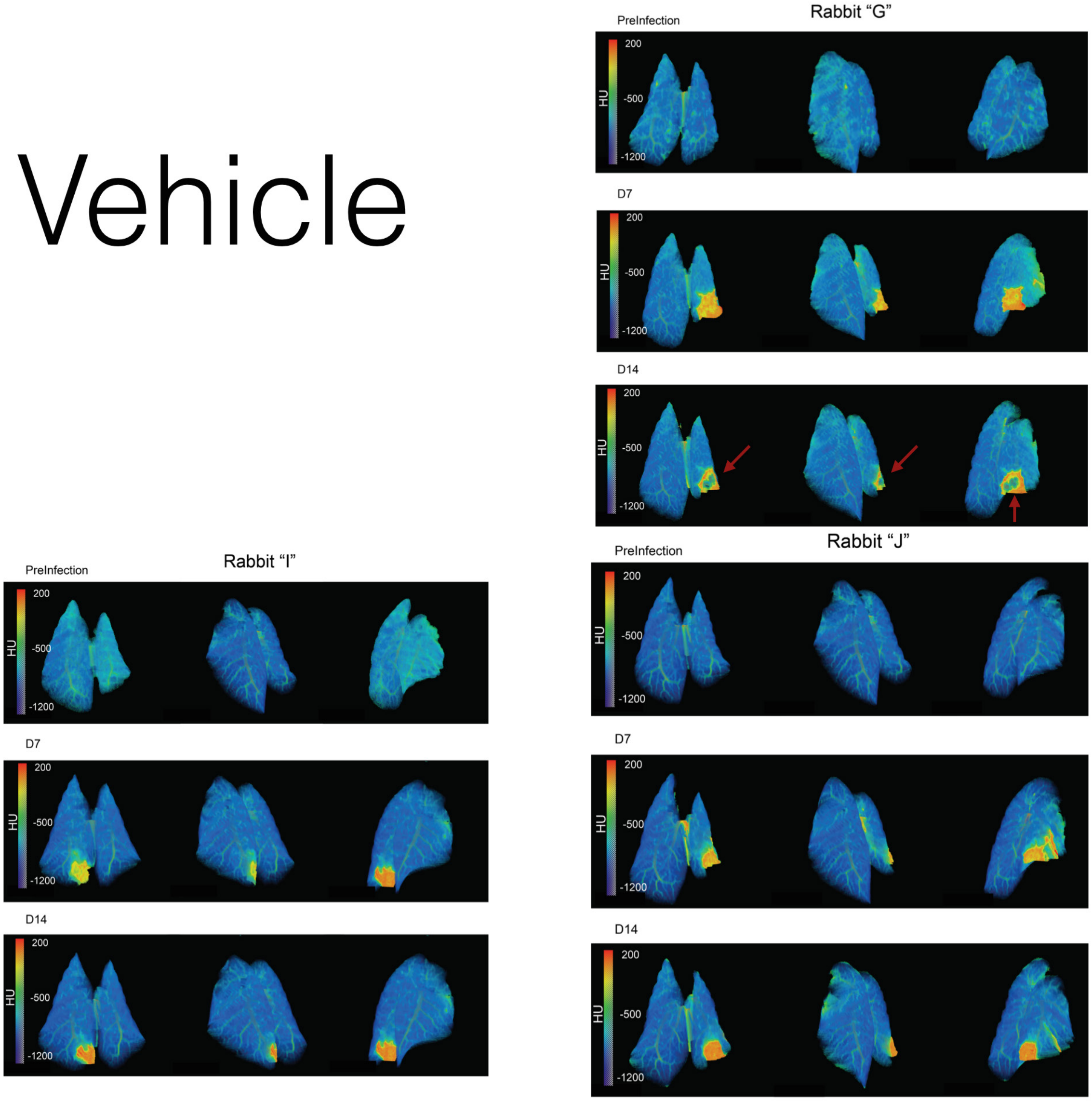

INH

Rabbit “E”

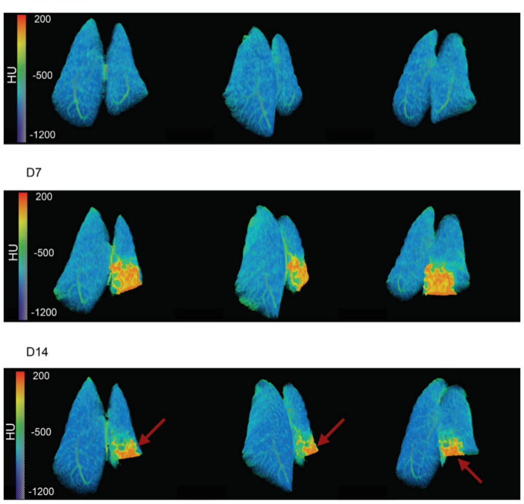

Rabbit “F”

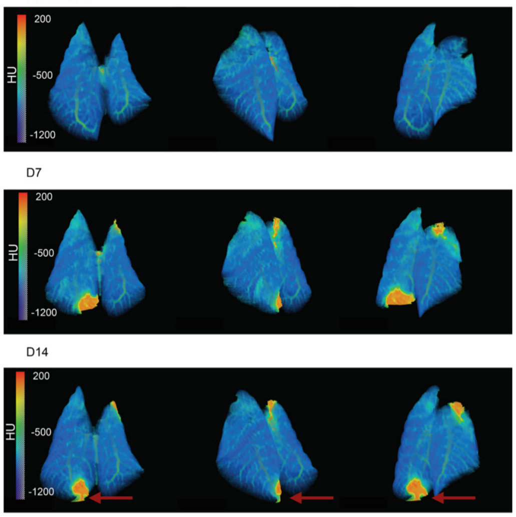

Rabbit “H”

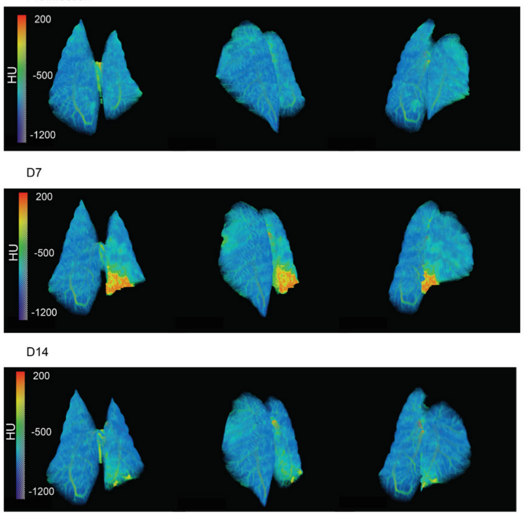

RO32-3555

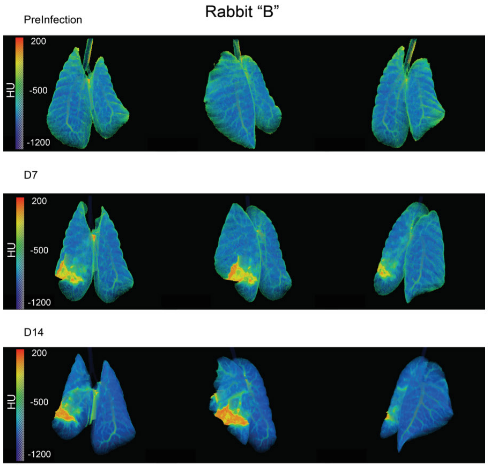
Rabbit “B”

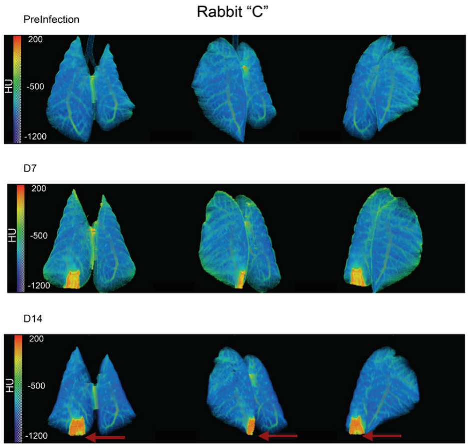
Rabbit “C”

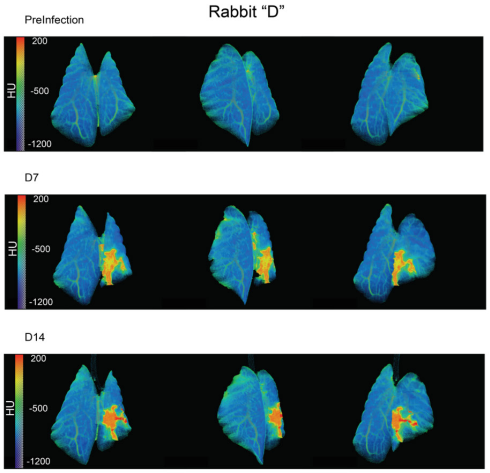
Rabbit “D”

Figure 4-6: Group 2 CT density plots

Rabbits underwent weekly CT breath hold scans at 20 cm water pressure. Total lung regions were first segmented and then a global threshold of -200:200 HU was applied to define the pathological region of interest. This threshold selects dense tissue which is associated with disease. A) Preinfection scan shows no difference between groups. B) No significant difference was observed between any treatment group at day 7 postinfection. C) The RO32-3555 treatment group showed the greatest amount of lung consolidation as compared to the vehicle and INH treatment groups respectively ($p<0.01$ and $p<0.001$).

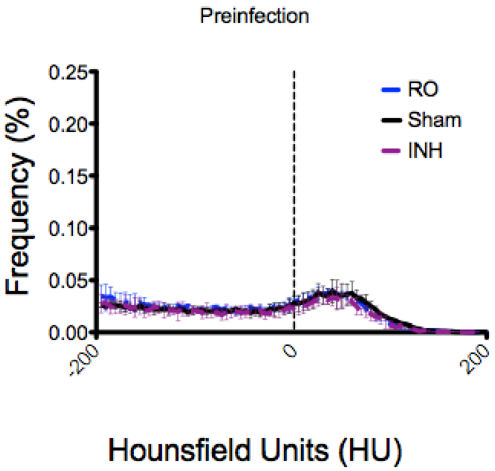

Tukey's Multiple Comparison Test	Mean Diff.	q	Significant? P < 0.05?
Sham vs INH	0.002125	1.724	No
Sham vs RO	-0.001169	0.9486	No
INH vs RO	-0.003293	2.673	No

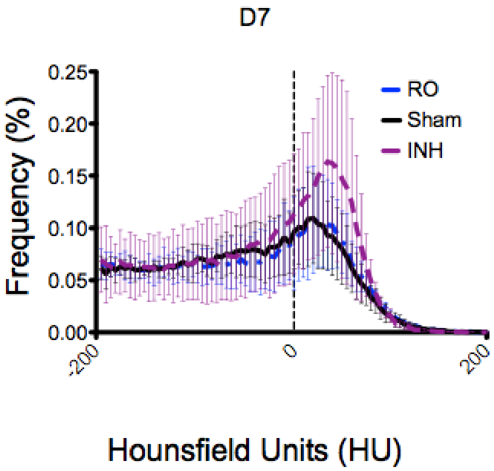

Tukey's Multiple Comparison Test	Mean Diff.	q	Significant? P < 0.05?
Sham vs INH	-0.01061	2.501	No
Sham vs RO	0.0007882	0.1857	No
INH vs RO	0.01140	2.686	No

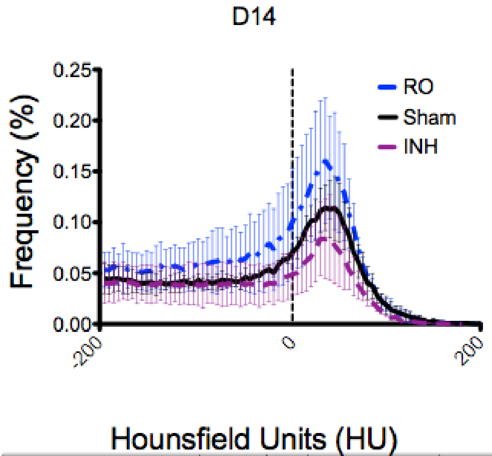

Tukey's Multiple Comparison Test	Mean Diff.	q	Significant? P < 0.05?	Summary
Sham vs INH	0.009303	2.522	No	ns
Sham vs RO	-0.01469	3.982	Yes	*
INH vs RO	-0.02399	6.504	Yes	***

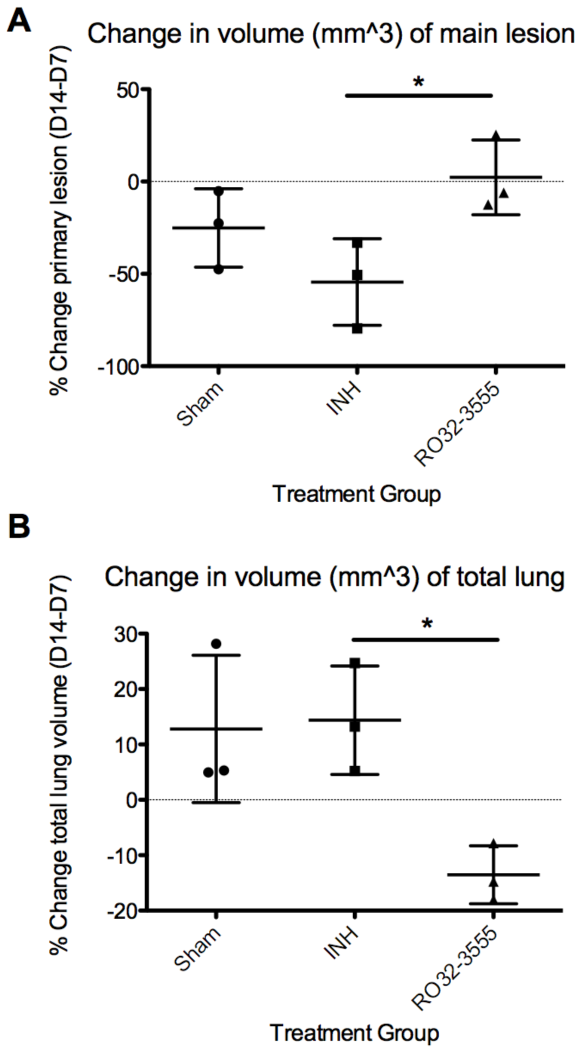

Figure 4-7: Group 2 lung and lesion volume

Changes in the volume of the main lesion (as defined by -200:200 HU threshold) and the total lung were measured. Healthy lung tissue should expand when inflated at 20 cm water, however the consolidated tissue has a decreased ability to expand. There was an inverse relationship between the change in volume of the A) main lesion and B) total lung.

Table 4-1: Cavity stats

The number of cavities and cavity volume were measured by CT. The size and frequency of cavities was less in the RO32-3555 treatment group.

	Vehicle (mm^3)	INH (mm^3)	RO32-3555 (mm^3)
Rabbit 1	381 (2 coalescing)	225; 75; 25	9
Rabbit 2	caseum	35	0
Rabbit 3	caseum	0	0

Appendix- Image processing of CT and PET images

Abstract

Image data sets from different modalities, PET and CT, were acquired on separate instruments with different spatial resolutions. PET image data sets were reconstructed at a resolution at 1 x 1 x 1 mm voxels; CT image data sets are reconstructed at 0.3 x 0.3 x 0.625 mm voxels. The data sets therefore have different spatial resolutions and additionally have different spatial coordinates. Differences in voxel size across data sets and also differences in spatial coordinates need to be resolved for successful image analysis. Following image coregistration, segmentation of the lungs and the associated disease pathology is a semi-automated process that requires user input and guidance of the image processing software.

Introduction

A general list of reference terms relating to image processing are summarized in **Table 1-1**. Images must be carefully coregistered and segmented for accurate image analysis. Data from [^{18}F]-FDG PET scans provide functional data in which high uptake of the tracer results in a positive signal. In the context of infectious disease, the positive signal is likely attributed to the accumulation of the host immune cells at the site of an infection. Similarly, in the context of cancer, a positive signal is likely due to the accumulation of cancer cells. PET images provide good functional data but lack adequate anatomical information. Therefore it is almost always necessary to coregister a PET data set with an image data set which provides good anatomical information such as CT or MRI. Two methods are described for coregistration and segmentation. The first method uses freely available software tools and the second method uses the commercially available Amira Imaging software tool (Visualization Sciences Group).

Method 1- Annotation tool (NIH)

Use of the annotation tool requires preprocessing of the input PET and CT images. Preprocessing is required for coregistration and also to make the voxel size uniform between PET and CT image sets **(Figure 5-1, 5-2)**. These preprocessing steps are not required for use of Method 2 which makes use of the commercially available Amira Imaging software.

1. Load PET and CT data into AMIDE [1].
2. Coregistration
    - 2.1. Point sources were fastened to the animal to aid in image coregistration. 2-5 μCi of PET tracer was added to PCR tubes for use as point sources. The PCR tubes can be identified by CT and the radioactive tracer can be identified by PET **(Figure 5-3)**.

2.2. Coregistration was done using the using the “Alignment Wizard” under “Tools” → “Alignment Wizard” → “Fiduciary Markers”. The CT data stays fixed as the reference data set and the PET data is transformed for the coregistration process.

2.3. Coregistered data sets are exported by “File” → “Export Data Sets” → “Resliced Orientation” → “Analyze SPM” → “Bounding Box Inclusive of all data sets”.

2.4. Data sets are coregistered but still contain voxel sizes of different dimensions.

3. Normalization of voxel size using FIJI **(Figure 5-4)** [2].

3.1. Coregistered PET and CT data is first loaded into FIJI image processing software.

3.2. If “a” = CT and “b”= PET, then the following operations are performed by “Process” → “Math” → “add...” (or subtract as needed):

3.2.1. $a + b = c$

3.2.2. $c - a = b'$; where $b'$is the PET data but now has equivalent voxel dimensions as the CT image set.

4. Segmentation

4.1. The Annotation Tool (NIH) allows for semi-automated segmentation of images and was developed by the Mollura lab at the NIH. This tool is planned to be freely distributed, but at the time of writing the tool was still under development for general release.

4.2. Segmentation can be performed by a combination of tools available through the software platform such as thresholding or assisted region growing.

    4.2.1. Thresholding is done by selecting a density range and all voxels that fall between these defined regions are selected **(Figure 5-5)**.

    4.2.2. Assisted region walking consists of 2 labeling steps. First, seed points are selected in which the user selects representative regions that should be included in the region of interest. Next the user selects several seed points that are representative of regions that should not be included in the region of interest **(Figure 5-6)**.

4.3. After successful segmentation of the lung, the binary mask is exported. The binary mask can then be loaded into FIJI along with the coregistered PET and CT data sets.

4.4. The final step of segmentation is completed by multiplying the binary mask and the PET or CT data set of interest by “Process” → “Math” → “multiply...” **(Figure 5-7)**.

5. Histogram plots

    5.1. Load lung masks into FIJI

    5.2. “Analyze” → “Histogram”

Method 2: Amira Visualization Sciences Group

Use of the Amira software package does not require the use of any additional software for image processing. No additional steps are needed for normalization of voxel sizes between different image data sets. Amira is also capable of image coregistration and segmentation.

1. Load PET and CT data into AMIRA.
2. Coregistration
    - 2.1. PET and CT files are manually coregistered in the "multi planer viewer". Point sources are identified in the PET and CT viewers. Unlike in AMIDE, the point sources are not labeled with fiducial markers (**Figure 5-8, 5-9)**.
    - 2.2. Selection of the "transform editor options" and "manual registration tool" allows for manipulation of the "overlay data set" in relation to the primary data set **(Figure 5-10, 5-11).**
3. Segmentation
    - 3.1. Segmentation is performed using the "Segmentation editor". Amira organizes the segmentation process into 2 levels. The first level is known as the "label" class. Multiple segmentations can be made and saved under a "label" and these are known as "materials". For example a "label" can be named **LUNG** and examples of possible "materials" are *lung, airway,* and *esophagus*. It is important to note

that voxels can only belong to a single “material” and a voxel cannot be included under multiple “materials”. It is necessary to first duplicate the original label that contains the segmented lung befor further segmentation of the lung is carried out. This can be accomplished from the “Tree view viewer” and using the right mouse click to “duplicate object”. Further lung segmentation should be done using the duplicated object.

3.2. The first step is to segment the entire lung; including both pathologic and non-pathologic tissue. A new label named *Lung* should be created. Segmentation should be performed using the CT data set **(Figure 5-12)**.

  3.2.1. The “lasso”, “brush”, “magic wand”, and “threshold” tools can all be used as needed. Generally a combination of all tools will be required for proper segmentation.

3.3. Duplicate the *Lung* label and use the copy for further lung segmentation.

  3.3.1. Pathologic lung segmentation can be done using a defined threshold scale. Consolidation was defined as -200:200 HU **(Figure 5-13).**

  3.3.2. The *Lung* label that was created using the CT as a template can then applied to the PET data set **(Figure 5-14)**. Pathologic segmentation of the PET data set was done using a threshold of the top 5% percentile of PET uptake.

4. Histogram Plots

    4.1. From the “Tree view viewer”, select the “label” of interest and select “measure” → “histogram” **(Figure 5-15)**.

    4.2. From the “histogram” window, select the appropriate “data” (PET or CT), the “label” to be applied, and lastly the specific “material” to be analyzed. Output files should be saved as “.csv” for later use (**Figure 5-16)**.

References

1. Loening, A. M., and Gambhir, S. S. (2003). AMIDE: a free software tool for multimodality medical image analysis. Mol Imaging *2*, 131–137.

2. Schindelin, J., Arganda-Carreras, I., Frise, E., Kaynig, V., Longair, M., Pietzsch, T., Preibisch, S., Rueden, C., Saalfeld, S., Schmid, B., et al. (2012). Fiji: an open-source platform for biological-image analysis. Nat Methods *9*, 676–682.

Figures

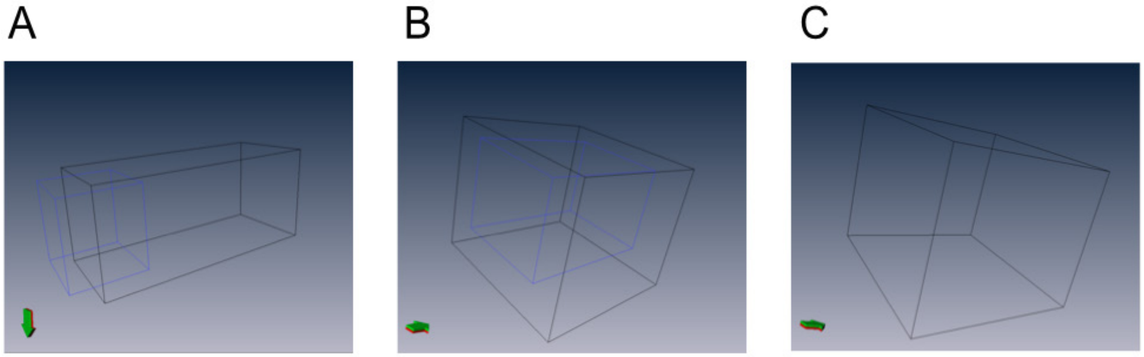

Figure 5-1: Image coregistration

Image preprocessing may be required for proper coregistration of images with different spatial size and spatial location. The wire bounding boxes represent the relative spatial size and location of the initial CT (black rectangle) and the PET (blue rectangle). A) The starting position of each respective data set prior to coregistration and normalization of voxel size. B) Transformation and coregistration of PET and CT data sets. C) Transformation and coregistration of PET and CT data sets after voxel size normalization between imaging sets.

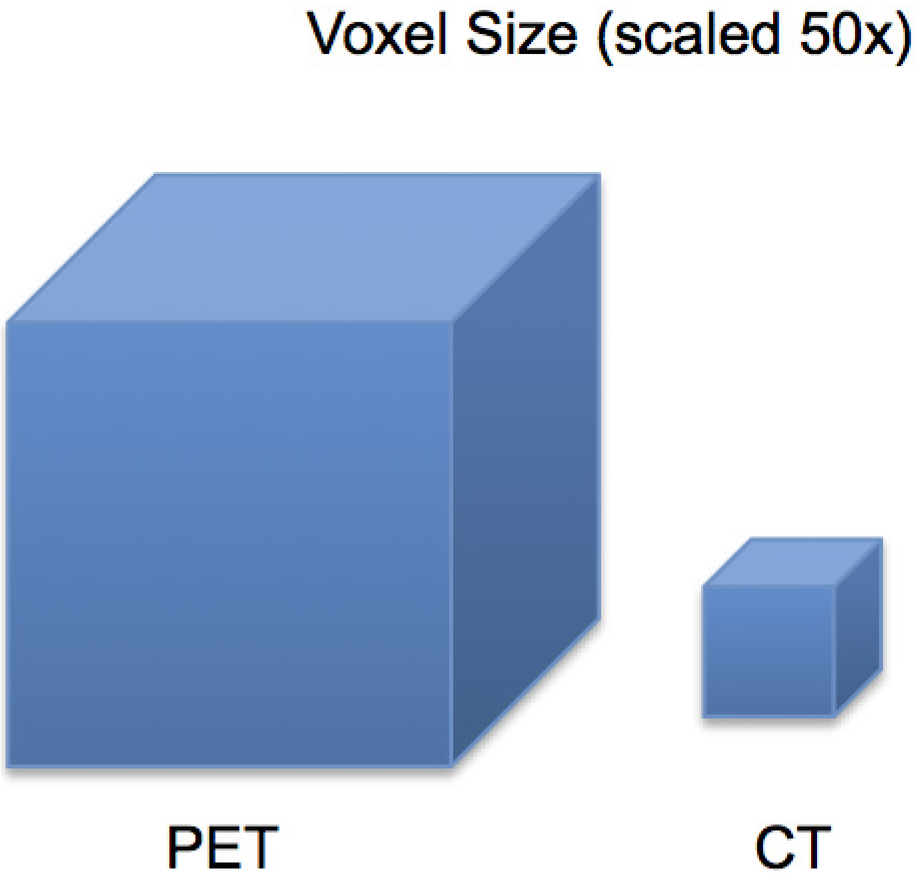

Figure 5-2: Voxel size

PET image data sets are reconstructed at a resolution of 1 x 1 x 1 mm voxel size. CT image data sets are reconstructed at a resolution of 0.3 x 0.3 x 0.625 mm voxel size. For proper coregistration of data sets to be used with the Method 1 data processing, preprocessing of the data sets is required to normalize voxel size between PET and CT data sets.

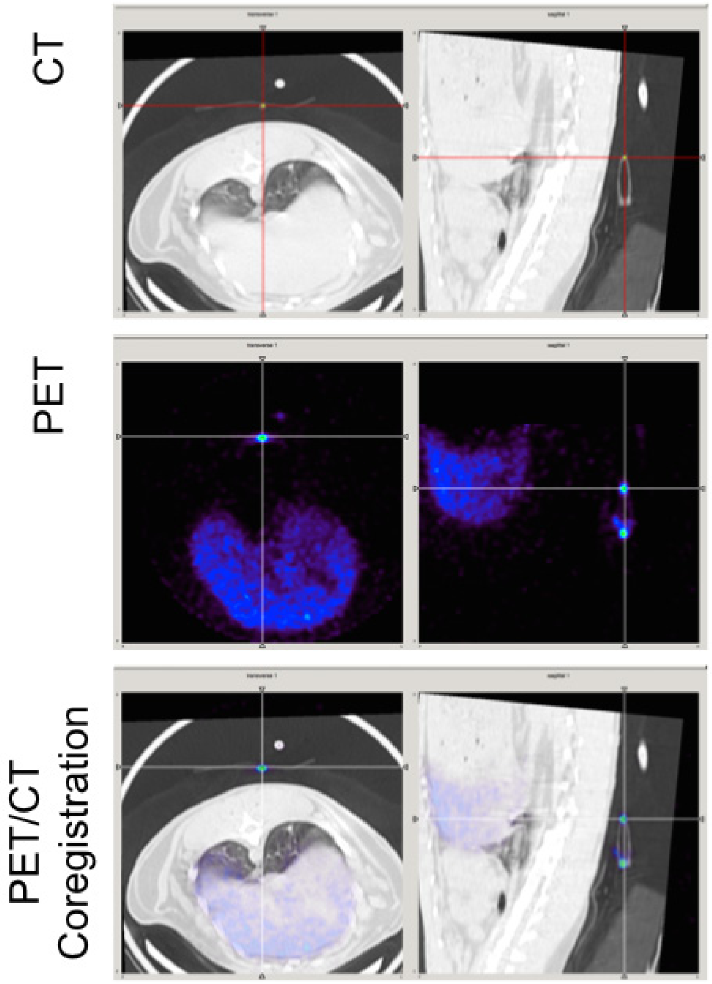

Figure 5-3: Point source coregistration

Point sources are used to for accurate coregistration of PET and CT image sets. PCR tubes filled with 2-5 µCi of [^{18}F]-FDG tracer were used as point sources. The PCR tube is identified and labeled with a fiducial mark using the AMIDE image processing software. The PET active tracer was labeled with a fiducial mark in the PET data set. Successful coregistration can be observed in the merged image. The liver shows high uptake of tracer as expected.

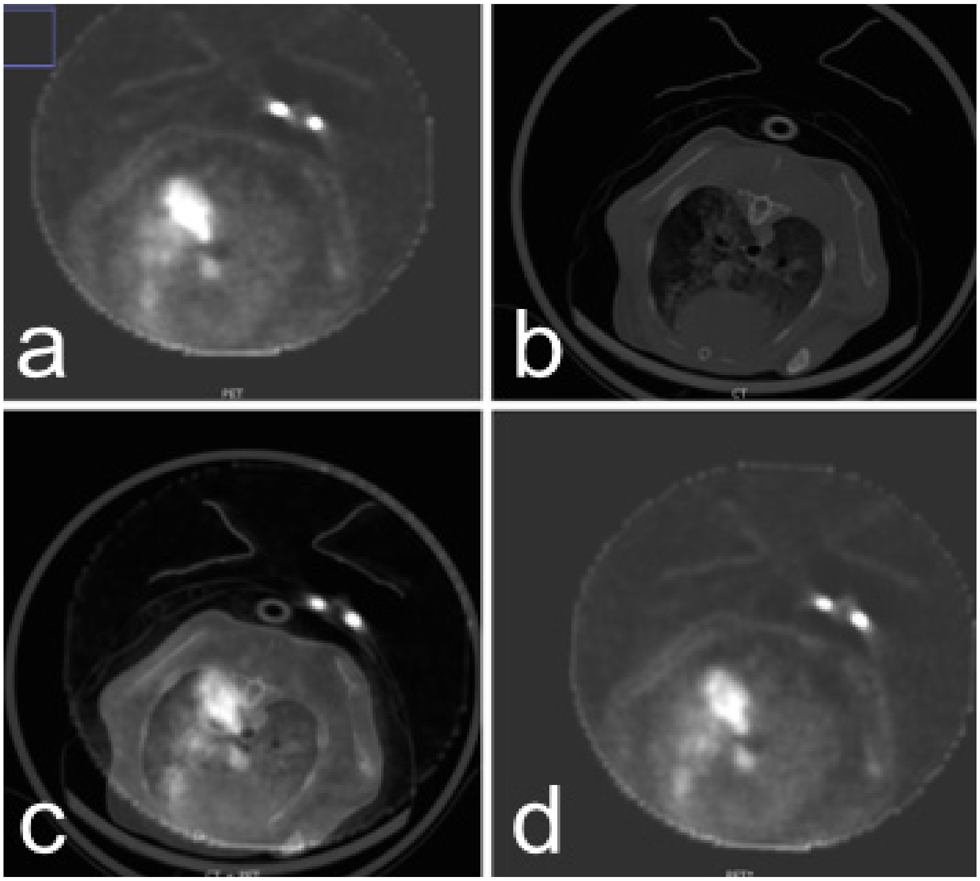

Figure 5-4: Voxel normalization

The PET data set is composed of larger voxels relative to the CT data set. It is necessary for some analysis platforms that both data sets are composed of the same sized voxels. Voxel size can be normalized using the math functions included in FIJI. “Process” → “Math” → “Add…” (or “Subtract…” as needed). *a*) coregistered PET. *b*) coregistered CT. *c*) sum of $a + b$. *d*) difference of $c - b$. The basic process can be summarized by the following equations: 1) $a + b = c$; 2) $c - b = d$.

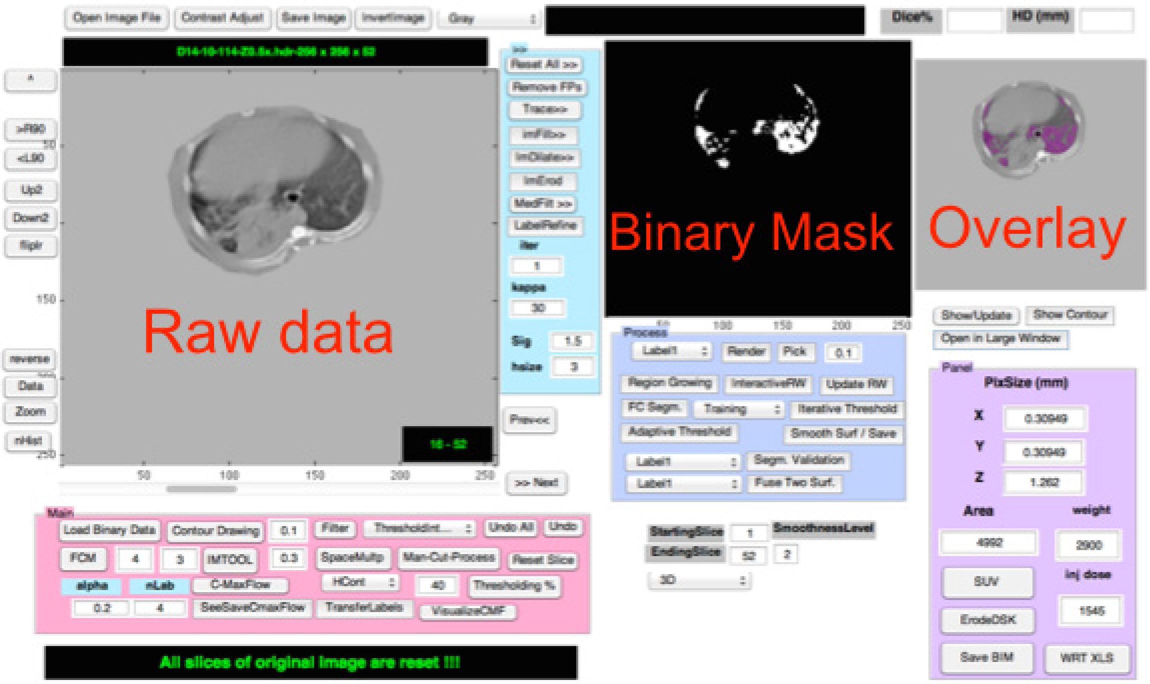

All slices of original image are reset !!!

Figure 5-5: Annotation tool threshold

Segmentation can be performed by thresholding. In this method, a density range is defined and all values within that range are selected. However as can be seen by the binary mask and overlay, not all parts of the lung are included. In general, thresholding will allow for the capture of pathologically uninvolved tissue, but will not allow for the inclusion of pathologically involved tissue. The density of pathologically involved lung tissue is similar to the density of surrounding muscle, fat, liver, or heart tissue. Selecting a threshold that will include pathologically involved tissue will also select some or all of the previously mentioned tissue types.

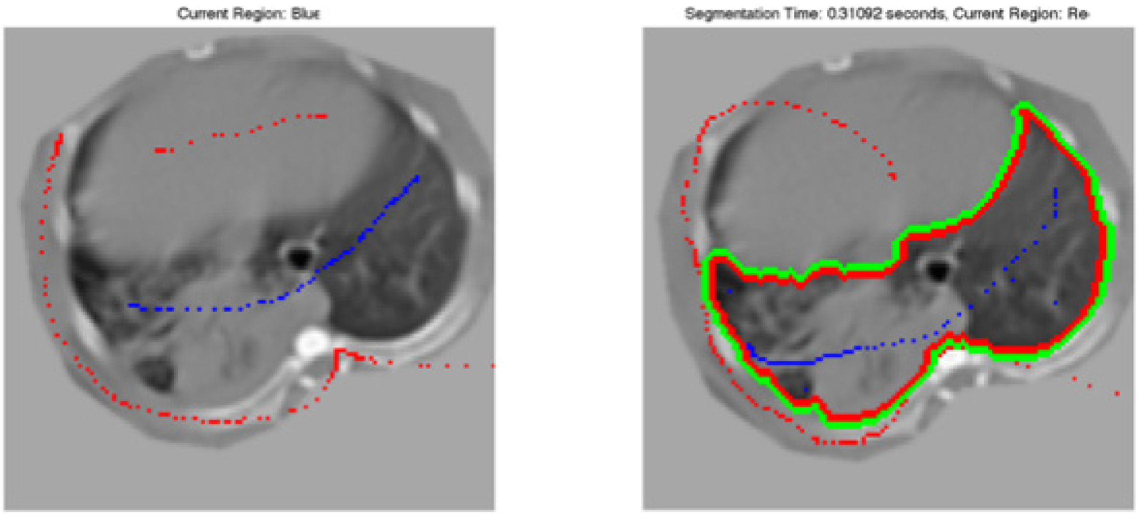

Figure 5-6: Annotation tool region walking

One of the more powerful options available is the trainable region walking method. In this segmentation method, the user selects seed points that represent regions to be included as denoted by the blue dots. The user then selects regions that are not to be included as represented by the red dots. The computer generated region of interest consists of the area bounded by the green and red boundaries. This segmentation method was successful in specifically capturing both pathologically involved and uninvolved lung.

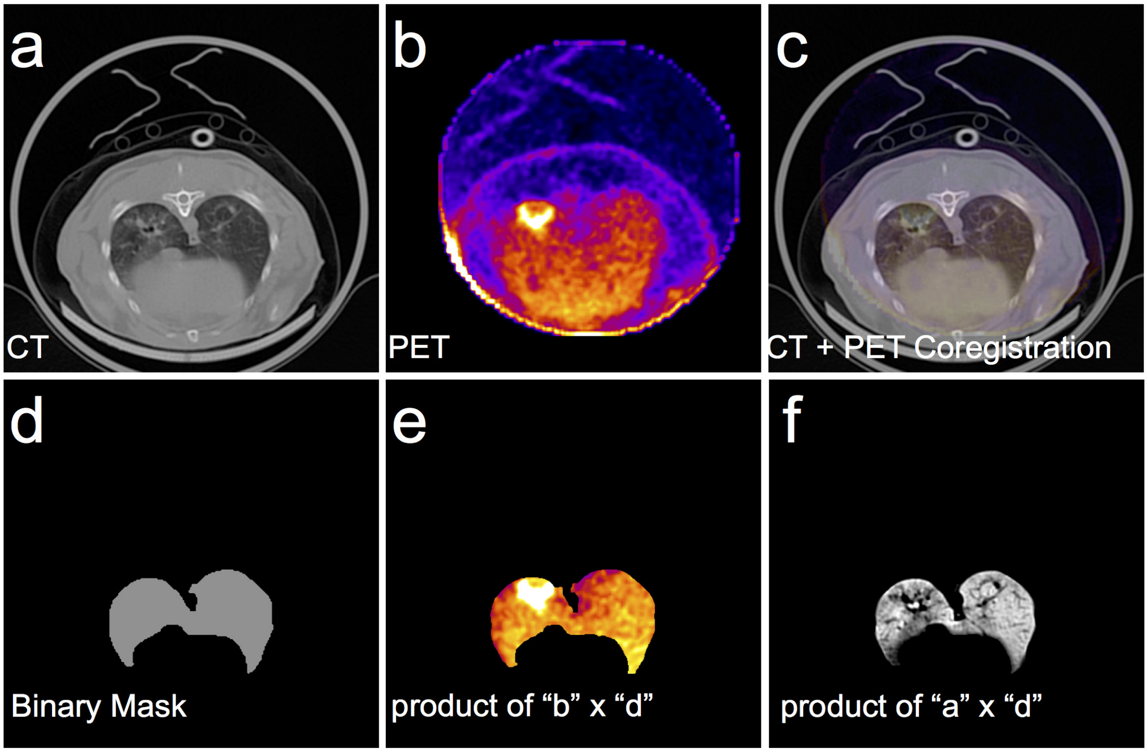

Figure 5-7: Annotation Tool final

A summary of the coregistration and segmentation process using Method 1. Raw data is loaded in AMIDE as represented in *a* and *b.* The coregistered images are shown in *c.* The resulting image data sets are then processed in FIJI to normalize voxel size across different imaging sets. The binary mask in *d* is generated with the Annotation Tool. Final segmented lungs are the result of applying the binary mask to the PET and CT data sets respectively as shown in *e* and *f.*

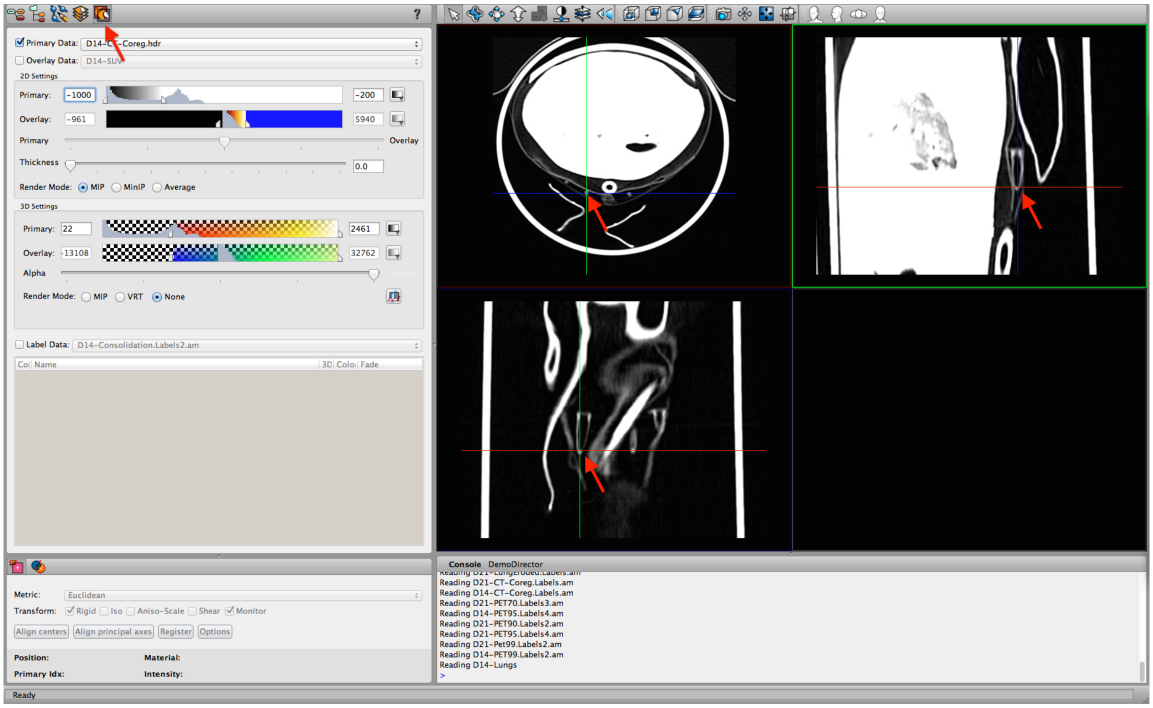

☑ Primary Data: D14-CT-Coreg.hdr

☐ Overlay Data: D14-SUV

2D Settings

Primary: -1000 -200

Overlay: -961 5940

Thickness 0.0

Render Mode: ● MIP ○ MinIP ○ Average

3D Settings

Primary: 22 2461

Overlay: -13108 32762

Render Mode: ○ MIP ○ VRT ● None

☐ Label Data: D14-Consolidation.Labels2.am

Metric: Euclidean

Transform: ☑ Rigid ☐ Iso ☐ Aniso-Scale ☐ Shear ☑ Monitor

```
Reading D21-CT-Coreg.Labels.am
Reading D14-CT-Coreg.Labels.am
Reading D21-PET70.Labels3.am
Reading D14-PET95.Labels4.am
Reading D21-PET90.Labels2.am
Reading D21-PET95.Labels4.am
Reading D21-Pet99.Labels2.am
Reading D14-PET99.Labels2.am
Reading D14-Lungs
>
```

Figure 5-8: Amira CT point source

PCR tubes filled 3 µCi of [^{18}F]-FDG tracer were used as point sources for coregistration of CT and PET images. Point sources can be identified in the CT view by adjusting the window to -1000:-200 HU. This window is not optimal for assessment of the lung pathology but it is sufficient for coregistration purposes.

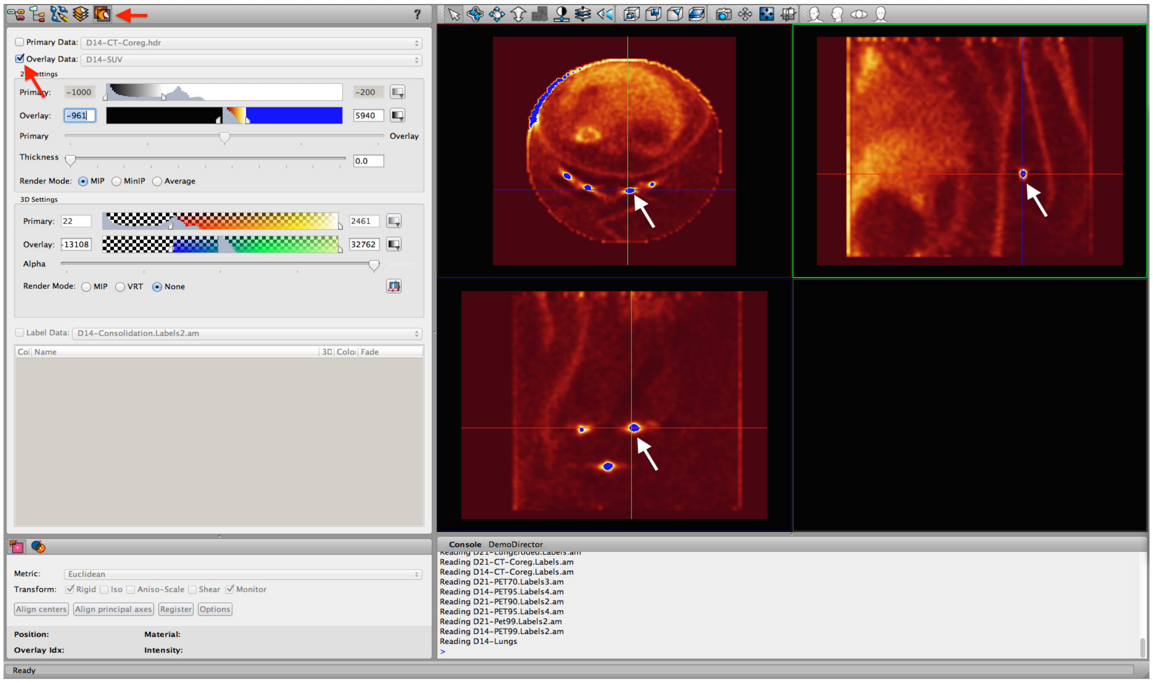

☐ Primary Data: D14-CT-Coreg.hdr

☑ Overlay Data: D14-SUV

2D Settings

Primary: -1000 -200

Overlay: -961 5940

Primary Overlay

Thickness 0.0

Render Mode: ● MIP ○ MinIP ○ Average

3D Settings

Primary: 22 2461

Overlay: -13108 32762

Alpha

Render Mode: ○ MIP ○ VRT ● None

☐ Label Data: D14-Consolidation.Labels2.am

Metric: Euclidean

Transform: ☑ Rigid ☐ Iso ☐ Aniso-Scale ☐ Shear ☑ Monitor

```
Reading D21-CT-Coreg.Labels.am
Reading D14-CT-Coreg.Labels.am
Reading D21-PET70.Labels3.am
Reading D14-PET95.Labels4.am
Reading D21-PET90.Labels2.am
Reading D21-PET95.Labels4.am
Reading D21-Pet99.Labels2.am
Reading D14-PET99.Labels2.am
Reading D14-Lungs
>
```

Figure 5-9: Amira PET point source

PCR tubes filled 3 μCi of [^{18}F]-FDG tracer were used as point sources for coregistration of CT and PET images. CT data is loaded into the “Primary Data” panel and PET data is loaded into the “Overlay Data” panel. Point sources can be identified in the PET view by adjusting the window to maximize the signal from the respective point sources.

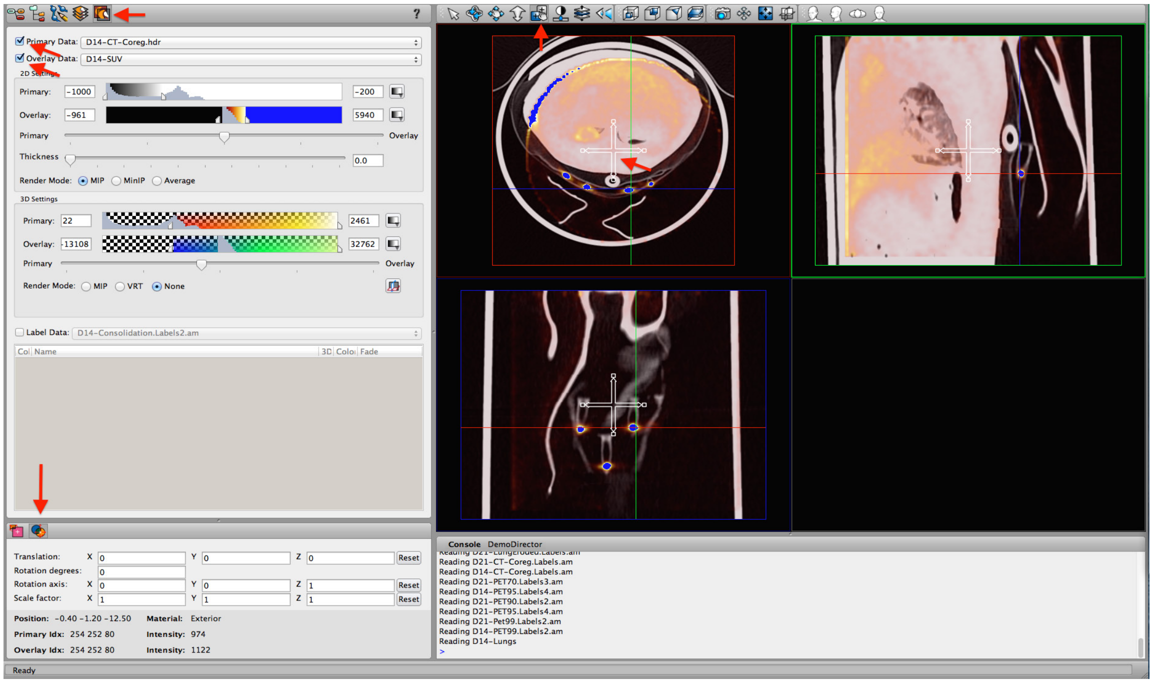

☑ Primary Data: D14-CT-Coreg.hdr

☑ Overlay Data: D14-SUV

2D Settings

Primary: -1000 -200

Overlay: -961 5940

Thickness 0.0

Render Mode: ● MIP ○ MinIP ○ Average

3D Settings

Primary: 22 2461

Overlay: -13108 32762

Render Mode: ○ MIP ○ VRT ● None

☐ Label Data: D14-Consolidation.Labels2.am

Translation: X 0 Y 0 Z 0

Rotation degrees: 0

Rotation axis: X 0 Y 0 Z 1

Scale factor: X 1 Y 1 Z 1

Position: -0.40 -1.20 -12.50 Material: Exterior

Primary Idx: 254 252 80 Intensity: 974

Overlay Idx: 254 252 80 Intensity: 1122

```
Reading D21-CT-Coreg.Labels.am
Reading D14-CT-Coreg.Labels.am
Reading D21-PET70.Labels3.am
Reading D14-PET95.Labels4.am
Reading D21-PET90.Labels2.am
Reading D21-PET95.Labels4.am
Reading D21-Pet99.Labels2.am
Reading D14-PET99.Labels2.am
Reading D14-Lungs
>
```

Figure 5-10: Amira coregistration

Manual coregistration can be done from the “Multi planer viewer”. Selection of the “Registration tool” from the top tool bar and the “Transform editor options” from the lower left corner allow for manual manipulation of the “overlay data” image set. The image set can be transformed in all 3 planes by manipulation of the white cross located in the center of each plane viewer.

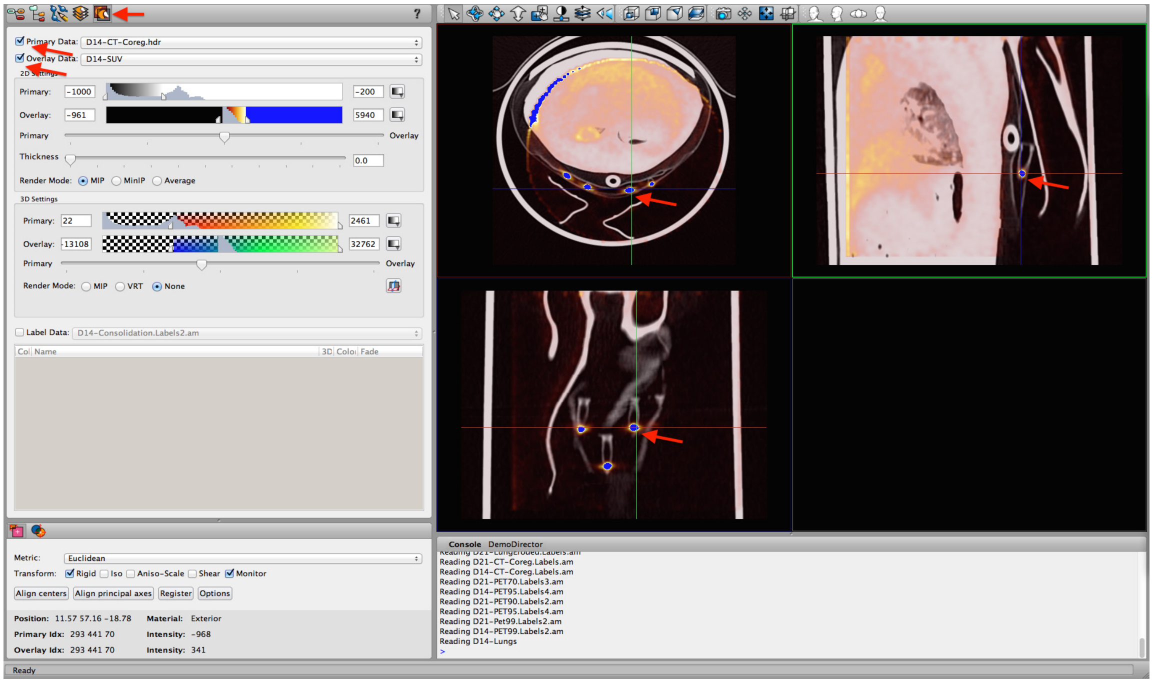

☑ Primary Data: D14-CT-Coreg.hdr
☑ Overlay Data: D14-SUV

2D Settings
Primary: -1000 … -200
Overlay: -961 … 5940
Primary … Overlay
Thickness 0.0
Render Mode: ● MIP ○ MinIP ○ Average

3D Settings
Primary: 22 … 2461
Overlay: -13108 … 32762
Primary … Overlay
Render Mode: ○ MIP ○ VRT ● None

☐ Label Data: D14-Consolidation.Labels2.am

Metric: Euclidean
Transform: ☑ Rigid ☐ Iso ☐ Aniso-Scale ☐ Shear ☑ Monitor

Position: 11.57 57.16 -18.78 Material: Exterior
Primary Idx: 293 441 70 Intensity: -968
Overlay Idx: 293 441 70 Intensity: 341

```
Reading D21-CT-Coreg.Labels.am
Reading D14-CT-Coreg.Labels.am
Reading D21-PET70.Labels3.am
Reading D14-PET95.Labels4.am
Reading D21-PET90.Labels2.am
Reading D21-PET95.Labels4.am
Reading D21-Pet99.Labels2.am
Reading D14-PET99.Labels2.am
Reading D14-Lungs
>
```

Ready

Figure 5-11: Amira coregistration overlay

Successful coregistration is visually confirmed by point source localization between both data sets. The signal from the point sources should be localized to the bottom of the PCR tubes.

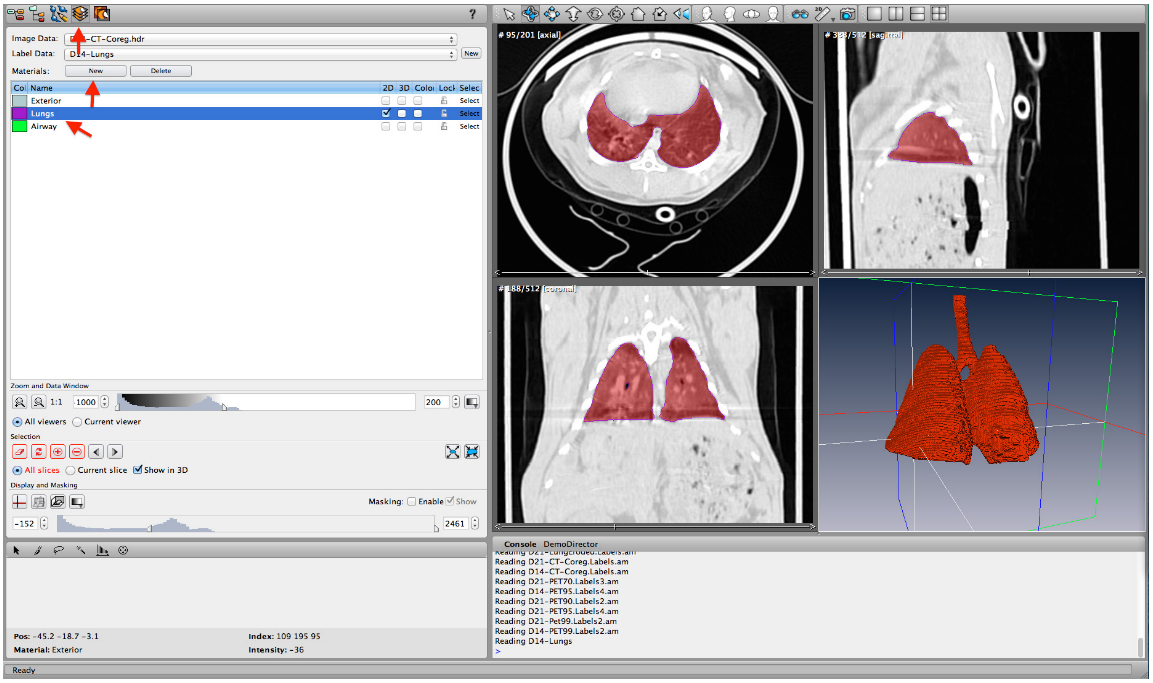

Image Data: CT-Coreg.hdr

Label Data: D14-Lungs

Materials: New Delete

Col	Name	2D	3D	Colo	Lock	Selec
	Exterior	☐	☐	☐		Select
	Lungs	☑	☐	☐		Select
	Airway	☐	☐	☐		Select

-1000 200

● All viewers ○ Current viewer

● All slices ○ Current slice ☑ Show in 3D

Masking: ☐ Enable ☑ Show

-152 2461

Pos: -45.2 -18.7 -3.1 **Index:** 109 195 95

Material: Exterior **Intensity:** -36

```
Reading D21-CT-Coreg.Labels.am
Reading D14-CT-Coreg.Labels.am
Reading D21-PET70.Labels3.am
Reading D14-PET95.Labels4.am
Reading D21-PET90.Labels2.am
Reading D21-PET95.Labels4.am
Reading D21-Pet99.Labels2.am
Reading D14-PET99.Labels2.am
Reading D14-Lungs
>
```

Figure 5-12: Amira CT segmentation

Segmentation is performed using the “Segmentation Editor”. CT data is loaded as the image data set and a new “label” is created. Next a new material *lung* is created. Segmentation can be accomplished using a combination of the “brush”, “lasso”, “magic wand”, and “threshold” tools. It will most likely be necessary to use a combination of all tools for accurate segmentation.

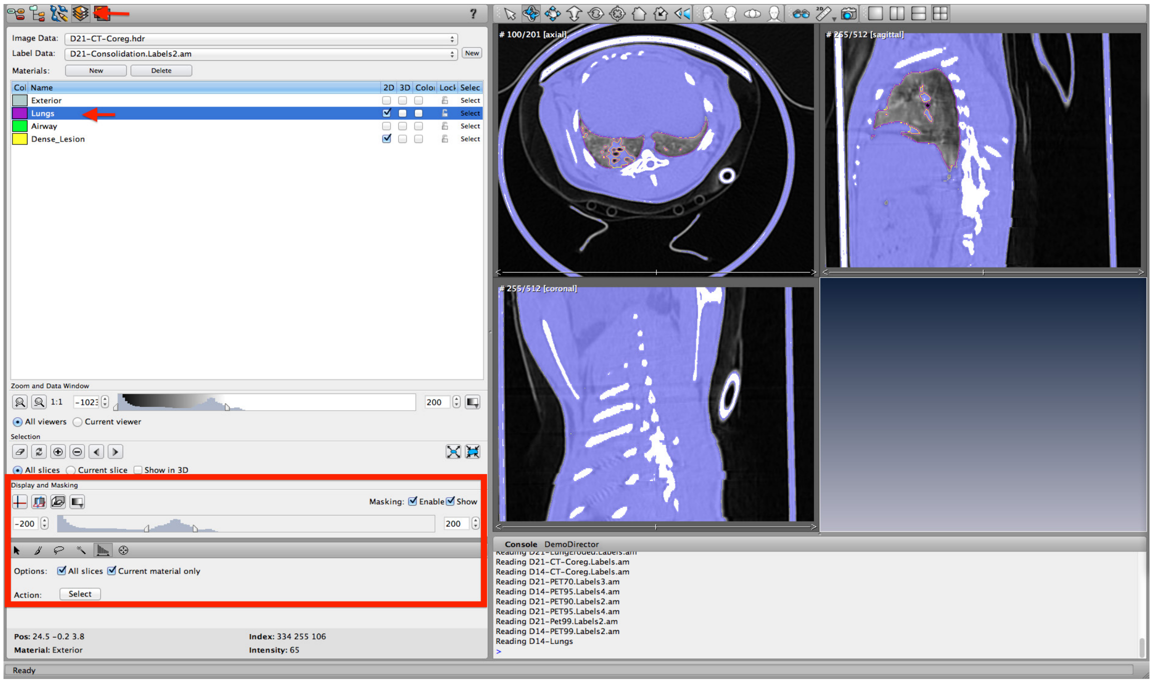

Image Data: D21-CT-Coreg.hdr

Label Data: D21-Consolidation.Labels2.am

Col	Name	2D	3D	Colo	Lock	Selec
	Exterior	☐	☐	☐		Select
🟪	Lungs	☑	☐	☐		Select
🟩	Airway	☐	☐	☐		Select
🟨	Dense_Lesion	☑	☐	☐		Select

-1023 … 200

● All viewers ○ Current viewer

● All slices ○ Current slice ☐ Show in 3D

Masking: ☑ Enable ☑ Show

-200 … 200

Options: ☑ All slices ☑ Current material only

Action: Select

Pos: 24.5 -0.2 3.8 **Index:** 334 255 106

Material: Exterior **Intensity:** 65

Ready

Console DemoDirector

```
Reading D21-LungEroded.Labels.am
Reading D21-CT-Coreg.Labels.am
Reading D14-CT-Coreg.Labels.am
Reading D21-PET70.Labels3.am
Reading D14-PET95.Labels4.am
Reading D21-PET90.Labels2.am
Reading D21-PET95.Labels4.am
Reading D21-Pet99.Labels2.am
Reading D14-PET99.Labels2.am
Reading D14-Lungs
>
```

Figure 5-13: Amira pathologic lung segmentation

Segmentation of pathologically involved lung tissue is done following the segmentation of the entire lung. Because individual voxels can only be attributed to a single material, it will be necessary to first duplicate the “label” containing the original lung segmentation. Segmentation of the pathologically involved tissue will be carried out using the copy of the original “label”. Defined threshold ranges are used to segment pathologically involved regions of interest. Threshold settings can be manipulated as indicated by the red box.

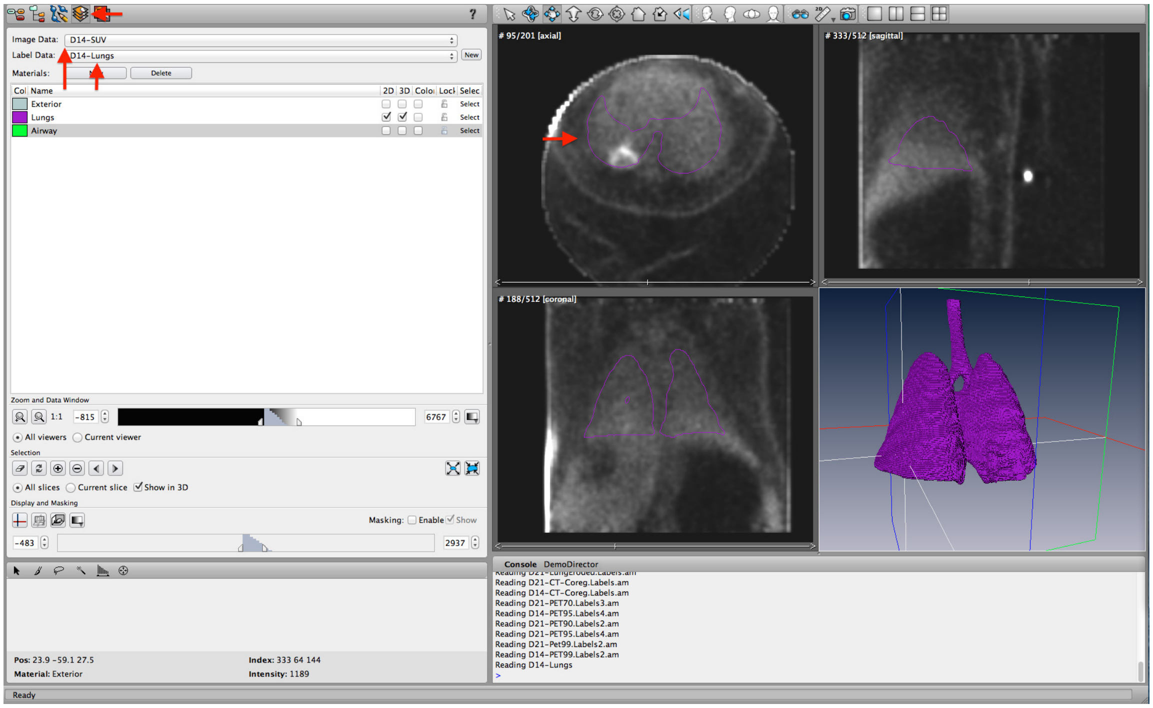

Image Data: D14-SUV

Label Data: D14-Lungs

Materials:

Col	Name	2D	3D	Color	Lock	Select
	Exterior	☐	☐	☐		Select
	Lungs	☑	☑	☐		Select
	Airway	☐	☐	☐		Select

Zoom and Data Window

1:1 -815 6767

● All viewers ○ Current viewer

Selection

● All slices ○ Current slice ☑ Show in 3D

Display and Masking

Masking: ☐ Enable ☑ Show

-483 2937

Pos: 23.9 -59.1 27.5

Index: 333 64 144

Material: Exterior

Intensity: 1189

Ready

```
Reading D21-CT-Coreg.Labels.am
Reading D14-CT-Coreg.Labels.am
Reading D21-PET70.Labels3.am
Reading D14-PET95.Labels4.am
Reading D21-PET90.Labels2.am
Reading D21-PET95.Labels4.am
Reading D21-Pet99.Labels2.am
Reading D14-PET99.Labels2.am
Reading D14-Lungs
>
```

Figure 5-14: Amira PET segmentation

The "Label Data" generated from the CT data can be applied to the PET data as well by simply selecting the appropriate "Image Data" and "Label Data" from the dropdown menus. After defining the lung window in the PET data set, it is then possible to segment regions of the lung with high tracer uptake.

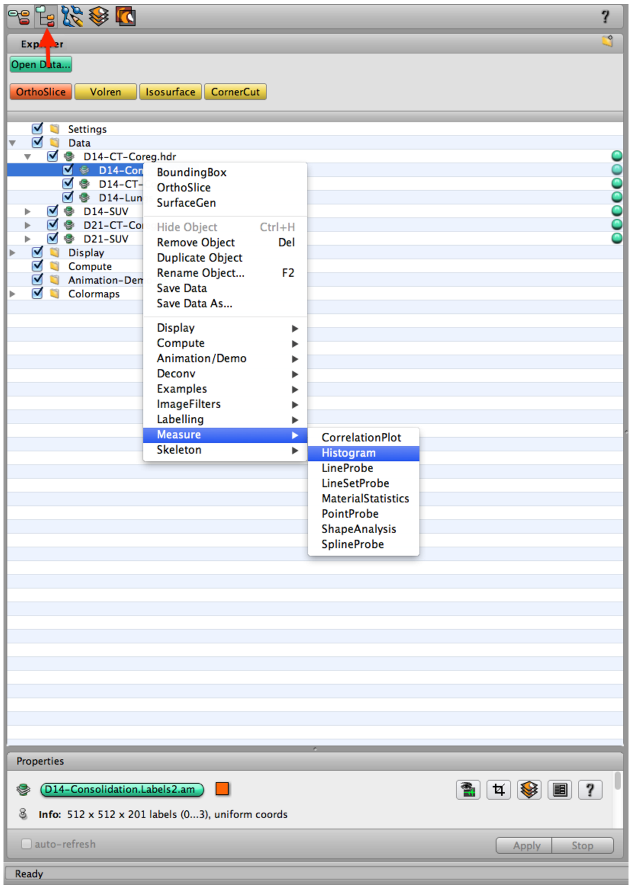

Info: 512 x 512 x 201 labels (0...3), uniform coords

Figure 5-15: Amira histogram

Selection of the label data for histogram analysis can be done through the “Tree view viewer” module.

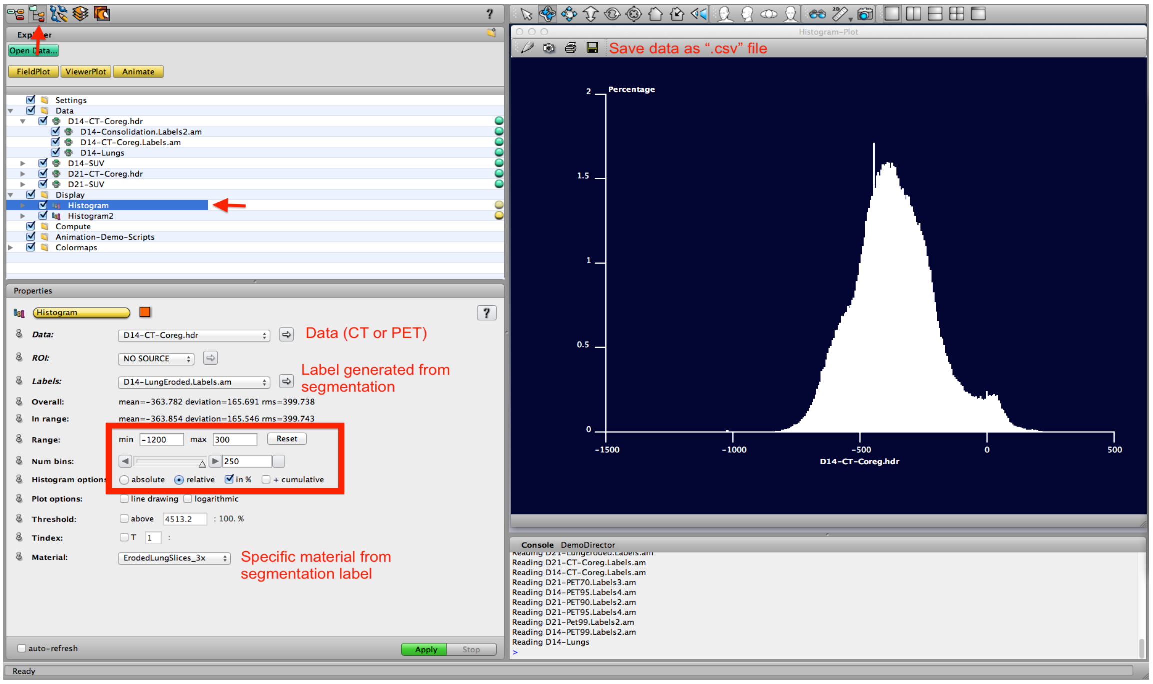

Save data as ".csv" file

Data: D14-CT-Coreg.hdr

Data (CT or PET)

ROI: NO SOURCE

Labels: D14-LungEroded.Labels.am

Label generated from segmentation

Overall: mean=-363.782 deviation=165.691 rms=399.738

In range: mean=-363.854 deviation=165.546 rms=399.743

Range: min -1200 max 300 Reset

Num bins: 250

Histogram options: ○ absolute ● relative ☑ in % ☐ + cumulative

Plot options: ☐ line drawing ☐ logarithmic

Threshold: ☐ above 4513.2 : 100. %

Tindex: ☐ T 1 :

Material: ErodedLungSlices_3x

Specific material from segmentation label

```
Reading D21-CT-Coreg.Labels.am
Reading D14-CT-Coreg.Labels.am
Reading D21-PET70.Labels3.am
Reading D14-PET95.Labels4.am
Reading D21-PET90.Labels2.am
Reading D21-PET95.Labels4.am
Reading D21-Pet99.Labels2.am
Reading D14-PET99.Labels2.am
Reading D14-Lungs
>
```

Figure 5-16: Amira histogram file

Selection of the "histogram" module from the "Tree view viewer" brings up the options panel that is represented in the lower left quadrant. The appropriate variables that need to be supplied are "data set", "label", "range", "number of bins", and "materials". After the histogram plot is created, the raw data can be saved as a ".csv" file for further analysis in other programs.

Curriculum Vitae

Brian M. Luna May 5, 2014

218 N Charles St, Apt 2501
Baltimore, MD 21202

brianluna@jhmi.edu
(909) 647-5561

EDUCATION

2008-2014 **Doctor of Philosophy, Cellular and Molecular Medicine**
Thesis: Cavity Formation in the Rabbit Model of Tuberculosis
Advisor: Dr. William R. Bishai
Johns Hopkins University School of Medicine, Baltimore, MD

2004-2008 **Bachelor of Science, Biology**
University of California, Irvine

PEER-REVIEWED PUBLICATIONS

1. Xu, Z., Bagci, U., Kubler, A., **Luna, B.**, Jain, S., Bishai, W. R., Mollura, D. J. (2013). Computer-Aided Detection and Quantification of Cavitary Tuberculosis from CT Scans. Medical Physics. *In Press.*
2. Bagci, U., Foster, B., Miller-Jaster, K., **Luna, B.**, Dey, B., Bishai, W. R., Jonsson, C. B., Jain, S., and Mollura, D. J. (2013). A computational pipeline for quantification of pulmonary infections in small animal models using serial PET-CT imaging. EJNMMI Res 3, 55.
3. Foster, B., Bagci, U., **Luna, B.**, Dey, B., Bishai, W., Jain, S., Xu, Z., and Mollura, D. J. (2013). Robust segmentation and accurate target definition for positron emission tomography images using Affinity Propagation. In (IEEE), pp. 1461–1464.
4. Larsson, C., **Luna, B.**, Ammerman, N. C., Maiga, M., Agarwal, N., and Bishai, W. R. (2012). Gene expression of Mycobacterium tuberculosis putative transcription factors whiB1-7 in redox environments. PLoS ONE 7, e37516.
5. **Luna, B.**, Juhn, J., and James, A. A. A. (2007). Injection of dsRNA into female A. aegypti mosquitos. J Vis Exp, 215.

MANUSCRIPTS

1. **Brian Luna**, André Kubler, Christer Larsson, Brent Foster, Ulas Bagci, Daniel J. Mollura, Sanjay Jain and William Bishai. (2014). *In vivo*

Prediction of Tuberculosis Cavity Formation. IN SUBMISSION

2. **Brian Luna**, André Kubler, Christer Larsson, Nicole C. Ammerman, Bruno B. Andrade, Marlene Orandle, Kevin Bock, Ziyue Xu, Ulas Bagci, John Marshall, Michael Urbanowski, Jay Burns, Kathryn Winglee, Bintou Ahmadou, Laurene Cheung, Mariah Klunk, Sanjay Jain, Alan Sher, Jon S. Friedland, Paul T.G Elkington, William R. Bishai. (2014). A quantitative, imaging-based rabbit model of tuberculosis reveals upregulation of endogenous tissue-destructive enzymes in cavitary lesions and progressive loss of functional lung tissue. IN SUBMISSION.

RESEARCH ORAL PRESENTATIONS

1. Johns Hopkins Center for Tuberculosis Research TB Day. Johns Hopkins University. 2013
2. Cellular and Molecular Medicine Program Retreat. Johns Hopkins University. 2012
3. Johns Hopkins Center for Tuberculosis Research TB Day. Johns Hopkins University. 2012

RESEARCH POSTER PRESENTATIONS

1. B. Foster, U. Bagci, Z. Xu, B. Dey**,** **B. Luna**, W. Bishai, S. Jain, D.J. Mollura. (2013). Affinity Propagation Clustering Determines Distributed Uptake Regions in PET Images: A Computer-Aided Approach for Quantification of Pulmonary Infections in Small Animals. Society of Nuclear Medicine.
2. **B. Luna**, A. Kubler, C. Larsson, M. Klunk, S. Jain and W. Bishai. (2013). Radiological Markers That Are Predictive of Cavitary Disease Progression. Keystone Symposium. Host Response to Tuberculosis.
3. **B. Luna**, A. Kubler, C. Larsson, S. Jain, and W. Bishai. (2012). ^{18}F-flouro-deoxy-glucose PET/CT is not predicative of cavity development in the rabbit model of tuberculosis. Molecular Imaging of Infectious Diseases: Current Status and Future Challenges
4. **B. Luna**, N. Agarwal, J.H. Lee, C. Larsson, N. Ammerman, W. Bishai. (2010). A transposon mutant screen to identify a cAMP transport system in Mycobacterium tuberculosis. Keystone Symposium.

AWARDS

Keystone Symposia Underrepresented Minority Scholarship 2013
MARC scholar 2007
MHIRT grant recipient 2007
MBRS recipient 2006-2007
Dean's Honor List Spring 2005, Fall 2006.

RESEARCH EXPERIENCE

Graduate Student, Johns Hopkins 2009-2014

1. Characterization of cAMP export in Mycobacterium tuberculosis.
2. In-vivo prediction of cavitary disease in the rabbit model of cavitary tuberculosis.
3. Host-directed therapies for treatment of tuberculosis. Inhibiting MMP-1 using RO32-3555
4. Characterizing latent tuberculosis disease progression in the rabbit model of tuberculosis by [18F]-2-Fluoro-Deoxy-D-Glucose (FDG)-PET/CT imaging.

Undergraduate Student, UC Irvine 2006-2008:

1. Create transgenic *Anopheles gambiae* mosquitoes by homologous recombination of repetitive sequence in 4th instar larvae.
2. Time depend knockdown of DBI mRNA transcripts in *Aedes aegypti* by RNAi.

Undergraduate, Universidad Autónoma de Madrid 2007

1. The effect of FMDV protein 2C on actin microfilaments and tubulin microtubules of the host cell. (NIH grant MD001485)